TriDurLE

National Center for Transportation
Infrastructure Durability & Life-Extension

Project ID: 2022-UCD-01

Time-dependent Durability of Composite-Repaired Bridge Members

Final Report

by

Yail Jimmy Kim
University of Colorado Denver
1200 Larimer Street, Denver, Colorado, 80217

for

National University Transportation Center TriDurLE
Department of Civil & Environmental Engineering
405 Spokane Street PO Box 642910
Washington State University Pullman, WA 99164-2910

July 31, 2024

Acknowledgements

The research team would like to acknowledge support from the US Department of Transportation through the National Center for Transportation Infrastructure Durability & Life-Extension (TriDurLE). Technical contents presented in this report are based on the opinion of the authors, and do not necessarily represent that of others.

Disclaimer

Table of Contents

Contents

Part I: Evolutionary Characteristics of Microstructural Hydration and Chloride Diffusion in UHPC

Part II: Cellular Automata for Corrosion in CFRP-Strengthened Bridge Columns

Part III: Simulated Chloride Penetration into a Solid Slab Bridge Overlayed with Ordinary Concrete and UHPC

List of Tables

List of Figures

Executive Summary

This report presents a three-phase research program concerning the durability of composite-repaired bridge members. The first phase discusses the evolutionary characteristics of microstructural hydration and chloride migration in ultra-high performance concrete (UHPC). The physicochemical interactions of constituents are simulated in conjunction with a random walk algorithm. The computed responses of the UHPC mixtures at a compressive strength varying from f'_c = 149 MPa to 164 MPa are comparatively evaluated for a curing period of 28 days against those of ordinary concrete involving f'_c = 30 MPa to 45 MPa. When the hydration of cementitious pastes proceeds, the quantity of silicates becomes larger alongside irregularly dispersed byproducts (calcium silica hydrate, C-S-H, and calcium hydroxide, CH). Owing to the formation of pozzolanic C-S-H consuming CH, the silicate reactions of UHPC are less than the reactions of the ordinary concrete. The implications of tricalcium silicate (C_3S) are notable for the early-age strength gain of UHPC in comparison with its dicalcium silicate (C_2S) counterpart. The matured pozzolanic reactions and invariable packing density of UHPC are responsible for preserving the proportion of silica fume in the mixtures. While the volumetric increase of conventional C-S-H is not controlled by water-binder ratios of the ordinary concrete and UHPC within 2 days of hydration, the extent of the pozzolanic C-S-H is tantamount to that of the conventional C-S-H at 28 days. Relative to UHPC, the ordinary concrete releases more heat caused by exothermic reactions that are a function of saturated pores and silica fume. Regarding corrosion durability, the chloride contents of a bridge deck cast with the ordinary concrete exceed the content of a deck with UHPC. As part of technology transfer, the notion of performance-based design applies and practice guidelines are suggested.

The second phase deals with the durability modeling of bridge piers subjected to corrosive environments, including atmospheric, splash, and submerged conditions, for a service period of 100 years. Two types of reinforced concrete columns are utilized, cast-in-place and accelerated bridge construction (ABC), and their time-dependent performance is predicted by von Neumann's square lattice in conjunction with a novel evolutionary mathematics approach called cellular automata. The capacity of the corrosion-damaged columns is upgraded using carbon fiber reinforced polymer (CFRP) sheets. Depending upon concrete strength and construction method, chloride migration mechanisms are evaluated to elucidate the variation of diffusion coefficients, chloride concentrations, and other corrosion-related issues for those columns with and without CFRP-confinement. For the first 30 years, the chloride diffusion of the ABC column is slower than that of the cast-in-place column; otherwise, no difference is noticed. Under the splash condition incorporating periodic wet-dry cycles, chloride concentrations remarkably increase relative to other exposure environments, particularly for the cast-in-place column. The development of corrosion current density is dominated by the pore structure of the concrete, and the corrosion initiation of the ABC column takes 4.3 times longer compared with its cast-in-place counterpart. At 100 years, the capacity of the cast-in-place and ABC columns decreases by 28.1% and 23.2%, respectively, primarily due to the impaired concrete near the degraded reinforcing bars in a corrosion influence zone. The columns' responses are enhanced by CFRP-confinement in terms of toughness, energy dissipation, load-carrying capacity, and load-moment interactions.

The third phase elaborates on the efficacy of ultra-high performance concrete (UHPC) overlays holds great promise for mitigating chloride-induced corrosion in reinforced concrete bridges. This research examines the corrosion resistance of a bridge structure through the application of simulation techniques in order to understand the effectiveness of ordinary concrete and UHPC overlays. To represent the three-dimensional microstructure of ordinary concrete and UHPC, the Virtual Cement and Concrete Testing

Laboratory (VCCTL) program is utilized. Additionally, an agent-based model is developed to investigate chloride penetration mechanisms within the concrete overlays. Furthermore, the structural response of the overlayed bridge under a corrosive condition is studied

Keywords: bridges; composites; durability; hydration; microstructure; properties; rehabilitation; repair; time-dependent characteristics; ultra-high performance concrete (UHPC)

Part I: Evolutionary Characteristics of Microstructural Hydration and Chloride Diffusion in UHPC

I.1. Introduction

Durability is a comprehensive concept with regard to the ability of resisting unfavorable distress when a structure is exposed to detrimental situations under assorted physical and chemical attributes. For safe and functional performance, the ultimate and serviceability limit states of constituting members are the most important requirements (AASHTO 2020). Even if the expected life span of concrete elements is over 50 to 75 years (Stewart and Val 1999), premature deterioration frequently occurs due to aggressive service environments. Consequently, a significant budget is executed to maintain acceptable quality in those elements. Among many, corrosion is deemed to be a critical factor in civil infrastructure; for example, it brings about a direct cost of more than 3% of the GDP (gross domestic product) in the United States, equivalent to $558 billion (Akhoondan and Bell 2016). Chloride-induced corrosion is particularly vulnerable to reinforced concrete, which is related to load-carrying capacities, repairs, and longevity (Zhou et al. 2015). The penetration of chlorides into concrete is dominated by the hydration of cementitious pastes (Wong et al. 2010). Properly hydrated pastes minimize the connectivity of micropores, inhibit the migration of chloride ions, and increase the packing density of concrete (Anastasiou 2021). Therefore, an appropriate understanding of hydration mechanisms is a prerequisite for adopting emerging concrete materials.

Based on the principle of reactive powder concrete in the 1990s (Richard and Cheyrezy 1994), a dense cementitious composite called ultra-high performance concrete (UHPC) was introduced to the infrastructure community and is recognized as a state-of-the-art construction material (ACI 2018). The benefits of using UHPC are found in its superior compressive strength of about 150 MPa, increased toughness, homogeneous composition, affordable maintenance, and reduced member size (Russell and Graybeam 2013; Shi et al. 2015). Review articles collate laboratory experiments and field applications around the globe, encompassing mixture optimization, mineralogical properties, workability, non-conventional systems, hybrid structures, strengthening, and highway bridges (Zhu et al. 2020; Bajaber and Hakeem 2021). For the assessment of durability, accelerated testing was conducted (Pierard et al. 2012; Alkaysi et al. 2016; Lu et al. 2021; Matos et al. 2021) and results substantiated that UHPC effectively resisted various types of damage caused by freeze-thaw, sulfate, alkali silica reaction, and chloride penetration. Despite these meaningful endeavors, little is known about the hydration process of UHPC at microscale and corresponding implications for durability in relation to chloride transport that is imperative to comprehend the long-term performance of UHPC structures. Rigorous investigations should, thus, be required to explore the obscure research themes.

Current practices for concrete engineering are heavily reliant upon prescriptive design methods (ACI 2019; AASHTO 2020). These approaches, albeit convenient, contain intrinsic limitations such that engineers make decisions to avoid predefined failure characteristics, rather than to address measurable requirements for structural members to withstand the specific levels of operational challenges. Accordingly, performance-based design, an alternative methodology, emerged in a couple of disciplines (e.g., seismic and fire) and active research is undertaken (Shama and Jones 2020; Siddiqui et al. 2021) to cope with realistic classifications that are anticipated during the service period of constructed facilities. Likewise, performance-based durability recently gained attention and valuable findings are being reported in the area of structural concrete (Bhaskar et al. 2020; Geiker et al. 2021). Those macroscopic examinations contributing to the development of the non-conventional design philosophy should be supported by scientific knowledge that fundamentally explicates physicochemical interactions between the constituents of concrete and external substances.

This report deals with an analytical protocol to simulate the microstructure of UHPC and chemical reactions for hydration, which would then be linked with stochastic chloride diffusion on the basis of a random walk algorithm. In addition, the responses of ordinary concrete are predicted and comparatively assessed to better evaluate the unique features of UHPC. Technical data are conceptualized to establish performance levels in terms of chloride content.

I.2. Material Characteristics

This section delineates typical concrete mixtures to be used for numerical simulations, which are essential to elucidate the behavior of ordinary concrete and UHPC from microstructural and Fickian-kinetic perspectives.

I.2.1. Benchmark Concrete Mixtures

According to literature (ACI 2002; Wille et al. 2012), benchmark concrete mixtures were designed. The compressive strength of ordinary concrete was set from f'_c = 30 MPa to 45 MPa, while that of UHPC was spanned from f'_c = 149 MPa to 164 MPa. Table I.1 enumerates details on these mixtures along with water-binder ratios (*w*/*b*) and relative mass proportions. The inconsistent portion of the fine aggregate in UHPC was attributed to the fact that the mixture design (Wille et al. 2012) was developed with two sizes of sand grains (0.2 mm and 0.8 mm). The percent mass of the major compounds in the cement of the ordinary concrete and UHPC is listed in Table I.2, involving tricalcium silicate (C_3S), dicalcium silicate (C_2S), tricalcium aluminate (C_3A), and tetracalcium aluminoferrite (C_4AF), which were based on existing documents (Alkaysi 2016; Qi et al. 2021). Although the contents of those compounds vary by cement type (Bourchy et al. 2020), the quantities given in Table I.2 can represent most products available in practice.

I.2.2. Chemical Reactions

Among others, two primary reactions relevant to the hydration of a cement paste were focused. When C_3S and C_2S interact with dihydrogen monoxide (H_2O), silicate reactions produce conventional calcium silica hydrate (C-S-H) and calcium hydroxide ($Ca(OH)_2$ or CH) (Liu et al. 2017; Pathirage et al. 2019)

$$C_3S + 5.3H_2O = C_{1.7}SH_4 + 1.3CH \quad (I.1)$$

$$C_2S + 4.3H_2O = C_{1.7}SH_4 + 0.3CH \quad (I.2)$$

Pozzolanic reactions occur on account of the silicon dioxide (SiO_2) in the silica fume of the UHPC mixture (Tavares et al. 2020). The CH crystals supplied from the foregoing silicate reactions react with the silica fume and create pozzolanic C-S-H gels ($C_{1.1}SH_{3.9}$), which are important for the durability of concrete by filling micro-voids (Liu et al. 2020; Kim et al. 2020)

$$1.1CH + SiO_2 + 2.8H_2O = C_{1.1}SH_{3.9} \quad (I.3)$$

I.2.3. Porosity

Considering that the network of capillary pores affects the permeability of concrete (Babaei et al. 2021), the amount of saturated spaces in the pastes of the aforementioned mixtures needs to be quantified with the progression of hydration. The volume of capillary pores (V_{cap}) is often estimated by (Powers 1962)

$$V_{cap} = \frac{w/b - 0.36\alpha_{cm}}{w/b + 0.32} \tag{I.4}$$

where w/b is the water-binder ratio of the concrete and α_{cm} is the degree of hydration in the paste, which may be obtained from

$$\alpha_{cm} = \frac{M_{hc} + M_{hs}}{M_{ic} + M_{is}} = \frac{\alpha_c + \alpha_{sf}\left(M_{is}/M_{ic}\right)}{1 + \left(M_{is}/M_{ic}\right)} \tag{I.5}$$

where M_{hc} and M_{hs} are the mass of hydrated cement and silica fume of the concrete, respectively, and M_{ic} and M_{is} are their initial unhydrated counterparts; and α_c and α_{sf} are the degree of hydration for the cement and silica fume, respectively, to be determined from computational modeling described in Sec. I.3 ($\alpha_c = M_{hc}/M_{ic}$ and $\alpha_{sf} = M_{hs}/M_{is}$).

I.2.4. Hydration Heat

The major compounds of the cement (Table 2) possess specific thermodynamic quantities: enthalpy = 517 kJ/kg, 262 kJ/kg, 1,144 kJ/kg, and 725 kJ/kg for C_3S, C_2S, C_3A, and C_4AF, respectively (Fukuhara et al. 1981; Taylor 1990). Upon obtaining the hydrated volume of these compounds and knowing the densities, the heat released during a hydration period can be calculated using those pre-calibrated enthalpy values.

I.2.5. Chloride Diffusion

The rate of chloride ingress in concrete is referred to as a chloride diffusion coefficient (D), which is express by Fick's first law

$$J = -D\left(dc/dL\right) \tag{I.6}$$

where J is the diffusion flux; c is the concentration; and L is the dimensional length. The diffusion occurs in a cement paste, especially via saturated capillary and gel pores (Chen and Razaqpur 2021). In general, the capillary pores are not filled with hydration products; nonetheless, the volume of the pores decreases as the amount of the products augments over time (Zhang et al. 2020). The gel pores exist in the crystals of the products and, contrary to the capillary pores, the gel pores occupy more spaces as the hydration progresses (Zhang and Zhou 2020). Passing through those pores, chloride ions accumulate inside hardened concrete and precipitate the corrosion of steel rebars, thereby degrading the performance and service life of reinforced concrete structures. Contemplating that aggregates in a concrete mixture interrupt the flow of chlorides (Shafikhani and Chidiac 2020), a relationship may be established between the diffusion coefficients of a cement paste and the concrete (D_p and D_c, respectively)

$$D_c = \xi D_p \tag{I.7}$$

where ξ is a conversion factor. From a practical standpoint, because of a difference in microstructural configurations, the diffusion of ordinary concrete and UHPC differs. It is also worth noting that, as visible in constructed members irregularly damaged by corrosion, the migration of chloride ions is nondeterministic; for this reason, conventional approaches (e.g., finite difference method) without considering uncertainties can provide imprecise results (Srikanth and Arockiasamy 2020).

I.3. Computational Modeling

A two-phase simulation framework is outlined to develop the microstructures of ordinary concrete and UHPC as well as to predict the migration of chlorides, as illustrated in Fig. I.1. Emphasis lies on the hydration of pastes and the quantification of diffusion coefficients in both concrete types.

I.3.1. Microstructural Model

I.3.1.1. Formulation

The three-dimensional microstructure of the pastes in the ordinary concrete and UHPC was modeled using computer software, called the Virtual Cement and Concrete Testing Laboratory (VCCTL, Bullard 2014). In compliance with the mixture proportions specified in Table I.1, the program generated volume elements (voxels comprising 100 by 100 by 100 pixels) with randomly distributed constituents representing digitized pastes in a computational domain (Fig. I.2). For the stochastic positioning of those constituents, the built-in random number generator created non-zero integers (Bullard 2014). Each voxel with a pixel size of 1 μm was equated to be a single object, such as silica fume, C_3A, C_4AF, and a capillary pore, and was used to predict the chemical reactions over time.

I.3.1.2. Simulated hydration

The digitized pastes were subjected to moisture-curing for 28 days at a constant temperature of 20^oC. Because free water in capillary pores is necessary for the hydration reactions, the pores of the pastes were regarded to be saturated (Sanchez et al. 2020). The two-phase hydration process, consisting of dissolution and diffusion for the chemical reactions, was iterated until a target period of 28 days (672 hours) was reached using the succeeding conversion equation (Bullard 2014)

$$t = \beta n^2 \tag{I.8}$$

where t is the physical time in hours; β is the conversion factor ($\beta = 3.5\times10^{-4}$); and n is the number of computational cycles (n = 1,386 is equivalent to 28 days).

- *Dissolution*: the microstructural configuration formulated in the preceding section was scanned to identify solid components and capillary pores. Afterward, the solubility of the individual solids was determined by the preset dissolution probability that was contingent upon physical significance (C_3A and C_3S have a high probability of 0.8, while C_4AF and C_2S have a low probability of 0.2, Bentz 1995). When the position of a solid compound was next to that of randomly distributed capillary pores, its solubility was identified: if the assigned dissolution probability was greater than a randomly generated number, the solid became soluble; otherwise, the state remained unchanged. In so doing, the process of dissolution was completely stochastic.
- *Diffusion*: In accordance with the above-described chemical reactions, the dissolved constituents reacted with water and diffusing products were generated (e.g., C-S-H in Eqs. I.1 to I.3). All products, including those from the current iteration and previously created ones, were dispersed via a random walk algorithm to be discussed in Sec. I.3.2.

I.3.1.3. Computed data

The simulated microstructure of the pastes generated hydrated and unhydrated constituents (C_3S, C_2S, C_3A, C_4AF, and SiO_2) at every iteration; accordingly, the degree of hydration (α_c and α_{sf} for the cement and silica fume, respectively) and the amount of enthalpy-based hydration heat were attained. Also acquired are the hydration products, conventional and pozzolanic C-S-H gels, which were necessary to estimate micropores pertaining to the migration of chlorides.

I.3.2. Random Walk for Chloride Diffusion

I.3.2.1. Discrete entity modeling

The rendered microstructural images at a hydration period of 28 days were processed by agent-based modeling in conjunction with a random walk algorithm. The agent-based modeling, often employed in computational social science (Macal 2020), handles multiple interactions between discrete entities under prearranged rules. Detailed information on the principle, development, and code language of Netlogo, an open-source application program, is available elsewhere (Wilensky and Rand 2015). Each of the three-dimensional representations (100 by 100 by 100 pixels) was divided into two-dimensional inputs (100 by 100 pixels) at intervals of 1 μm in the depth direction; subsequently, images were analyzed every ten pixels (10 μm) and results were averaged to characterize chloride diffusion in the pastes of the ordinary concrete and UHPC mixtures: the diffusion coefficients were taken to be stable after 28 days of curing (Yu et al. 2019). The selected images were imported to the simulation domain of Netlogo (Fig. I.3) and the individual capillary pores were designated by patches (spatial entities). Since the microstructural images did not contain gel pores, 25% of the conventional C-S-H and 19% of the pozzolanic C-S-H were assumed to be the amount of gel pores (Felix et al. 1997; Yajun and Cahyadi 2004). Thereafter, self-organized agents representing chloride ions were distributed to every patch that covered the locations of the capillary and gel pores. Each agent generated a random number (n) at two decimal places between 0 and 1, and the moving direction of the agents was determined: up ($0 \leq n < 0.25$), right ($0.25 \leq n < 0.5$), down ($0.5 \leq n < 0.75$), and left ($0.75 \leq n \leq 1.0$). The agents then checked the state of the pixel in one of the four directions. If the immediate neighbor was a pore, the agent moved by 1 μm in that direction; otherwise, it stayed at the present location. This process, depicted in Fig. I.4(a), was iterated until convergence was achieved.

I.3.2.2. Determination of diffusion coefficient

Chloride diffusion coefficients for the pastes of the ordinary concrete and UHPC were calculated by (Liu et al. 2012)

$$D_p = \phi \frac{\left\langle r(t)^2 \right\rangle}{\left\langle r_{free}(t)^2 \right\rangle} D_{free} \tag{I.9}$$

where ϕ is the pore-fraction of the concrete; D_{free} is the diffusion coefficient in free water ($D_{free} = 1.5 \times 10^{-9}$ m^2/s (Weast 1976)); and $<r(t)^2>$ and $<r_{free}(t)^2>$ are the average squared distances of the agents at the initial time ($t = 0$) and simulation time t under the paste and free water conditions, respectively, which were acquired from the Euclidean distance

$$\left\langle r(t)^2 \right\rangle or \left\langle r_{free}(t)^2 \right\rangle = \frac{1}{N} \sum_{i=1}^{N} \left[\left(x_i(t) - x_i(0) \right)^2 + \left(y_i(t) - y_i(0) \right)^2 \right] \tag{I.10}$$

where N is the number of the agents; and x_i and y_i are the coordinates of the agents at time t (Figs. I.4(b) to (e)). The paste condition indicates the simulation space mentioned in Sec. 4.2.1 (Figs. I.4(b) and (d)), while the free water condition was set with a 100 by 100 pixel region without the solid compounds and the agents randomly moved in all orthogonal directions (Figs. I.4(c) and (e)).

I.3.3. Validation

Before implementing the predictive approaches for the migration of chlorides in the ordinary concrete and UHPC, a validation step was undertaken using experimental data taken from published papers. Unlike the abundant cases of a cement paste in the ordinary concrete, the diffusion of UHPC was not reported at the paste level. As such, the D_p of UHPC was estimated from D_c (Eq. I.7) (Li et al. 2012)

$$D_p = D_c / \left(V_p T \right) \tag{I.11}$$

$$T = \frac{1+V_p}{3-V_p} \tag{I.12}$$

where V_p is the volumetric fraction of the paste from the micromechanical model and T is the tortuosity associated with aggregate. Figures I.5(a) and (b) exhibit the convergence of relative diffusivity (D_p/D_{free}) in the ordinary concrete and UHPC, respectively. The largely fluctuating diffusivities stabilized when 200 or more agents were assigned and, for conservative prediction, 2,000 agents were adopted at 300,000 iterations. As far as the diffusion coefficients of the pastes (D_p) are concerned, the computed values with a water-binder ratio of w/b = 0.37 to 0.54 (Fig. 5(c)) and w/b = 0.14 to 0.18 (Fig. I.5(d)) for the ordinary concrete and UHPC, respectively, were within the ranges of others' experimental programs (Page et al. 1981, Byfors 1987, Tang and Nilsson 1992, Sun et al. 2011, Pierard et al. 2012, Pourjahanshahi and Madani 2021, Li et al. 2012, Thomas et al. 2012). Owing to the high porosity of the ordinary concrete, its diffusion coefficients (Fig. I.5(c)) were much higher than those of UHPC (Fig. I.5(d)), which will be elaborated later.

I.4. RESULTS

The simulated outcomes of hydrated pastes in ordinary concrete and UHPC mixtures are compiled and construed with a focus on compound interactions during a hydration process and their related consequences, which would be the foundation of developing practice recommendations to address concerns arising from chloride content.

I.4.1. Silicate and Pozzolanic Reactions

I.4.1.1. Qualitative assessment

The chemical reactions of the ordinary concrete and UHPC are plotted in Figs. I.6 and I.7, respectively. The contents of C_2S and C_3S were instrumental in the silicate reactions (Eqs. I.1 and I.2) and a considerable change was noticed in the compound composition of the cement paste over time. The growth of the silicate amount denoted the progression of hydration, leading to the hardening of the paste. Since the rate of hydration is unsteady (Schmid et al. 2019), the spatial distributions of C-S-H and CH were irregular. It is worth noting that the entangled C-S-H particles provide the mechanical resistance of the paste, which controls the strength of the concrete. The 28-day curing images point out that some portions of the pastes were unhydrated and, as previous research reported (Granju and Grandet 1988), the C_2S and C_3S compounds may remain without the chemical reactions for more than several months. Compared with the ordinary concrete case (Fig. I.6), the extent of CH in the silicate reactions of UHPC was insignificant (Fig. I.7(a)). This is attributable to the consumption of the produced CH by the formation of the pozzolanic C-S-H (Eq. I.3) in tandem with SiO_2 (Fig. I.7(b)).

I.4.1.2. Quantified reactions

Figures I.8(a) and (b) demonstrate the time-dependent depletion of C_3S and C_2S, respectively. Aligning with the different compressive strength of the UHPC and ordinary concrete mixtures (Table I.1), the quantity of C_3S in the former was consistently higher than that in the latter. The volume of C_3S in both cases rapidly declined within a curing period of 7 days and tended to level out (Fig. I.8(a)), meaning that the physical conformation of those mixtures was set (Sun et al. 2020). The degree of the reduction was a function of the water-binder ratio (w/b) that was a salient factor in the hydration process. As shown in the variation of C_2S (Fig. I.8(b)), the early-age contribution of C_3S (Fig. I.8(a)) was substantial to the strength gain of the hydrated pastes, which was experimentally confirmed (Kim et al. 2019). The pattern of the CH development (Fig. I.8(c)) agreed with the spectrum analysis of X-ray diffraction (Omotoso et al. 1995) and, in line with the qualitative assessment (Fig. I.7), the proportion of CH in UHPC was much lower relative to the occasion of the ordinary concrete, for which the dilution effect that transforms a chemical phase was responsible (Bhattacharya and Harish 2018). The crystallization of CH occupied the micropores of the pastes (Pignat et al. 2005) and influenced the evolution of porosity (to be detailed). Due to the active reactions with calcium hydroxide and dihydrogen monoxide (Eq. I.3), the fraction of the silica fume dwindled during the first 5 days (Fig. I.8(d), inset). The marginal alteration of the silica fume after 7 days in Fig. I.8(d) implies that i) the pozzolanic reactions matured (Eq. I.3) and ii) the packing density of the hardened UHPC microstructure became invariable (Fan et al. 2020).

I.4.2. Reaction Compounds

The temporal characteristics of C-S-H are graphed in Fig. I.9. When the reactions commenced for hydration, the C-S-H products emerged and propagated (Figs. I.9(a) and (b), where only C-S-H is observable). The volumetric increase of the conventional C-S-H in the ordinary concrete was independent of the water-binder ratio (or compressive strength) up to 2 days, beyond which bifurcations were seen (Fig. I.9(c)). Regarding the UHPC mixtures, the bifurcation took place at around 1 day, which signifies the quicker reaction kinetics of UHPC. Shown in Fig. I.9(d) is the total C-S-H of the mixtures, comprising the conventional and pozzolanic C-S-H compounds, divided by the initial binder volumes. Dissimilar to the conventional C-S-H case (Fig. I.9(c)), the gap was lessened between the ordinary concrete and UHPC because of the pozzolanic reaction that produced additional C-S-H (Eq. I.3). Figure 9(e) instantiates the implications of the pozzolanic C-S-H. The conventional C-S-H area of the 164 MPa UHPC was $2{,}324\times10^{-6}$ mm^2 at 28 days, 37.7% lower than that of the 30 MPa concrete; however, with the inclusion of the additional C-S-H compound, the area became $4{,}597 \times10^{-6}$ mm^2 at 28 days. The simulation results account for the mechanism of the UHPC's accruing strength with time. The ratio between the conventional and pozzolanic C-S-H products gradually rose from 0.8 to 1.05 (Fig. I.9(f)), and the impact of the compressive strength was negligible within a range between f'_c = 149 MPa and 164 MPa (Fig. I.9(f), inset).

I.4.3. Hydration

The exothermic reactions of the ordinary concrete and UHPC mixtures are provided in Fig. I.10(a). In general, the content of cement dominates the degree of hydration heat (Yalcinkaya and Copuroglu 2021), whereas all of the present mixtures possessed the same proportion of cement for comparison purposes (Table I.1). The heat of the ordinary concrete was higher due to the abundance of pore water and the absence of silica fume (Kadri and Duval 2009; Riding et al 2012). Given that the released heat exacerbates the autogenous shrinkage of concrete, accompanied by premature cracking (Kadri and Duval 2009; Kim et al. 2011), the UHPC mixtures are expected to outperform the ordinary concrete in the context of long-term durability. Figure I.10(b) points out the significance of water-binder ratios in the hydration heat at 28 days. From a micro-dynamics standpoint (Zhang et al. 2021), the diffusion of dihydrogen monoxide molecules raises temperatures during the hydration reactions. The degree of hydration associated with the cement and silica fume (Eq. I.5) is summarized in Figs. I.10(c) and (d). In both concrete types, the cement-related hydration precipitously went up for 7 days and the response slopes slowed down (Fig. I.10(c)). Such a trend is explained by the fact that the cement particles initially reacted with water at the surface level; then, the saturated portion impeded the ingress of the water so that the interaction between CH and C-S-H hindered the chemical reactions necessary for the hydration (Young 1972). Furthermore, the local osmosis that fractures the cement particles partially obstructed the hydration process (Tang et al. 2016). A similar propensity was noted for the silica fume case (Fig. I.10(d)) alongside the plateaus after 7 days, resulting from the activation of alkali in the cement compounds (Wang 2014).

I.4.4. Porosity

Figures I.11(a) and (b) illustrate the progression of capillary pores in the mixtures. The C_3S and C_2S compounds (appreciable white circular spaces at 0 days) were progressively pulverized with an increase in the hydration reactions (Eqs. I.1 and I.2); in other words, the areas of the saturated pores (black and red dots for the ordinary concrete and UHPC in Figs. I.11(a) and (b), respectively) decreased extensively. It is apparent to state that the presence of the silica fume lowered the porosity of UHPC (Fig. I.11(b)), which is beneficial in increasing the compressive strength of the mixture (Zhang et al. 2020). Shown in Fig. I.11(c) are the porosities of selected concrete types validated against the theoretical ones calculated by Eq. I.4. Even if the porosities exponentially decreased with time, the existence of the pores clarifies that the hydration products did not completely occupy the voids of the pastes. The tendency was retained in all mixtures, while the ramifications of the water-binder ratios were prominent, especially for the ordinary concrete (Fig. I.11(d)). These residual pores can accelerate the permeability of detrimental chemicals when the concrete is under service (Torrent et al. 2022).

I.5. Performance-Based Design

To expand the element-level investigations, a practical situation was hypothesized as per the American Association of State Highway Transportation Officials (AASHTO) Load and Resistance Factor Design (LRFD) Bridge Design Specifications (AASHTO 2020). A reinforced concrete deck (thickness = 250 mm) was designed with a cover depth of 50 mm and 75 mm when subjected to a corrosive environment.

I.5.1. Chloride Content

The content of chlorides in the deck at depth *x* and time *t* ($C(x,t)$) was estimated by (Stewart and Rosowsky 1998)

$$C(x,t) = C_0\left[1 - erf\left(\frac{x}{2\sqrt{tD}}\right)\right] \tag{I.13}$$

where C_0 is the surface chloride (C_0 = 3.5 kg/m^3 for a deicing condition); D is the diffusion coefficient predicted by the microstructure model; and *erf* is the Gauss error function. Figure I.12 reveals the progression of chlorides in the spatial and temporal domains. With the increased time, the chloride contents augmented (1 year and 100 years in Figs. I.12(a) and (b), respectively) and the susceptibility of the UHPC deck was much lower than that of the ordinary concrete deck. At the level of the steel reinforcement (50 mm and 75 mm from the concrete surface, Figs. I.12(c) and (d), respectively), the chloride contents smoothly rose and the deck cast with UHPC benefitted from retarding the accumulation of chlorides.

I.5.2. Assessment

Figure I.13(a) shows the time for corrosion initiation predicted by (Thoft-Christensen et al. 1996)

$$t_i = \frac{(C_v/10)^2}{4D}\left(erf^{-1}\left(\frac{C_{cr}-C_0}{C_i-C_0}\right)\right)^{-2} \tag{I.14}$$

where t_i is the initiation time in years; C_v is the cover depth in mm; and C_{cr} and C_i are the critical and initial chloride concentrations (C_{cr} = 0.4% and C_i = 0% of the cement weight, Elsener and Angst 2016). For the ordinary concrete, the occurrence of corrosion was expected after 6.5 years (f'_c = 30 MPa at a cover depth of 50 mm); however, more than 100 years was required for UHPC. The microstructure-based diffusion coefficients of the concrete mixtures (D_{free} and D) were converted to chloride permeability (Riding et al. 2018)

$$Q = \frac{206{,}830}{(D_{free}/D)\rho_0} \tag{I.15}$$

where Q is the permeability in Coulombs and ρ_0 is the pore solution resistivity (ρ_0 = 0.1 Ωm). As appraised by ASTM C1202 (ASTM 2019) in Fig. I.13(b), the corrosion vulnerability of the decks with the ordinary concrete and UHPC was classified into the High/Moderate and Low categories, respectively. Although the vulnerability does not necessarily mean immediate structural damage, attention should be paid to minimize adverse repercussions, as suggested in the next section.

I.5.3. Proposal

Pursuant to a published standard (Standards Australia 2007), three performance levels were defined as a function of the chloride content (Table I.3): Level I (Satisfactory) indicates a condition that a deck allows traffic loadings without a corrosion issue, Level II (Operational) signifies that a deck has partially corroded and needs regular inspections for maintenance/repair, and Level III (Critical) manifests that corrosion-induced damage is severe and major rehabilitation/replacement is highly likely. These levels focus on corrosion-related matters under a deicing condition and exclude other sources of deterioration (e.g., freeze-thaw, impact, and fatigue). The calculated chloride contents of the concrete mixtures were utilized at a variable cover depth to constitute the predefined performance levels and corresponding tolerable periods were identified in Table I.3. The Level I period of the deck with f'_c = 30 to 40 MPa at a cover depth of 50 mm, frequently employed in the field, was from 5 to 18 years. This range was in proximity to a measured average corrosion initiation period of 19.6 years (Estes and Frangopol 1999). The arithmetic mean of Level II was 29 years for the deck with the ordinary concrete, which was reasonably close to the actual life span of bridge decks spanning between 25 and 30 years (Tikalsky et al. 2005). Corrosion damage in the UHPC deck with f'_c = 149 to 164 MPa was not a primary factor dominating its performance when subjected to deicing agents. Notwithstanding the erratic nature of deck corrosion, the tolerable time enumerated in Table 3 suggests implementable guidelines: when planning an inspection, bridge professionals should proactively presume an expected performance level as per year-built and, if a deck exceeds the tolerable time of Level I, conduct specialized approaches such as nondestructive testing to properly diagnose the state of the deck.

I.6. Summary and Conclusions

This report has examined the hydration mechanisms and chloride migration of UHPC through microscopic models coupled with a random walk algorithm. The simulated results of the UHPC mixtures at a compressive strength of f'_c = 149 MPa to 164 MPa were appraised against the results of ordinary concrete possessing f'_c = 30 MPa to 45 MPa. The physicochemcial responses of pastes in these mixtures were evaluated during a time frame of 28 days. For technology transfer, the corrosion durability of a bridge deck was studied by means of three performance levels (*Satisfactory*, *Operational*, and *Critical*), depending upon chloride content. The following are concluded:

- As the hydration of the pastes progressed, the amount of silicates increased with erratically distributed C-S-H and CH. The silicate reactions of UHPC were not comparable to those of the ordinary concrete due to the formation of pozzolanic C-S-H that consumed the CH compounds.
- The volume of C_3S in both concrete types promptly decreased up to 7 days and stabilized. The early-age strength gain in UHPC was reliant upon the presence of C_3S, rather than that of C_2S. The dilution effect transforming chemical phases lowered the portion of CH in UHPC. Passing through a reduction for the first 5 days of curing, the proportion of silica fume was maintained steadily, which was associated with the matured pozzolanic reactions and invariable packing density of the UHPC mixtures.
- The water-binder ratio of the ordinary concrete and UHPC did not affect the volumetric increase of the conventional C-S-H within a hydration period of 2 days. Irrespective of compressive strength in UHPC, the development of pozzolanic C-S-H at 28 days was akin to that of the conventional C-S-H.
- The exothermic reactions of the concrete mixtures were dominated by saturated pores and silica fume; thus, the released heat of the ordinary concrete was higher relative to UHPC. Owing to the surface-level saturation of the cement particles, the ingress of water was impeded and the chemical interactions between CH and C-S-H slowed down. In the meantime, the pulverization of C_3S and C_2S diminished the amount of the residual pores.
- The augmented chloride contents of the deck with the ordinary concrete were appreciably more than those of the deck with UHPC; as a result, the corrosion initiation time of the former was estimated to be as early as 6.5 years, which was much shorter than the initiation time of the latter showing over 100 years. The proposed performance levels are expected to assist field engineers in inspecting constructed bridge decks exposed to deicing chemicals.

References

AASHTO. 2020. AASHTO LRFD bridge design specifications (9th edition), American Association of State Highway Transportation Officials, Washington, D.C

ACI. 2002. Standard practice for selecting proportions for normal, heavyweight, and mass concrete (ACI 211.1-91: reapproved 2002), American Concrete Institute, Farmington Hills, MI.

ACI. 2018. Ultra-high performance concrete: an emerging technology report (ACI 239R-18), American Concrete Institute, Farmington Hills, MI.

ACI. 2019. Building code requirements for structural concrete and commentary (ACI 318-19), American Concrete Institute, Farmington Hills, MI.

Akhoondan, M. and Bell, G.E.C. (2016), Fastener corrosion, Structure, 13(3), 74-75

Alkaysi, M. 2016. Strength and durability of ultra-high performance concrete materials and structures, PhD Dissertation, University of Michigan, Ann Arbor, MI.

Alkaysi, M., El-Tawil, S., Liu, Z., and Hansen, W. 2016. Effects of silica powder and cement type on durability of ultra high performance concrete (UHPC), Cement and Concrete Composites, 66, 47-56.

Anastasiou, E.K. 2021. Effect of high calcium fly ash, ladle furnace slag, and limestone filler on packing density, consistency, and strength of cement pastes. Materials, 14, 301.

ASTM. 2019. Standard test method for electrical indication of concrete's ability to resist chloride ion penetration (ASTM C1202-19), ASTM International, West Conshohocken, PA.

Babaei, S., Seetharam, S.C., Dizier, A., Steenackers, G., Craeye, B. 2021. Permeability of cementitious materials using a multiscale pore network model, Construction and Building Materials, 312, 125298.

Bajaber, M.A. and Hakeem, I.Y. 2021. UHPC evolution, development, and utilization in construction: a review, Journal of Materials Research and Technology, 10, 1058-1074.

Bentz, D.P. 1995. A three-dimensional cement hydration and microstructure program: I. hydration rate, heat of hydration, and chemical shrinkage, Report No. NISTIR 5756, National Institute of Standards and Technology, Gaithersburg, MD.

Bhaskar, S., Ramesh, G., and Bharatkumar, B.H. 2020. A review on performance-based specifications toward concrete durability, Structural Concrete, 22(5), 2526-2538.

Bhattacharya, M. and Harish, K.V. 2018. An integrated approach for studying the hydration of portland cement systems containing silica fume, Construction and Building Materials, 188, 1179-1192.

Bourchy, A., Barnes-Davin, L., Bessette, L., and Torrenti, J.M. 2020. Effect of cement composition on fresh state and heat of hydration of Portland cement with limestone and slag, ACI Materials Journal, 117(1), 153-165.

Brown, L.S. and Carson, Petrographic studies of hydrated cements, Proceedings of ASTM, 36, 332-350.

Bullard, J.W. 2014. Virtual Cement and Concrete Testing Laboratory: version 9.5 user guide, National Institute of Standards and Technology, Gaithersburg, MD.

Byfors, K. 1987. Influence of SF and flyash on chloride diffusion and pH values in cement paste, Cement and Concrete Research, 17(1), 115-130.

Chen, B. and Razaqpur, A.G. 2021. Effect of sub-zero versus sub-freezing temperature on chloride diffusion and binding in concrete, Construction and Building Materials, 287, 123057.

Estes, A. C., and Frangopol, D. M. 1999. Repair optimization of highway bridges using system reliability approach, Journal of Structural Engineering, 125(7), 766-775.

Fan, D., F., Yu, R., Shui, Z., Wu, C., Wang, J., and Su, Q. 2020. A novel approach for developing a green Ultra-High PerformanceConcrete (UHPC) with advanced particles packing meso-structure, Construction and Building Materials, 265, 120339.

Felix, F., Fraaij, A.L.A., and Hendriks, C.F. 1997. Inorganic immobilisation of waste materials, Studies in Environmental Science, 71, 769-780.

Fukuhara, M., Goto, S., Asaga, K., Daimon, M., and Kondo, R. 1981. Mechanisms and kinetics of C_4AF hydration with gypsum, Cement and Concrete Research, 11, 407-414.

Geiker, M.R., Hendriks, M.A.N., and Elsener, B. 2021. Durability-based design: the European perspective, Sustainable and Resilient Infrastructure, 1-16.

Granju, J.L. and Grandet, J. 1988. Characterization of the hydration state of Portland cement pastes, Cement and Concrete Research, 18, 886-894.

Kadri, E.H. and Duval, R. 2009. Hydration heat kinetics of concrete with silica fume, Construction and Building Materials, 23(11), 3388-3392.

Kim, G.-Y., Lee, E.-B., Nam, K.-M., and Koo, K.-M. 2011. Analysis of hydration heat and autogenous shrinkage of high-strength mass concrete, Magazine of Concrete Research, 63(5), 377-389.

Kim, J.J., Youm, K.-S., and Moon, J. 2020. A study on conversion fraction and carbonation of Pozzolan blended concrete through Si MAS NMR analysis, Applied Sciences, 10, 6855.

Kim, Y., Park, W., and Hanif, A. 2019. Steam-cured recycled aggregate concrete incorporating moderately high early strength cement: effect of binder content and curing conditions, Applied Sciences, 1, 445.

Li, L., Xia, J., and Lin, S. 2012. A multi-phase model for predicting the effective diffusion coefficient of chlorides in concrete, Construction and Building Materials, 26, 295-301.

Liu, Z., Xu, D., and Zhang, Y. 2017. Experimental investigation and quantitative calculation of the degree of hydration and products in fly ash-cement mixtures, Advances in Materials Science and Engineering, 2017, 1-12.

Liu, C., Wang, F., Zhang, M. 2020. Modelling of 3D microstructure and effective diffusivity of fly ash blended cement paste, Cement and Concrete Composites, 110, 103586

Liu, L., Sun, W., Ye, G., Chen, H., and Qian, Z. 2012. Estimation of the ionic diffusivity of virtual cement paste by random walk algorithm, Construction and Building Materials, 28, 405-413.

Lu, Z., Feng, Z.-G., Yao, D., Li, X., and Ji, H. 2021. Freeze-thaw resistance of Ultra-High performance concrete: Dependence on concrete composition, Construction and Building Materials, 293, 123523.

Macal, C.M. 2020. Agent-based modeling and artificial life, Complex Social and Behavioral Systems, Springer.

Matos, A.M., Nunes, S., Costa, C., Aguiar, J.L.B. 2021. Durability of an UHPC containing spent equilibrium catalyst, Construction and Building Materials, 305, 124681.

Omotoso, O.E., Ivey, D.G., and Mikula, R. 1995. Characterization of chromium doped tricalcium silicate using SEM/EDS, XRD and FTIR, Journal of Hazardous Materials, 42, 87-102.

Page, C.L., Short, N.R., and Tarras, A, E. 1981. Diffusion of chloride ions in hardened cement pastes, Cement and Concrete Research, 11, 395-406.

Pathirage, M., Bentz, D.P., Di Luzio, G., Masoero, E., and Cusatis, G. 2019. The ONIX model: a parameter-free multiscale framework for the prediction of self-desiccation in concrete, Cement and Concrete Composites, 103, 36-48.

Pierard, J., Dooms, B., and Cauberg, N. 2012. Evaluation of durability parameters of UHPC using accelerated lab tests, 3rd International Symposium on UHPC and Nanotechnology for High Performance Construction Materials, Kassel, Germany, 371-376.

Pignat, C., Navi, P., and Scrivener, K. 2005. Simulation of cement paste microstructure hydration, pore space characterization and permeability determination, Materials and Structures, 38, 459-466.

Pourjahanshahi, A. and Madani, H. 2021. Chloride diffusivity and mechanical performance of UHPC with hybrid fibers under heat treatment regime, Materials Today Communications, 26, 102146.

Richard, P. and Cheyrezy, M. 1994. Reactive powder concretes with high ductility and 200-800 MPa compressive strength, ACI Materials Journal, 144(3), 507-518.

Riding, K.A., Thomas, M.D.A., Hooton, R.D., Obla, K.H., and Weiss, W.J. 2018. Performance-based specifications for concrete exposed to chlorides, Concrete International, 40(7), 41-47.

Russell, H.G. and Graybeam, B.A. 2013. Ultra-high performance concrete: a state-of-the-art report for the bridge community, Report No. FHWA-HRT-13-060, Federal Highway Administration, Washington, D.C.

Shi, C., Wu, Z., Xiao, J., Wang, D., Huang, Z., and Fang, Z. 2015. A review on ultra high performance concrete: Part I. Raw materials and mixture design, Construction and Building Materials, 101, 741-751.

Standards Australia. 2007. Specification and supply of concrete (AS1379-2007), Standards Australia, Sydney, Australia.

Stewart, M.G. and Rosowsky, D.V. 1998. Time-dependent reliability of deteriorating reinforced concrete bridge decks, Structural Safety, 20(1), 91-109.

Sun, Y., Zhang, P., Guo, W., Bao, J., and Qu, C. 2020. Effect of nano-CaCO3 on the mechanical properties and durability of concrete incorporating fly ash, Advances in Materials Science and Engineering, 2020, 7365862.

Qi, T., Zhou, W., Liu, X., Wang, Q., and Zhang, S. 2021. Predictive hydration model of portland cement and its main minerals based on dissolution theory and water diffusion theory, Materials, 14(3), 595.

Riding, K. A., Poole, J.L., Folliard, K.J., Juenger, M.C., and Schindler, A.K. 2012. Modeling hydration of cementitious systems, ACI Materials Journal, 109(2), 225-234.

Sanchez, T., Conciatori, D., Laferriere, F., and Sorelli, L. 2020. Modelling capillary effects on the reactive transport of chloride ions in cementitious materials, Cement and Concrete Research, 131, 106033.

Schmid, M., Pichler, C., and Lackner, R. 2019. Engineering hydration model for ordinary Portland cement based on heat flow calorimetry data, Journal of Thermal Analysis and Calorimetry, 138, 2283-2288.

Shafikhani, M., and Chidiac, S.E. 2020. A holistic model for cement paste and concrete chloride diffusion coefficient, Cement and Concrete Research, 133, 106049.

Shama, A. and Jones, M. 2020. Seismic performance-based design of cable-supported bridges: state of practice in the United States, Journal of Bridge Engineering, 25(12), 04020101.

Siddiqui, A.A., Ewer, J.A., Lawrence, P.J., Galea, E.R., and Frost, I.R. 2021. Building information modelling for performance-based fire safety engineering analysis- a strategy for data sharing, Journal of Building Engineering, 42, 102794.

Srikanth, I. and Arockiasamy, M. 2020. Deterioration models for prediction of remaining useful life of timber and concrete bridges: a review, Journal of Traffic and Transportation Engineering, 7(2), 152-173.

Stewart, M.G. and Val, D.V. 1999. Role of load history in reliability-based decision analysis of aging bridges, Journal of Structural Engineering, 125(7), 776-783.

Sun, G., Zhang, Y., Sun, W., Liu, Z., and Wang, C. 2011. Multi-scale prediction of the effective chloride diffusion coefficient of the concrete, Construction and Building Materials, 25, 3820-3831.

Tang, L., and Nilsson L. 1992. Rapid determination of the chloride diffusivity in concrete by applying an electrical field, ACI Materials Journal, 89(1), 49-53

Tang, Y., Xu, G., Lian, J., Su, H., and Qu, C. 2016. Effect of temperature and humidity on the adhesion strength and damage mechanism of shotcrete-surrounded rock, Construction and Building Materials, 124, 1109-1119.

Tavares, L.R.C., Tavares, J.F., Costa, L.M., da Silva Bezerra, A.C., Cetlin, P.R., and Aguilar, A.M.T. 2020. Influence of quartz powder and silica fume on the performance of Portland cement, Scientific Reports 10, 21461.

Taylor, H.F.W. 1990. Cement chemistry, Academic Press, London, UK.

Thomas, M., Green, B., O'Neal, E., Perry, V., Hayman, S., and Hossack, A. 2012. Marine performance of UHPC at Treat Island. 3rd International Symposium on UHPC and Nanotechnology for High Performance Construction Materials, Kassel, Germany, 365-370.

Tikalsky, P.J., Pustka, D., and Marek, P. 2005. Statistical variations in chloride diffusion in concrete bridges, ACI Structural Journal, 102(3), 481-486.

Torrent, R.J., Neves, R.D., and Imamoto, K.-I. 2022. Concrete permeability and durability performance from theory to field applications, CRC Press, Boca Raton, FL.

Wang, X.-Y. 2014. Properties prediction of ultra high performance concrete using blended cement hydration model, Construction and Building Materials, 64, 1-10.

Weast, R.C. 1976. Handbook of chemistry and physics (57th Edition), CRC Press, Cleveland, OH.

Wilensky, U. and Rand, W. 2015. An introduction to agent-based modeling, MIT Press, Cambridge, MA.

Wille, K., Naaman, A.E., EI-Tawil, S., and Parra-Montesinos, G.J. 2012. Ultra-high performance concrete and fiber reinforced concrete: achieving strength and ductility without heat curing, Materials and Structures, 45, 309-324.

Wong, H.S., Zhao, Y.X., Karimi, A.R., Buenfeld, N.R., and Jin, W.L. 2010. On the penetration of corrosion products from reinforcing steel into concrete due to chloride-induced corrosion, Corrosion Science, 52, 2469-2480.

Yajun, J. and Cahyadi, J.H. 2004. Simulation of SF blended cement hydration, Materials and Structures, 37, 397-404.

Yalcinkaya, C. and Copuroglu, O. 2021. Hydration heat, strength and microstructure characteristics of UHPC containing blast furnace slag, Journal of Building Engineering, 34, 101915.

Young, J.F. 1972. A review of the mechanisms of set-retardation in Portland cement pastes containing organic admixtures, Cement and Concrete Research, 2(4), 415-433.

Yu, H., Tan, Y., and Feng, T. 2019. Study of temporal change in chloride diffusion coefficient of concrete, ACI Materials Journal, 116(1), 103-112.

Zhang, G., Yang, G. Li, S., Shen, Q., Wang, H., Li, Z., Zhou, Y., and Ye, W. 2021. Effects of hydration and temperature on the microstructure and transport properties of Nafion polyelectrolyte membrane: a molecular dynamics simulation, Membranes, 11, 11090695.

Zhang, L. and Zhou, J. 2020. Fractal characteristics of pore structure of hardened cement paste prepared by pressurized compact molding, Construction and Building Materials, 259, 119856.

Zhang, W., Gu, X., Qiu, J., Liu, J., Zhao, Y., and Li, X. 2020. Effects of iron ore tailings on the compressive strength and permeability of ultra-high performance concrete, Construction and Building Materials, 260, 119917.

Zhang, Y., Ye, G., and Yang, Z. 2020. New insights into long-term chloride transport in unsaturated cementitious materials: Role of degree of water saturation, Construction and Building Materials, 238, 117677.

Zhou, Y., Gencturk, B., Willam, K., and Attar, A. 2015. Carbonation-induced and chloride-induced corrosion in reinforced concrete structures, Journal of Materials in Civil Engineering, 27(9), 04014245.

Zhu, Y., Zhang, Y., Hussein, H., and Chen, G. 2020. Flexural strengthening of reinforced concrete beams or slabs using ultra-high performance concrete (UHPC): a state of the art review, Engineering Structures, 205, 110035.

Table I.1. Relative mass of ingredients in concrete mixtures

Component	Ordinary concrete				UHPC			
f'_c (MPa)	30	35	40	45	149	158	160	164
w/b	0.54	0.47	0.42	0.37	0.18	0.16	0.15	0.14
Water	0.54	0.48	0.42	0.37	0.22	0.20	0.19	0.18
Cement	1	1	1	1	1	1	1	1
Fine aggregate	1.9	1.57	1.31	1.03	1.38	1.01	1.03	1.05
Coarse aggregate	3.20	2.82	2.51	2.18	-	-	-	-
Silica fume	-	-	-	-	0.25	0.25	0.25	0.25
Silica powder	-	-	-	-	0.25	0.25	0.25	0.25

f'_c = compressive strength of concrete; w/b = water-binder (cement) ratio

Table I.2. Cement phases in mass percent

Phase	Ordinary concrete	UHPC
C_3S	69.6	78.7
C_2S	12.9	14.9
C_3A	11.2	5.3
C_4AF	6.3	1.1

Table I.3. Performance-based design for durability under deicing condition

Concrete		Cover depth (mm)	Tolerable time (years)		
Type	f'_c (MPa)		Level I (Satisfactory) (Cl. ≤ 0.8 kg/m^3)	Level II (Operational) (0.8 kg/m^3 < Cl. ≤ 2 kg/m^3)	Level III (Critical) (2 kg/m^3 < Cl.)
Ordinary concrete	30	50	≤ 5	> 5 and < 43	43 ≤
		75	≤ 16	16 <	N/A
	35	50	≤ 14	14 <	N/A
		75	≤ 42	42 <	N/A
	40	50	≤ 18	18 <	N/A
		75	≤ 55	55 <	N/A
	45	50	≤ 39	39 <	N/A
		75	-	-	N/A
UHPC	149	50	≤ 81	81 <	N/A
		75	N/A	N/A	N/A
	158	50	N/A	N/A	N/A
		75	N/A	N/A	N/A
	160	50	N/A	N/A	N/A
		75	N/A	N/A	N/A
	164	50	N/A	N/A	N/A
		75	N/A	N/A	N/A

f'_c = compressive strength; Cl. = chloride contents; N/A = not applicable

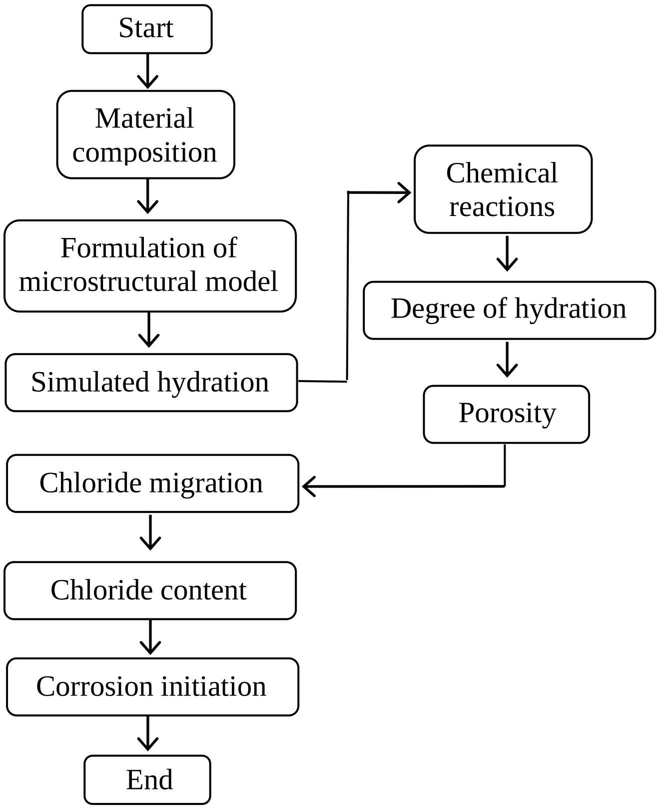

Fig. I.1. Overview of modeling approach

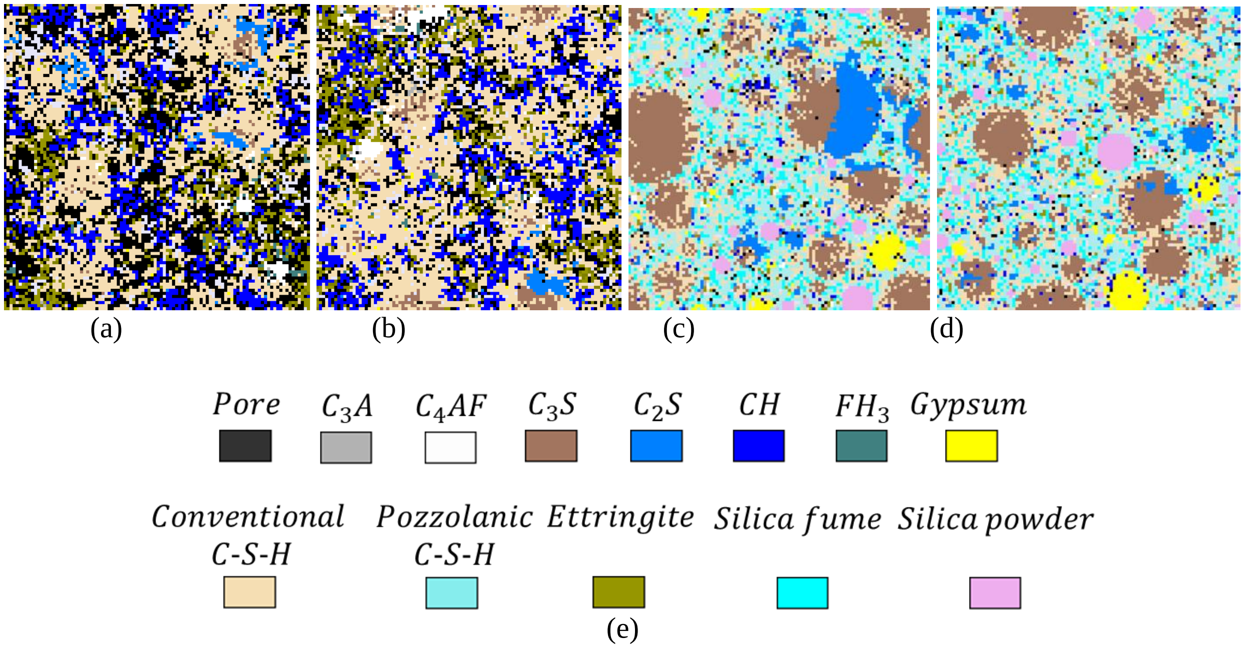

Fig. I.2. Microstructural model of concrete at 28 days (cross-sectional view): (a) ordinary concrete at f'_c = 30 MPa; (b) ordinary concrete at f'_c = 45 MPa; (c) UHPC at f'_c = 149 MPa; (d) UHPC at f'_c = 164 MPa; (e) chemical components

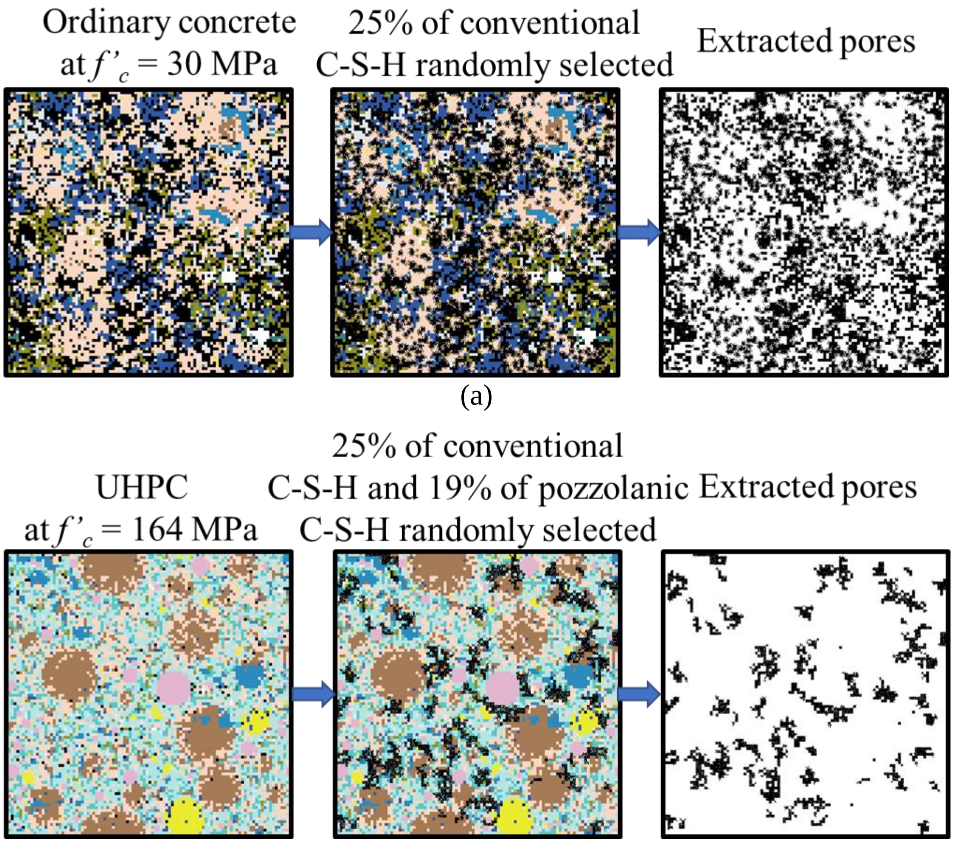

(a)

(b)

Fig. I.3. Determination of capillary and gel pores: (a) ordinary concrete at f'_c = 30 MPa; (b) UHPC at f'_c = 164 MPa

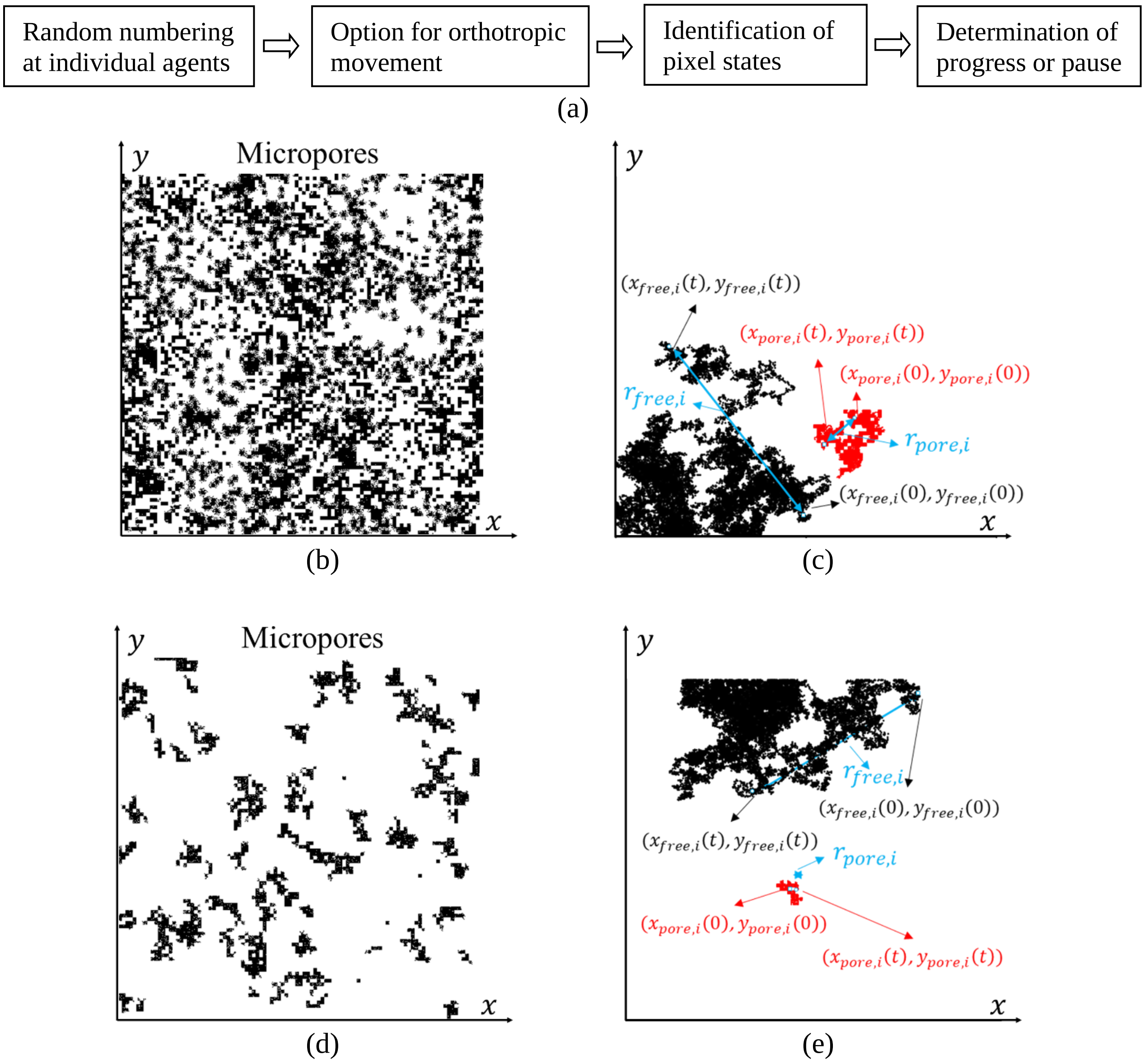

Fig. I.4. Random walk for chloride migration through micropores: (a) algorithm; (b) pore space of ordinary concrete at f'_c = 30 MPa; (c) random movement of chloride ions in ordinary concrete at f'_c = 30 MPa; (d) pore space of UHPC at f'_c = 164 MPa; (e) random movement of chloride ions in UHPC at f'_c = 164 MPa

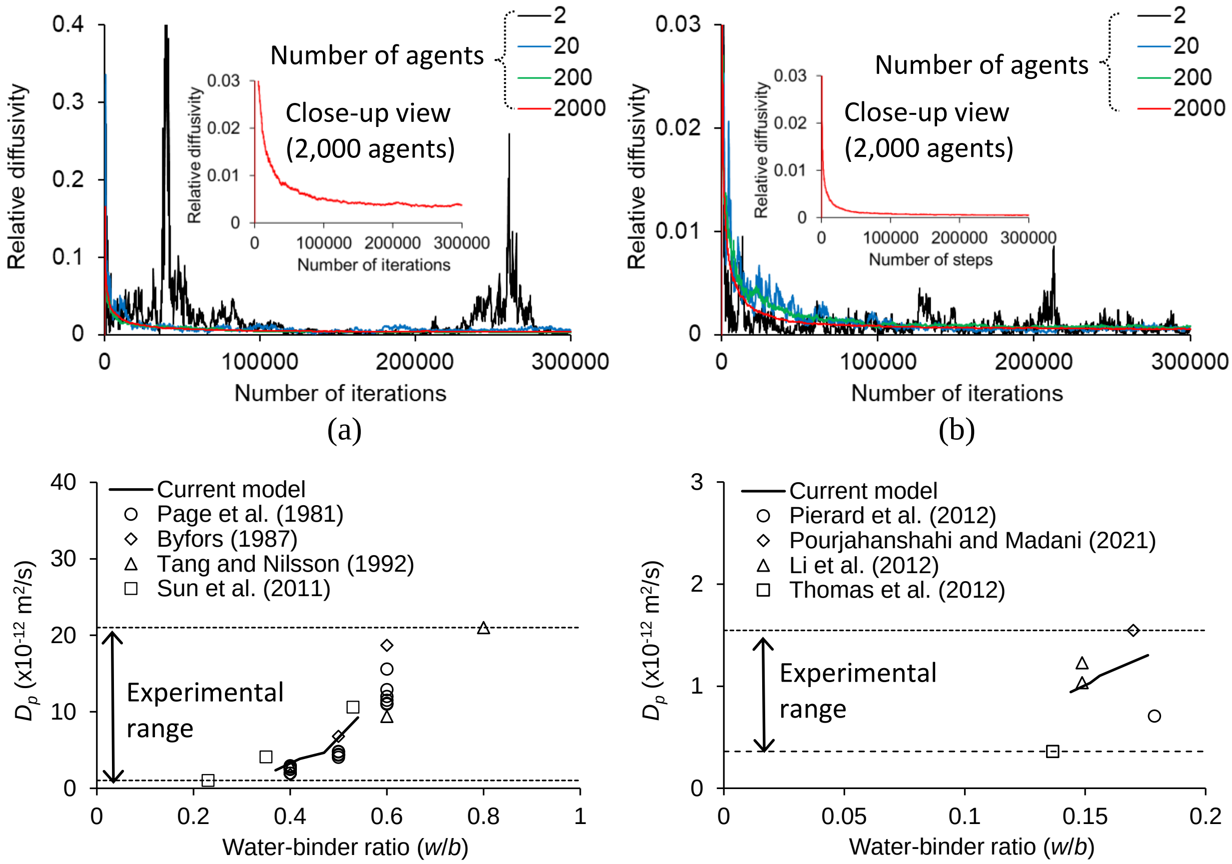

(a) (b)

(c) (d)

Fig. I.5. Assessment of modeling approaches: (a) convergence of relative diffusivity (D_p/D_{free}) for paste of ordinary concrete at f'_c = 30 MPa; (b) convergence of relative diffusivity (D_p/D_{free}) for paste of UHPC at f'_c = 164 MPa; (c) diffusion coefficient of ordinary concrete; (d) diffusion coefficient of UHPC

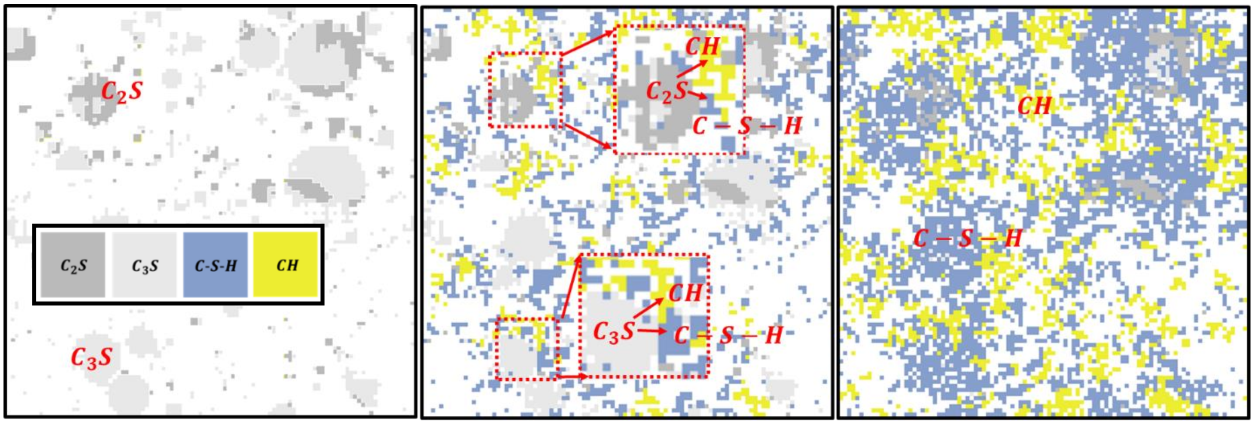

0 days

1 day

28 days

Fig. I.6. Silicate reactions in paste of ordinary concrete at *f'c* = 30 MPa with close-up views

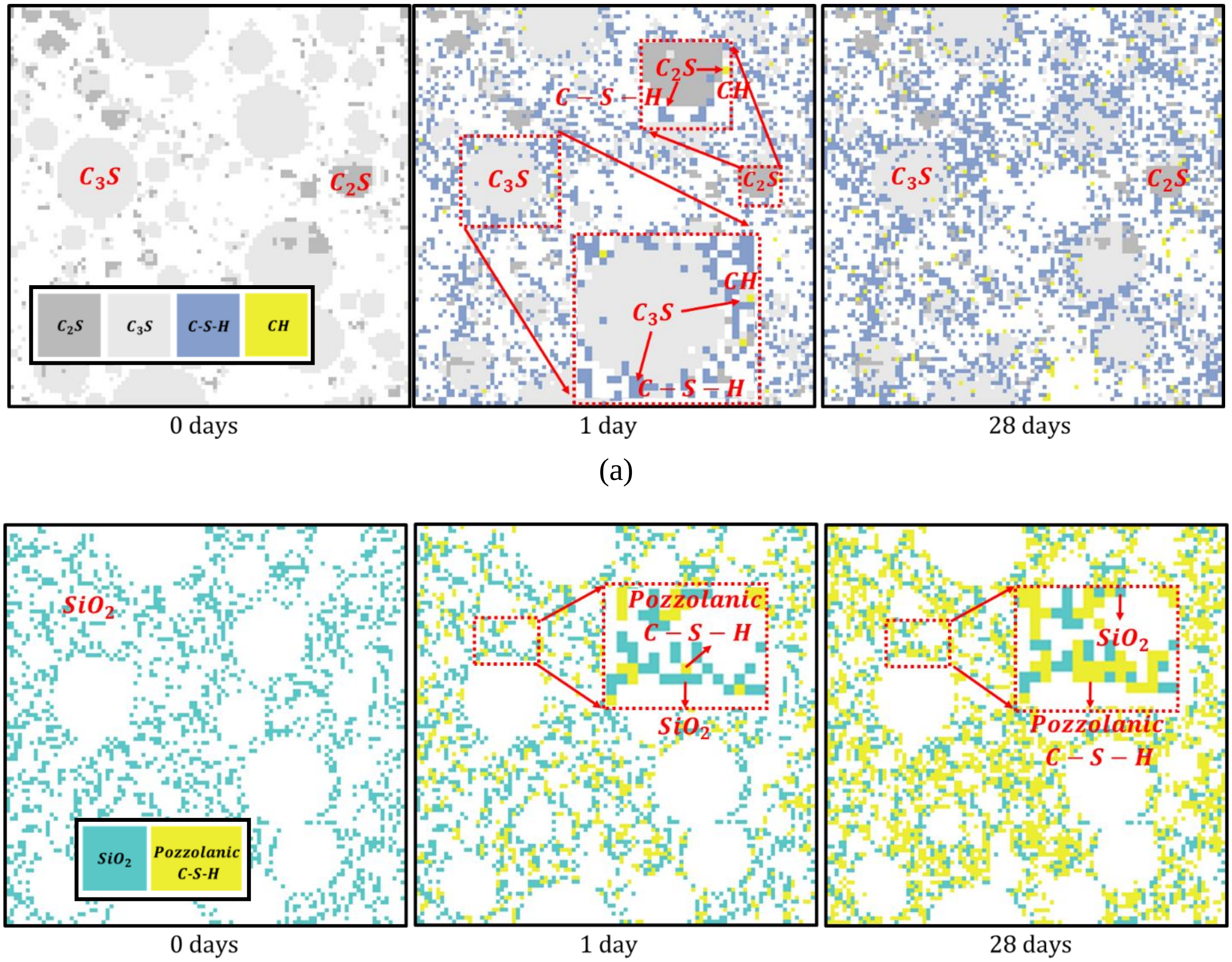

(a)

(b)

Fig. I.7. Chemical reactions of UHPC at f'_c = 164 MPa with close-up views: (a) silicate reactions; (b) pozzolanic reactions

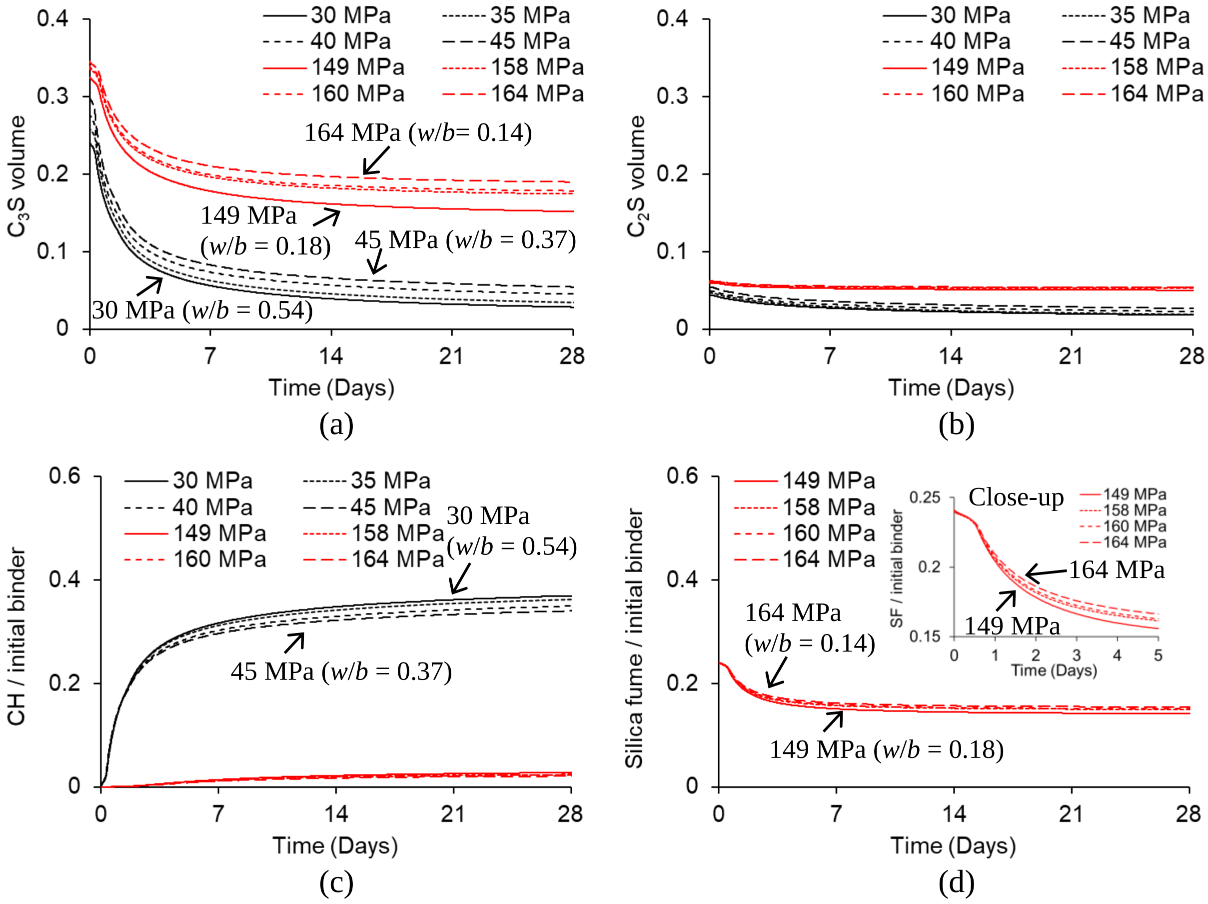

Fig. I.8. Development of major compounds during chemical reactions: (a) tricalcium silicate; (b) dicalcium silicate; (c) calcium hydroxide divided by initial binder volume; (d) silica fume divided by initial binder volume

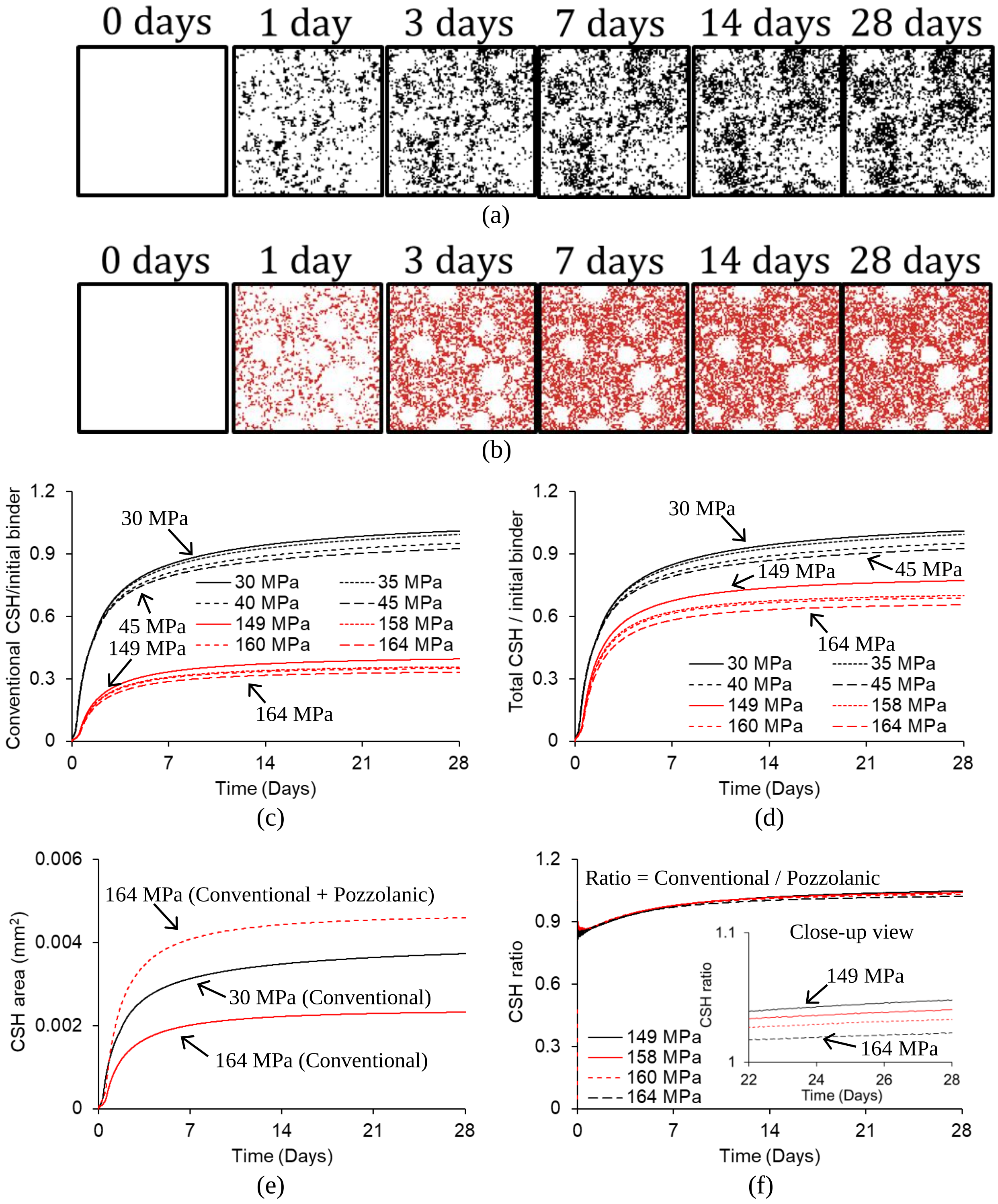

Fig. I.9. Temporal characteristics of reaction compounds: (a) calcium silicate hydrate of ordinary concrete at f'_c = 30 MPa; (b) total calcium silicate hydrate of UHPC at f'_c = 164 MPa; (c) conventional calcium silicate hydrate divided by initial binder volume; (d) total calcium silicate hydrate divided by initial binder volume; (e) calcium silicate hydrate areas; (f) ratio between conventional and pozzolanic C-S-H components in UHPC

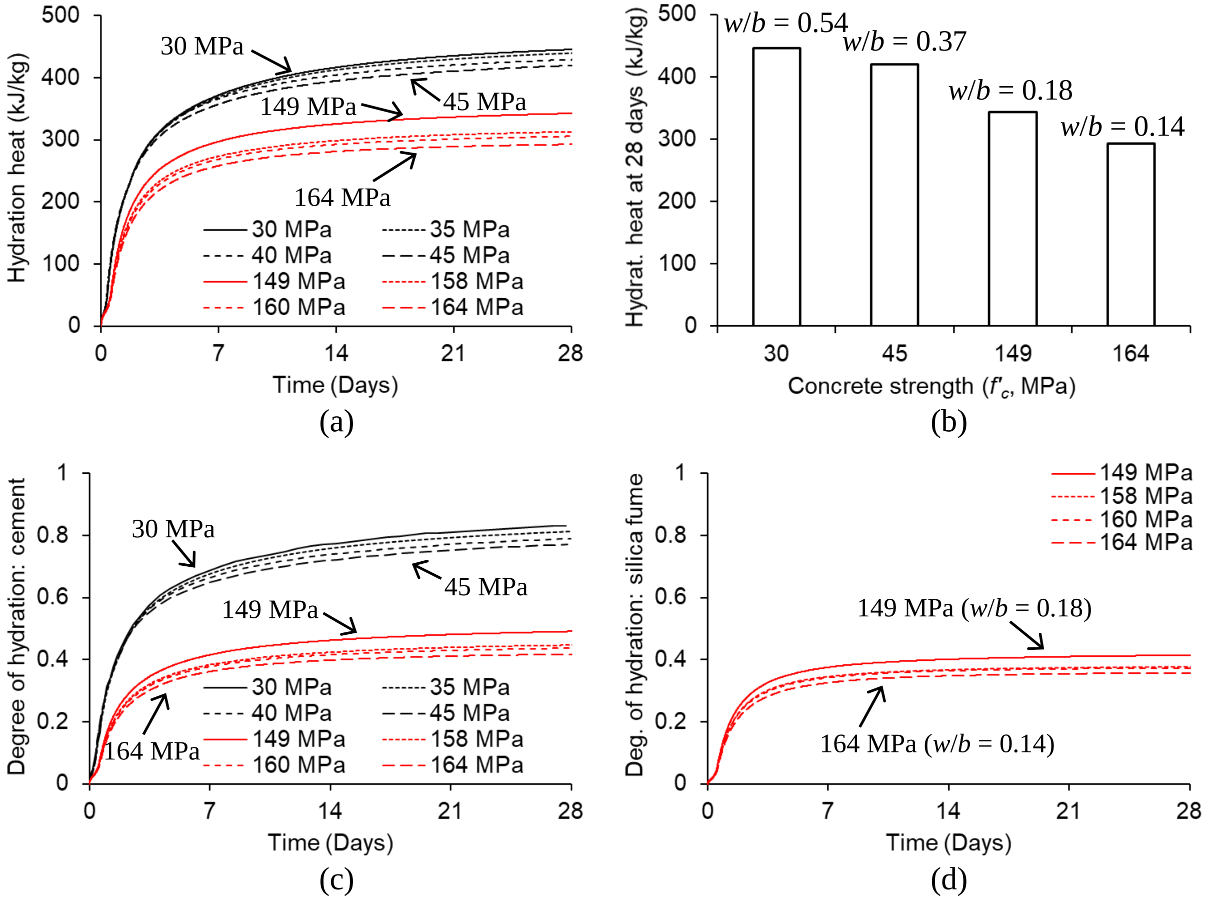

Fig. I.10. Progression of hydration: (a) total heat; (b) heat at 28 days; (c) cement; (d) silica fume

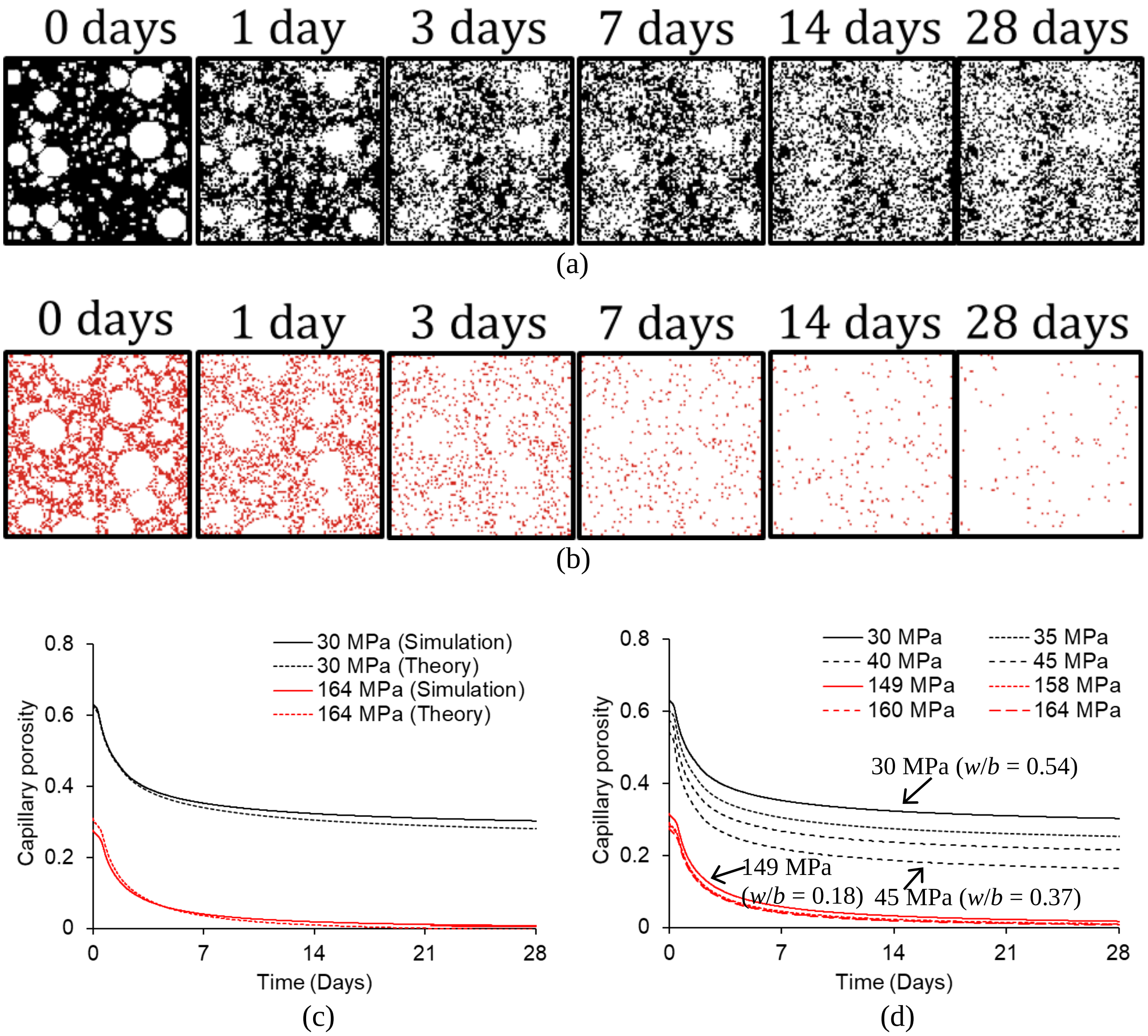

Fig. I.11. Evolution of capillary pores: (a) ordinary concrete at f'_c = 30 MPa; (b) UHPC at f'_c = 164 MPa; (c) comparison with theory; (d) progression

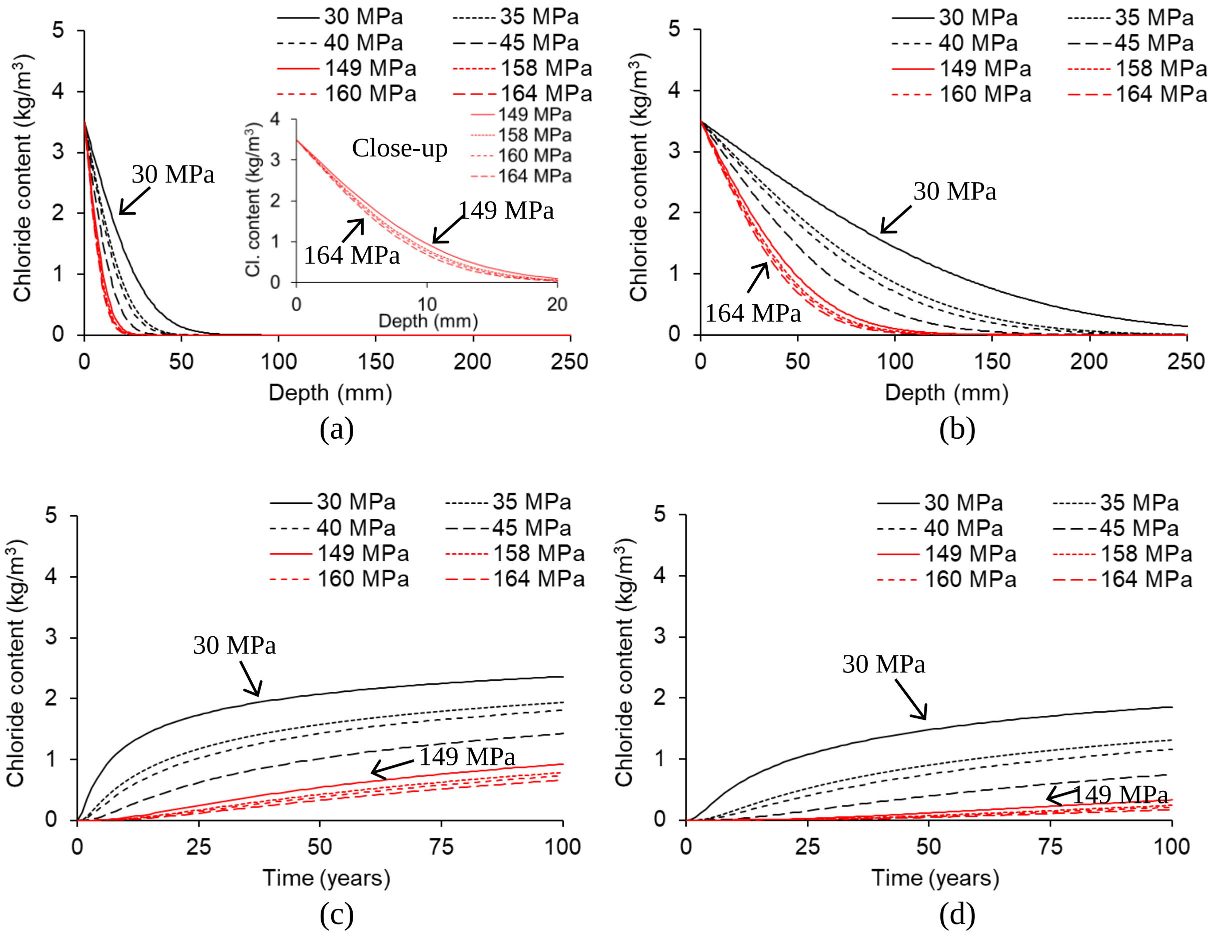

Fig. I.12. Chloride content: (a) across concrete member at 1 year; (b) across concrete member at 1 00 years; (c) at cover depth of 50 mm from concrete surface; (d) at cover depth of 75 mm from concrete surface

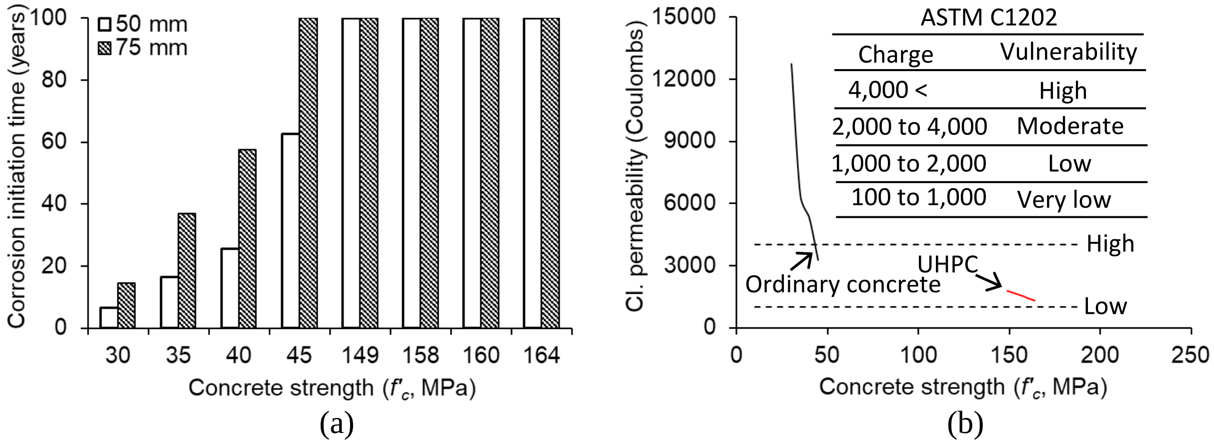

Fig. I.13. Performance-based durability: (a) corrosion initiation time; (b) chloride permeability

Part II: Cellular Automata for Corrosion in CFRP-Strengthened Bridge Columns

II.1. Introduction

Corrosion is prevalent in built-environments, such as parking garages to highway bridges, and often accompanied by a significant economic impact. It is estimated that more than 3% of the global Gross Domestic Product (GDP), equivalent to $2.5 trillion, is spent due to corrosion (Koch et al. 2016). These dollar amounts could include all major aspects of design, construction, and maintenance concerning the corrosion problems of facilities. Corrosion-induced damage often leads to the failure of concrete members, especially when deicing agents are excessively used (Debaiky et al. 2002). When iron-oxide residues surround steel bars, internal pressure causes cracking in the concrete cover (Nossoni 2015) through which detrimental chemicals propagate, thereby accelerating the deterioration process, and eventually spalling the cracked concrete (Chen et al. 2019). Partially submerged bridge columns are vulnerable to corrosion because wet-dry cycles periodically supply moisture and oxygen (Hussain et al. 2020). The loss of a column section degrades both strength and ductility (Hamilton et al. 2004); hence, preserving the integrity of structural configurations is an important requirement from a functional standpoint. As far as load-bearing members are concerned, accelerated bridge construction (ABC) is increasingly employed in the infrastructure community, which is a state-of-the-art concept integrating all major aspects of highway bridges. By erecting prefabricated members, transportation agencies benefit from project delivery time, on-site safety, and traffic interruption (Khan 2014). The majority of ABC-related research has been focused on seismic responses (Zhang and Alam 2020); accordingly, little is known about other subjects. For example, supported by the fact that the durability of cast-in-place and ABC columns may not be the same on account of different quality control procedures, the need for investigations into corrosion-induced damage in ABC columns was raised recently (Liu and Palermo 2020). Concrete patching and jacketing are traditional repair methods for impaired columns (Grantham et al. 2012), whereas the formation of incipient anodes elevates the likelihood of recurring corrosion problems (Christodoulou et al. 2013). In addition, those repairs are labor-intensive and demand considerable preparation for cage fabrication, form assembly, and casting (Hamilton et al. 2004; Bousias et al. 2007).

Wrapping with carbon fiber reinforced polymer (CFRP) sheets is an effective approach to upgrade the capacity and ductility of a damaged column by reducing direct exposure to chlorides and minimizing potential corrosion activities in steel reinforcement (ElMaaddawy et al. 2006). When repairing columns possessing disintegrated concrete, surface-preparation should be preceded with a cementitious patching material before applying CFRP in order to warrant even pressure distributions along the substrate (ACI 2017). It is necessary to maintain adequate contacts between the concrete and CFRP; otherwise, moisture and chemicals can infiltrate into the locally debonded gap and promote corrosion in the repaired columns. Debaiky et al. (2002) tested corrosion rates in reinforced concrete columns with and without CFRP-wrapping. Electrochemical reactions were monitored by the half-cell potential and linear polarization resistance techniques. With one and two layers of CFRP, the corrosion current density of the columns decreased from 10 $\mu A/cm^2$ to 0.1 $\mu A/cm^2$. Based on oxygen diffusion and cathodic reactions, Nossoni (2015) developed an analytical model to predict the implications of CFRP-wrapping in a corrosive environment. For representing actual site conditions that bring about corrosion, the core of a concrete column was assumed to contain a sufficient amount of chloride before repair. After wrapping with CFRP, a low corrosion rate was noticed in comparison to unconfined specimens and the longevity of the column was extended. Amran et al. (2020) reported moisture permeability in CFRP-wrapped concrete, which controlled the degree of corrosion. Pursuant to ASTM C1585 (ASTM 2004), permeability coefficients were measured and an empirical expression was proposed. Compared with plain concrete, the presence of CFRP layers significantly lowered the permeability, contingent upon the number of bonded layers. Although CFRP-wrapping was not yet utilized for repairing deteriorated ABC columns, possibly ascribing to their relatively short application history, this rehabilitation method can be applicable to such bridge elements and a precedent assessment would be of interest.

This report discusses the ramifications of corrosion in the simulated performance of cast-in-place and ABC columns under various exposure conditions. Cellular automata, an evolutionary mathematics approach, are adopted to simulate the intricate progression of diffusive chlorides via mutual interactions among multiple discrete entities controlling regional responses, which are instrumental in determining the global behavior of the deteriorated columns. Additionally, the efficacy of CFRP-wrapping is examined with a focus on strength recovery and reductions in chloride ingress rate.

II.2. Benchmark Column

Pursuant to the American Association of State Highway and Transportation Officials (AASHTO) Load and Resistance Factor Design (LRFD) Bridge Design Specifications (BDS) (AASHTO 2020), a simulated two-column bridge pier is designed to support a two-span concrete box girder bridge. Described below are the materials and structural details of the column exposed to aggressive service environments, and a CFRP-strengthening technique for restoring a capacity loss caused by corrosion damage.

II.2.1. Outline and Parameters

The benchmark column was a circular shape with a diameter of ϕ = 1,070 mm at a length of 5.3 m. Each of No. 14 Grade 60 reinforcements (d_b = 43 mm, where d_b is the nominal diameter, with a yield strength of f_y = 414 MPa) had a cross-sectional area of A_s = 1,452 mm^2, and 12 rebars were distributed around the column section (Fig. II.1(a)). It was assumed that transverse ties were adequately placed to prevent the local buckling of the longitudinal rebars. In view of practical significance, a variable range of concrete strength was used from f'_c = 30 MPa to 45 MPa. Table II.1 enumerates the ingredients of the concrete mixtures based on ACI 211.1-91 (ACI 2002), which were necessary for modeling chloride migration. The cover depth of the column (Table II.2) was assigned as specified in AASHTO LRFD BDS (AASHTO 2020) along with modification factors in relation to the water-to-cement ratio (*wc*) of the concrete (Table II.1). Regarding the construction of the column, cast-in-place and ABC methods were taken into consideration.

II.2.2. Service Condition

In compliance with NACE SP0176-2007-SG (NACE 2007), the column was exposed to three service environments: atmospheric, splash, and submerged zones (Fig. II.1(b)). The atmospheric zone is not wet, but airborne chlorides permeate the column concrete. The splash zone suffers from the continual fluctuation of water level, accelerating the adverse consequences of wet-dry cycles in tandem with capillary suction and diffusion (Gao et al. 2013). The submerged zone is permanently saturated and electrochemical reactions among chlorides, electrolytes, and dissolved oxygen facilitate a corrosion process (Eyu et al. 2017). The performance of the column under those simulated corrosive environments was examined for 100 years, which can fully cover the design life of 75 years in AASHTO LRFD BDS (AASHTO 2020). It is noteworthy to mention that the 75-year design life was conservatively taken because the actual service life of bridge structures is generally longer than 100 years.

II.2.3. CFRP-Strengthening

The provisions of ACI 440.2R-17 (ACI 2017) were referenced to strengthen the corrosion-damaged column

$$f'_{cc} = f'_{c} + \psi_f 3.3\kappa_a f_l \tag{II.1}$$

$$f_l = \frac{2E_f n t_f \varepsilon_{fe}}{\phi} \tag{II.2}$$

where f'_{cc} is the compressive strength of the confined concrete; ψ_f is the reduction factor ($\psi_f = 1$ for a nominal capacity prediction); κ_a is the efficiency factor ($\kappa_a = 1$ for a circular section); f_l is the confining pressure; E_f, n, and t_f are the elastic modulus, number of plies, and thickness of CFRP, respectively; and ε_{fe} is the effective CFRP strain ($\varepsilon_{fe} = 0.55\varepsilon_{fu}$, in which ε_{fu} is the rupture strain). Commercially available CFRP sheets, consisting of unidirectional carbon fibers and an epoxy resin, were used with the following properties: ultimate strength (f_{fu}) = 3,800 MPa, E_f = 227 GPa, ε_{fu} = 0.0167, and t_f = 0.165 mm. The damaged column was confined at a capacity loss of 10% and the strengthening effect was maintained up to 100 years (illustrative explanations will be given).

II.3. Theoretical Modeling

A modeling approach is elaborated on the initiation and progression of corrosion in the benchmark column and corresponding structural responses. The interdependency of axial load and bending moment is delineated for the prediction of the column capacity when linked with unfavorable operational environments.

II.3.1. Cellular Automata

Cellular automata are a branch of computational mathematics, which are intended to understand the complexity of discrete dynamical systems (Wolfram 1984). The architecture of cellular automata comprises an array of multiple grids in a finite dimension, responding to a preset rule that defines a relationship between adjacent cells. With an increase in time, the assembled cohort evolves with the absence of a governing entity at the global level (that is, the engagement of the constituting cells is completely autonomous) and a generalized pattern is manifested. For the present numerical study, the von Neumann neighborhood with orthogonal cells (Wolnik and Baets 2020) was chosen to simulate the migration of chlorides in the column concrete. Further information on the development, principle, and application of cellular automata is available elsewhere (Hoekstra et al. 2010; Baetens and Kutrib 2018).

II.3.2. Chloride Diffusion

II.3.2.1. Kinetics

Diffusive interactions among discrete cells may be represented by Fick's second law

$$\frac{\partial C}{\partial t} = D\frac{\partial^2 C}{\partial^2 x^2} \tag{II.3}$$

where C is the chloride concentration at position x and time t; and D is the diffusion coefficient. Conforming to the von Neumann's square lattice (Fig. II.2(a)), the concentration of the center cell at time t+1 ($C_{x,y}(t+1)$) can be estimated by (Podrouzek and Teply 2008)

$$C_{x,y}(t+1)=\Phi_1 C_{x,y}(t)+\Phi_2 C_{x,y-1}(t)+\Phi_3 C_{x+1,y}(t)+\Phi_4 C_{x,y+1}(t)+\Phi_5 C_{x-1,y}(t) \quad \text{(II.4)}$$

$$\sum_{i=1}^{5}\Phi_i=1 \quad \text{(II.5)}$$

where x and y are the abscissa and ordinate of the two-dimensional space, respectively, and Φ_i is the evolutionary coefficient satisfying the principle of mass conservation (Eq. II.5). Assuming that the progression of chlorides is isotropic (Wang et al. 2018), Φ_1 = 0.5 for $C_{x,y}$ and $\Phi_{2,3,4,5}$ = 0.125 are suggested with Eq. II.6 (Podrouzek and Teply 2008)

$$\Delta t=\Phi_i\frac{\Delta s}{D} \quad \text{(II.6)}$$

where Δt is the time step and Δs is the size of the cell. The outbound coefficient Φ_6 from the center cell ($C_{x,y}$) is obtained by $\Phi_6 = (1 - \Phi_1)/4$. The initial and time-dependent diffusion coefficients ($D(0)$ and $D(t)$, respectively) of ordinary concrete may be determined by (Frederiksen et al. 2000; Poulsen and Mejlbro 2006)

$$D(0)=ke^{\left(-\sqrt{10/wc}\right)} \quad \text{(II.7)}$$

$$D(t)=D_e(0)t^{-\eta} \quad \text{(II.8)}$$

$$\eta=k_a(1-1.5wc) \quad \text{(II.9)}$$

where k and k_a are the service environment and adjustment factors, respectively (k = 10,000 mm^2/year and k_a = 1.0 for atmosphere, k = 15,000 mm^2/year and k_a = 0.1 for splash, and k = 25,000 mm^2/year and k_a = 0.6 for submerged conditions); and $D_e(t)$ is the diffusion coefficient under a specific exposure environment; and η is the age coefficient. Considering the different curing conditions of concrete between the cast-in-place and ABC columns, Eq. II.10 is adopted

$$D_e(0)=k_c D(0) \quad \text{(II.10)}$$

where k_c is the curing factor (k_c = 1 for the concrete that is moisture-cured for 28 days, representing ABC members, and k_c = 4.3, 2.8, and 2.7 for the cast-in-place concrete (cured under a typical site condition at a relative humidity of 40% to 50% and 19^{o}C to 23^{o}C) that is subsequently exposed to atmospheric, splash, and submerged conditions, respectively (Alizadeh et al. 2008).

II.3.2.2. Validation

The above-described approach was validated against other research programs (Cao et al. 2012; Titi and Biondini 2016; Wang et al. 2018; Yin and Pan 2020). According to the properties listed in Table II.3, chloride contents were computed at the respective chloride-exposure times and locations denoted in the cited literature (Fig. II.3). It should be noted that, for the purpose of consistency, the units of the contents were intentionally kept as presented in the literature. In spite of the marginal differences possibly due to randomly dispersed aggregates in the concrete specimens, the prediction was sufficiently close to the collated data.

II.3.3. Corrosion

II.3.3.1. Initiation

The corrosion initiation of the column may be attained by (Thoft-Christensen et al. 1996; Liu and Weyers 1998)

$$t_i = \frac{(c/10)^2}{4D}\left(erf^{-1}\left(\frac{C_{cr}-C_0}{C_i-C_0}\right)\right)^{-2} \text{ for atmospheric and submerged conditions} \qquad \text{(II.11a)}$$

$$t_i = \left(\frac{\ln(1.08 i_{corr}) - 8.37 - 0.618 \ln 1.69 C_f(t) + 3034/T + 0.000105 R_c}{2.32}\right)^{0.215} \text{ for splash} \qquad \text{(II.11b)}$$

where t_i is the initiation time; c is the concrete cover in mm; *erf* is the Gauss error function; C_{cr} and C_i are the critical and initial chloride concentrations, respectively (C_{cr} = 0.4% and C_i = 0% of the cement weight (Elsener and Angst 2016)); C_0 is the surface chloride concentration; i_{corr} is the corrosion current density (i_{corr} = 0.3 $\mu A/cm^2$ was adopted[42]); C_f is the free chloride concentration at the rebar level in kg/m^3; T is the absolute temperature at the surface of the rebar in Kelvin (T = 293.15K); and R_c is the resistance of the cover concrete in ohms (R_c = 1,500 ohms). For the atmospheric and submerged conditions, the surface chlorides were assumed to be constant (C_0 = 0.2% and 0.5% of the concrete weight, respectively (Roy et al. 1993)); however, for the splash exposure, variable chlorides were considered to reflect periodic wet-dry cycles with time t in years alongside the percent weight of the concrete (Song et al. 2008; Liu et al. 2020)

$$C_0(t) = (0.213wc + 0.134)t^{0.484} \qquad \text{(II.12)}$$

II.3.3.2. Progression

Upon initiation of corrosion damage, the cross-sectional area of the reinforcement is reduced (Val and Melchers 1997)

$$d_b(t) = d_{bo} - 0.0232(t - t_i)i_{corr} \qquad \text{(II.13)}$$

where $d_b(t)$ and d_{b0} are the diameter of the rebar at time t and its initial counterpart, respectively. The corrosion current density (i_{corr}) with increasing corrosion time t in years may be calculated using Eq. II.14 that was originated from 2,927 measured data at the surface of steel rebars for up to 5 years of outdoor exposure (Liu and Weyers 1998)

$$\ln(1.08 i_{corr}) = 8.37 + 0.618 \ln 1.69 C_f(t) - 3034/T - 0.000105 R_c + 2.32 t^{-0.215} \qquad \text{(II.14)}$$

Although Eq. II.14 is comprehensive, several limitations are acknowledged because it did not account for geometry, oxygen availability, the dynamic nature of corrosion, and other factors that influence corrosion rate. Since the free chlorides (C_f) affect the progression of corrosion, the total chlorides imparted from the cellular automata model (C_t) in kg/m^3 need to be converted (Cheewaket et al. 2010)

$$C_f = 0.8541 C_t \tag{II.15}$$

When the column is wrapped with CFRP, the ingress of chlorides is impeded and previous research demonstrates that the magnitude of the current density decreases by 1/3 (Suh et al. 2007).

II.3.3.3. Impaired Concrete

The volumetric expansion of the corroded rebars weakens the cover concrete of the column. For modeling convenience, the occurrence of cracking and spalling is frequently replaced by the equivalent compressive strength ($f_c^*(t)$) of the cover concrete (Vecchio and Collins 1986; Coronelli and Gambarova 2004)

$$f_c^*(t) = \frac{f_c'}{1 + k^* \varepsilon_1(t) / \varepsilon_{co}} \tag{II.16}$$

where k^* is the characteristic coefficient ($k^* = 0.1$); ε_{co} is the strain at the peak stress of the concrete ($\varepsilon_{co} = 0.002$); and $\varepsilon_1(t)$ is the average tensile strain of the cracked concrete (Coronelli and Gambarova 2004)

$$\varepsilon_1(t) = (n_b W_{cr}(t)) / \phi \tag{II.17}$$

where n_b is the number of the rebars in compression and $W_{cr}(t)$ is the average crack width in mm (Vidal et al. 2004)

$$W_{cr}(t) = K\left(\Delta A_s(t) - \Delta A_{so}\right) \tag{II.18}$$

where K is an empirical factor ($K = 0.00575$/mm); $\Delta A_s(t)$ is the cross-sectional loss of the rebars in mm^2; and ΔA_{so} is the loss of the rebar section in mm^2 when the column concrete cracks

$$\Delta A_{so} = A_{so}\left(1 - \left(1 - \frac{\alpha_p}{d_{bo}} x_0 10^{-3}\right)^2\right) \tag{II.19}$$

where A_{so} is the cross-sectional area of the intact steel rebars; α_p is the pitting factor ($\alpha_p = 2$ for uniform corrosion); and x_0 is the corrosion penetration in μm associated with cover depth c in mm (Alonso et al. 1998)

$$x_0 = 7.53 + 9.32(c / d_{bo}) \tag{II.20}$$

The pitting type of corrosion in Eq. II.19 is attributed to the interaction between the chloride ions (Cl^-) and iron hydroxide ($Fe(OH)_2$), which generates autocatalytic reactions[53].

II.3.4. Structural Model

II.3.4.1. Load-Bearing

The nominal capacity of the column ($P_n(t)$) under axial compression is calculated

$$P_n(t)=0.85\left[A_s(t)f_y+0.85\left(f_c^{'}\left(A_g-A_s(t)-A_{iz}\right)+f_c^{*}(t)A_{iz}\right)\right] \tag{II.21}$$

$$A_{iz}=n_b\left(\frac{\left(360^o-2\left(90^0-\theta^o\right)\right)}{360^o}\pi c_r^2-2A_r\right) \tag{II.22}$$

$$A_r=\frac{\pi\left(\phi/2-c_r\right)^2\theta^o}{360^o}-\frac{c_r^2/\tan\theta^o}{2} \tag{II.23}$$

$$\sin\theta^o=\frac{c_r}{\phi/2-c_r} \tag{II.24}$$

where A_g is the gross cross-sectional area of the column; A_{iz} is the area of the influence zone for $f_c^*(t)$ in Eq. II.16 (Figs. II.4(a) and (b)); n_b is the number of the rebars; c_r is the distance from the concrete surface to the rebar center; A_r is the difference between the arc and triangular areas (Fig. II.4(c)); and θ is the angle of the component triangle in degrees. As noted earlier, the equivalent strength of $f_c^*(t)$ in the influence zone (A_{iz}) is activated when the concrete cracks, and the reduced strength reflects the accelerated chloride ingress in the cracked column.

The axial capacity of the column is independently computed by the cellular automata model (Eq. II.25) and verified against Eq. II.21

$$P_n(t)=\left(\sum_{j=1}^{j=n_c}\sum_{i=1}^{i=n_c}\sigma_{c,i,j}(t)+\sum_{j=1}^{j=n_s}\sum_{i=1}^{i=n_s}\sigma_{s,i,j}(t)\right)A_a \tag{II.25}$$

where i and j are the abscissa and ordinate, respectively, in Fig. II.5(a); n_c and n_s are the number of agents for the concrete and steel reinforcement, respectively; A_a is the area of a single agent; and $\sigma_{c,i,j}(t)$ and $\sigma_{s,i,j}(t)$ are the stress in the concrete and steel, respectively

$$\sigma_{c,i,j}(t)=f_{c,i,j}^{'}\left[\frac{2\varepsilon_{c,i,j}(t)}{\varepsilon_{co}}-\left(\frac{\varepsilon_{c,i,j}(t)}{\varepsilon_{co}}\right)^2\right] \tag{II.26}$$

$$\sigma_{s,i,j}(t)=\varepsilon_{s,i,j}(t)E_s\leq\sigma_y \tag{II.27}$$

where $f'_{c,i,j}$ is the compressive strength of the concrete agent $a_{c,i,j}$ at time t (f'_c and $f_c^*(t)$ are used for the core and the impaired area, respectively, Fig. II.4); E_s and σ_y are the elastic modulus and yield strength of the steel (E_s = 200 GPa and σ_y = 414 MPa); $\varepsilon_{c,i,j}(t)$ is the strain of $a_{c,i,j}$; and $\varepsilon_{s,i,j}(t)$ is the strain of the steel agent $a_{s,i,j}$ (Figs. II.5(a) to (c)). The moment capacity of the column ($M_n(t)$) is expressed in a similar manner

$$M_n(t)=\left(\sum_{j=1}^{j=n_c}\sum_{i=1}^{i=n_c}\sigma_{c,i,j}(t)+\sum_{j=1}^{j=n_s}\sum_{i=1}^{i=n_s}\sigma_{s,i,j}(t)\right)A_a\left(\frac{\phi}{2}-j_a\right) \tag{II.28}$$

where j_a is the ordinate of the agent.

II.3.4.2. Interaction Diagram

The capacity of the column can be obtained under compression (P_n) and flexural (M_n) loadings. The pure compression of the section is associated with the uniform strain of ε_{cu} = 0.003, in which ε_{cu} is the maximum usable strain of concrete (ACI 2019). For other general cases, the steel strain at the bottom of the section (ε_s in Fig. II.5(c)) is incremented and, then, the aforementioned $\varepsilon_{i,j}$ strain is determined

$$\varepsilon_{i,j} = \frac{(\varepsilon_s + \varepsilon_{cu})\left(\frac{\varepsilon_{cu}}{\varepsilon_{cu} + \varepsilon_s} d_{br} j_a\right)}{d_{br}} \qquad \text{(II.29)}$$

where d_{br} is the distance from the top of the section to the bottom rebar (Fig. II.5(c)). For the CFRP-confined column, the interaction diagram may be constructed in accordance with the procedure explained in ACI 440.2R-17 (ACI 2017). To accommodate the equivalent compressive strength (Eq. II.16) within the influence zone (A_{iz}), the unconfined concrete strength (f'_c) in Eq. II.1 is replaced by

$$f_i^{'}(t) = \left(f_c^{'}(A_g - A_s(t) - A_{iz}) + f_c^{*}(t)A_{iz}\right)/A_g \qquad \text{(II.30)}$$

where f_i' is the adjusted concrete strength for CFRP-confinement with corrosion damage.

II.4. Implementation

The durability of cast-in-place and ABC columns, predicted by discrete computational cellular automata models, is expounded from material and structural points of view. Emphasis is placed on the diffusivity of chlorides, consequences of corrosion, and the efficaciousness of CFRP-strengthening.

II.4.1. Chloride Migration

II.4.1.1. Diffusion

The coefficients of chloride diffusion are provided in Figs. II.6(a) and (b) for the cast-in-place and ABC columns, respectively. The exponentially diminishing coefficients illustrate that the concrete pores became partially clogged by surplus chlorides over time; in other words, the permeated chlorides reduced the effective porosity of the cement binder (Koleva et al. 2008). As the compressive strength of the concrete was increased from 30 MPa to 45 MPa, the flux of the chlorides noticeably dropped (Fig. II.6(a)). This observation aligns with the fact that greater hydration in concrete leads to a strength gain and decreases the size of micro-pores; consequently, the transport of chloride ions in the electrolytes is retarded (Purnell 2007; Shi et al. 2019). Compared with the cast-in-place column, the diffusion coefficient of the ABC column was lower (Fig. II.6(b)) and the submerged condition showed a consistently higher coefficient than other environments, owing to the increased conductivity of the pore solution (Zhang et al. 2018). Likewise, the rate of the diffusion coefficient rapidly developed under the submerged condition for the cast-in-place column (Fig. II.6(c)), whereas marginal differences were noted among the three environments after 30 years (Fig. II.6(c), inset). Shown in Fig. II.6(d) is a comparison between the diffusion coefficient rates of the cast-in-place and ABC columns. Irrespective of concrete strength (f'_c = 30 MPa and 45 MPa), the ABC column outperformed and its peak rates were 37% of those of the cast-in-place column, on average.

II.4.1.2. Concentration

The chloride concentrations of the cast-in-place column at the level of steel surface are plotted in Figs. II.7(a) and (b), dependent upon concrete strength and exposure condition, respectively. The ingress of chlorides in the column with f'_c = 30 MPa was 1.9 times relative to the case with f'_c = 45 MPa at 100 years (Fig. II.7(a)). The high water-to-cement ratio of the low strength concrete (Table II.1) allowed more chlorides on account of the increased permeability (Espinoza-Hijazin and Lopez 2011). In regard to the environmental exposure (Fig. II.7(b)), the concentration was prominent under the splash condition because the wet-dry cycles expedited the sorptivity of the concrete (Stanish et al. 1997). As concrete resistance to chlorides declines when saturated (Basheer et al. 2002), the asymptotic concentration curve under the submerged condition was graphed above the curve under the atmospheric condition. It is worth noting that, even if both were subjected to water, the mechanisms of chloride progression under the splash and submerged conditions differed: the former was based on absorption and capillary suction, while the latter was related to pure diffusion caused by a concentration gradient in the electrolyte across the column (Andrade 1993).

Figure II.7(c) exhibits the elevation of chloride concentrations in the cast-in-place and ABC columns under the submerged condition. The response slope of the cast-in-place column was steep up to 12 years, followed by a transition to the gradually rising concentrations. Except for the distinguishable development trend between 0 and 30 years, the slopes of these column categories were virtually identical, meaning that the superior durability of the ABC column was due to the betterment of its performance during the relatively early ages. For this reason, the ABC column allowed less chlorides inside the concrete (Fig. II.7(d)). A comprehensive summary of the chloride concentrations at a depth of 100 mm, the average cover of the columns, is charted in Figs. II.7(e) and (f). The use of ABC was beneficial for all occasions, especially under the splash condition.

II.4.2. Effects of Corrosion

II.4.2.1. Corrosion Current Density

The ascending pattern of the corrosion current density was a function of the concrete strength (Fig. II.8(a)), which is concerned with the connectivity of the micro-pores that dominates the transport of chloride ions (Koleva et al. 2008). The difference in the initial diffusion coefficient ($D(0)$ in Table II. 2) was responsible for the grouping of the densities above and below the concrete strength of f'_c = 40 MPa. Figure II.8(b) reaffirms that the alternate cycles of saturation and desiccation raised the conductivity of the micro-pores with the dissolved chloride ions (Casoli et al. 2020), thereby lessening the resistivity of the column concrete under the splash condition (that is, the increased corrosion rate). Such a prediction, however, does not necessarily signify invariant local conductivity since the activation energy of the concrete oscillated as per the degree of saturation (Wang et al. 2016). The evolution tendency of the current density under the submerged condition in Fig. II.8(b) clarifies the importance of continued oxidation for the electrochemical process of corrosion: the plateau-like response was attributable to the limited supply of oxygen in the pores that partially filled with chlorides, which slowed down cathodic reactions (Hornbostel et al. 2013). Shown in Fig. II.8(c) are the corrosion current densities normalized by time. The growth rate of the density for the cast-in-place column was rapider than the rate for the ABC column, whereas their dissimilarity disappeared after 40 years. It is thus stated that the high current density of the cast-in-place column (Fig. II.8(d)) was the result of the accelerated rate before the 40-year alteration time.

II.4.2.2. Detrimental Consequences

Figure II.9(a) demonstrates the corrosion initiation year of the cast-in-place column. Under the splash and submerged conditions that were linked with direct contact to water, the initiation time was 11 years, on average. Contrarily, the initiation time under the atmospheric condition was longer than 54 years and the case with a concrete strength higher than 40 MPa would not corrode within the 75-year design life of AASHTO LRFD BDS (AASHTO 2020). The corrosion initiation of the ABC column took substantially longer, up to 4.3 times that of the cast-in-place column (Fig. II.9(b)). Once the columns corroded, the diameter of the reinforcing bars began to dwindle (Fig. II.9(c)) and the use of the ABC technique remarkably inhibited a reduction magnitude (Fig. II.9(d)). The strength decrease of the equivalent cover concrete for the cast-in-place column was noticed at 16.5 years and 15.4 years under the splash and submerged conditions, respectively (Fig. II.9(e)), which were incomparable with the case under the atmospheric exposure (> 62 years). As shown in Fig. II.9(f), the ratio of the cover-strength reduction time between the ABC and cast-in-place columns was over 1.56 (no reduction occurred for the ABC column with a concrete strength greater than 35 MPa).

II.4.3. Structural Aspect

II.4.3.1. Axial Capacity

The reduced capacity of the cast-in-place column under the splash condition inducing corrosion is provided in Fig. II.10(a). The ratio of the capacities between the damaged and undamaged states diminished with time. It should be noted that the proximity of the responses with f'_c = 35 MPa and 40 MPa resulted from the same cover depth of 100 mm, Table II.2. The contribution of each constituent to the capacity drop is visible in Figs. II.10(b) and (c). The capacity variation caused by the equivalent compressive strength (Eq. II.16) was the primary factor (Fig. II.10(b)), while the influence of the steel corrosion was marginal (Fig. II.10(c)). In particular, the dependency of the concrete strength pertaining to the chloride flux was significant on the capacity decrease of the column exposed to water (the splash and submerged conditions, Fig. II.10(d)). The benefit of the ABC column was pronounced for a low strength concrete; for instance, the capacity-drop ratios between the ABC and cast-in-place columns under the submerged condition were 0.88 and 0.67 for f'_c = 30 MPa and 45 MPa, respectively (Fig. II.10(e)).

II.4.3.2. Effectiveness of CFRP-Confinement

Complying with the provisions of ACI 440.2R-17 (ACI 2017) (Eqs. II.1 and II.2), the number of CFRP layers was calculated and then rounded for practical application (Fig. II.11(a)). The more durable ABC column necessitated less layers than the cast-in-place column, and the propensity was preserved without regard to the strength of the unconfined concrete (f'_c). The constitutive relationship of the confined concrete (Fig. II.11(b)) was bilinear until the maximum useable strains of CFRP were reached (all values did not exceed the strain limit of 0.01 specified in ACI 440.2R-17 (ACI 2017)). Although the increased f'_c from 30 MPa to 45 MPa raised the confined strength (f'_{cc}), the usable strain was shortened from ε_{ccu} = 0.0065 to 0.0044. An average toughness ratio of 1.97 was noted between the confined and unconfined cases (toughness is defined as the area under a stress-strain curve up to failure); scilicet, CFRP-confinement improved the energy dissipation of the column concrete. Figures II.11(c) and (d) show the time-dependent capacity ratio of the cast-in-place and ABC columns, respectively. In line with the strengthening philosophy established earlier, the columns were strengthened when a 10% reduction was noticed in the capacity and the enhanced ratios were maintained above unity for the rest of service life to 100 years (confined capacity ≥ intact capacity). The temporal span of the adjusted capacity ratio for the cast-in-place column (27.4 years to 100 years) was 46.4% longer than the span for the ABC column (50.4 years to 100 years); on the contrary, the efficacy of strengthening was indistinguishable, which corroborates the fact that CFRP-based rehabilitation is a recommendable technique for both column types.

II.4.3.3. Load-Moment Interaction

The interaction diagram of the axial load (P_n) and bending moment (M_n) for the cast-in-place column at 100 years is given in Fig. II.12(a). The size of the interaction envelope conspicuously decreased under the splash condition. With CFRP-confinement, the envelope was enlarged over the control curve, indicating the fully recovered performance of the abated column. The abruptly dropping moment at the balance point of the confined column (P_b and M_b) was ascribed to the restriction of ACI 440.2R-17 (ACI 2017): strength enhancement is only allowed in the compression-controlled region. As the core strength (f'_c) was increased (Fig. II.12(b)), the resistance level of the upgraded column became elevated against the combined axial compression and bending. The ABC column exhibited structural efficiency with less CFRP layers (Fig. II.12(c)). The transition moment from compression- to tension-controlled failure modes went up in proportion to the core strength (Fig. II.12(d)) and, albeit inappreciable, the ABC column outperformed the cast-in-place column.

II.5. Summary and Conclusions

This report has investigated the detrimental effects of chloride migration in cast-in-place and ABC column models exposed to atmospheric, splash, and submerged environments. Employing a novel simulation approach called cellular automata, chloride diffusivity and various levels of corrosion were computed during a service period of 100 years. The degraded columns were strengthened with CFRP sheets in conformity with ACI 440.2R-17 (ACI 2017) and their load-carrying capacity was examined. Attention was directed toward full-range interactions between axial and flexural loadings. The study substantiated that CFRP-confinement was a favorable technique for both column types. The following are concluded:

- Because of the concrete pores partially filled by surplus chlorides as documented in the literature, the diffusion coefficient of the columns exponentially decreased with time. The microstructural characteristics of the concrete relating to the compressive strength also dominated the ingress of chlorides. The chloride diffusion of the ABC column was slower than that of the cast-in-place column; however, their distinction in the diffusion rate disappeared after 30 years.
- The chloride concentration of the columns under the splash condition was noticeable owing to the expedited sorptivity of the concrete subjected to wet-dry cycles, which was properly documented by others. The development of chloride concentrations in the cast-in-place column was faster than the case of the ABC column, which led to the superior durability of the latter particularly under the splash exposure.
- The corrosion current density of the columns steadily rose up to 100 years, while the growth pattern was a function of the concrete strength related to the connectivity of micro-pores. Compared with the ABC column, the cast-in-place column revealed a rapid increase rate in the current density until 40 years, beyond which both cases showed similar responses.
- When the cast-in-place column was exposed to water (splash and submerged), the average corrosion initiation time was 11 years. By contrast, the ABC column required up to a 4.3 times longer period and effectively impeded a loss in the cross-sectional area of the reinforcement. The

reduction of the equivalent strength due to corrosion-induced cracking and spalling was not noticed for the ABC column with a concrete strength of 35 MPa and greater.

- With the presence of corrosion damage, the axial capacity of the cast-in-place and ABC columns decreased by 28% and 23% under the splash condition at 100 years, respectively. The primary factor for such an observation was the impaired concrete in the corrosion influence zone, whereas the direct contribution of the deteriorated reinforcement was less than 5%.
- The CFRP-strengthening raised the toughness of the existing concrete by almost two times; accordingly, the confined columns were able to carry more moments without flexural failure. Notwithstanding the reduced number of CFRP layers, the ABC column's performance was comparable to that of the cast-in-place column under synergistic distress from axial compression and bending.

References

AASHTO. 2020. AASHTO LRFD bridge design specifications (9th edition), American Association of State Highway Transportation Officials, Washington, D.C

ACI. 2002. Standard practice for selecting proportions for normal, heavyweight, and mass concrete (ACI 211.1-91: reapproved 2002), American Concrete Institute, Farmington Hills, MI.

ACI. 2017. Guide for the design and construction of externally bonded FRP systems for strengthening concrete structures (ACI 440.2R-17), American Concrete Institute, Farmington Hills, MI.

ACI. 2019. Building code requirements for structural concrete and commentary (ACI 318-19), American Concrete Institute, Farmington Hills, MI.

Ahmad, A. and Kumar, A. 2013. Chloride ion migration/diffusion through concrete and test methods, International Journal of Advanced Scientific and Technical Research, 3(6), 151-180.

Alizadeh, R., Ghods, P., Chini, M., Hoseini, M., Ghalibafian, M., and Shekarchi, M. 2008. Effect of curing conditions on the service life design of RC structures in the Persian Gulf region, Journal of Materials in Civil Engineering, 20(1), 2-8.

Alonso, C., Andrade, C., Rodriguez, J and Diez, J.M. 1998. Factors controlling cracking of concrete affected by reinforcement corrosion, Material and Structures, 31, 435-441

Amran, Y.H.M., Alyousef, R., Alabduljabbar, H., Alaskar, A., and Alrshoudi, F. 2020. Properties and water penetration of structural concrete wrapped with CFRP, Results in Engineering, 5, 100094.

Andrade, C. 1993. Calculation of chloride diffusion coefficients in concrete from ionic migration measurements, Cement and Concrete Research, 23, 724-742.

ASTM. 2004. Standard test method for measurement of rate of absorption of water by hydraulic-cement concretes (ASTM C1585-04), ASTM International, West Conshohocken, PA.

Baetens, J.M. and Kutrib, M. 2018. Cellular automata and discrete complex systems, Springer, Cham, Switzerland

Basheer, P.A.M., Gilleece, P.R.V., Long, A.E., and McCarter, W.J. 2002. Monitoring electrical resistance of concretes containing alternative cementitious materials to assess their resistance to chloride penetration, Cement and Concrete Composites, 24, 437-449.

Bousias, S.N., Biskinis, D., Fardis, M.N., and Spathis, A.-L. 2007. Strength, stiffness, and cyclic deformation capacity of concrete jacketed members, ACI Structural Journal, 104(5), 521-531.

Cao, J., Wang, Y., Li, K., and Ma, Y. 2012. Modeling the diffusion of chloride ion in concrete using cellular automaton, Journal of Materials in Civil Engineering, 24 (6), 783-788.

Cheewaket, T., Jaturapitakkul, C and Chalee, W. 2010. Long term performance of chloride binding capacity in fly ash concrete in a marine environment, Construction and Building Materials, 24(8), 1352-1357.

Chen, E., Tang, S., and Leung, C.K.Y. 2019. Corrosion-induced cracking in reinforced concrete due to chloride contamination and ingress, ACI Materials Journal, 116(5), 99-111.

Christodoulou, C., Goodier, C., Austin, S., Webb, J., and Glass, G.K. 2013. Diagnosing the cause of incipient anodes in repaired reinforced concrete structures, Corrosion Science, 69, 123-129.

Coronelli, D., and Gambarova, P. 2004. Structural assessment of corroded reinforced concrete beams: modeling guidelines, Journal of Structural Engineering, 130(8),1214-1224.

Cosoli, G., Mobili, A., Tittarelli, F., Revel, G.M., and Chiariotti, P. 2020. Electrical resistivity and electrical impedance measurement in mortar and concrete elements: a systematic review, Applied Sciences, 10, 9152.

Cuzzilla, R., Di Ludovico, M., Prota, A., and Manfredi, G. 2011. Seismic rehabilitation of RC bridges by using FRP and SRP: case study of a bridge in the south of Italy, ACI-SP 277 (Recent Advances in Maintenance and Repair of Concrete Bridges), 1-20.

Debaiky, A.S., Green, M.F., and Hope, B.B. 2002. Carbon fiber-reinforced polymer wraps for corrosion control and rehabilitation of reinforced concrete columns, ACI Materials Journal, 99(2), 129-137.

ElMaaddawy, T., Chahrour, A., and Soudki, K. 2006. Effect of fiber-reinforced polymer wraps on corrosion activity and concrete cracking in chloride-contaminated concrete cylinders, Journal of Composites for Construction, 10(2), 139-147.

Elsener, B. and Angst, U. 2016. Corrosion inhibitors for reinforced concrete, Science and Technology of Concrete Admixtures, 321-339.

Espinoza-Hijazin, G. and Lopez, M. 2011. Extending internal curing to concrete mixtures with W/C higher than 0.42, Construction and Building Materials, 25, 1236-1242.

Eyu, G.D., Will, G., Dekkers, W., and MacLeod, J. 2017. Effect of dissolved oxygen and immersion time on the corrosion behaviour of mild steel in bicarbonate/chloride solution, Materials, 9(9), 748.

Frederiksen, J.M., Mejlbro, L., and Poulsen, E. 2000. The HETEK model of chloride ingress into concrete made simpler by approximations, International RILEM Workshop on Testing and Modelling the Chloride Ingress into Concrete, 317-336.

Gao, J., Yu, Z., Song, L., Wang, T., and Wei, S. 2013. Durability of concrete exposed to sulfate attack under flexural loading and drying-wetting cycles, Construction and Building Materials, 39, 33-38.

Grantham, M., Mechtcherine, V., and Schneck, U. 2012. Concrete solutions, CRC Press, London, UK.

Hamilton, C.H., Pardoen, G.C., Navalpakkam, S., and Kanzanjy, R.P. 2004. Reinforced concrete bridge column performance enhancement through shotcrete jacketing, ACI Structural Journal, 101(3), 332-340.

Hoekstra, A.G., Kroc, J., and Sloot, P.M.A. 2010. Simulating complex systems by cellular automata, Springer, Heidelberg, Germany.

Hornbostel, K., Larsen, C.K., and Geiker, M.R. 2013. Relationship between concrete resistivity and corrosion rate - A literature review, Cement and Concrete Composites, 39, 60-72.

Hussain, R.R., Al-Negheimish, A., Alhozaimy, A., and Singh, D.D.N. 2020. Corrosion characteristics of vanadium micro-alloyed steel reinforcement bars exposed in concrete environments and industrially polluted atmosphere, Cement and Concrete Composites, 113, 103728.

Karimipour, A. and Edalati, M. 2021. Retrofitting of the corroded reinforced concrete columns with CFRP and GFRP fabrics under different corrosion levels, Engineering Structures, 228, 111523.

Khan, M.A. 2014. Accelerated bridge construction: best practices and techniques, Butterworth-Heinemann, Oxford, UK.

Koch, G., Varney, J., Thompson, N., Moghissi, O., Gould, M., and Payer, J. 2016. International measures of prevention, application and economics of corrosion technology, NACE International, Houston, TX.

Koleva, D.A., Copuroglu, O., van Breugel, K., Ye, G., de Wit, J.H.W. 2008. Electrical resistivity and microstructural properties of concrete materials in conditions of current flow, Cement and Concrete Composites, 30, 731-744.

Liu, T. and Weyers, R.W. 1998. Modeling the dynamic corrosion process in chloride contaminated concrete structures, Cement and Concrete Research, 28(3), 365-379.

Liu, R. and Palermo, A. 2020. Ten years of experiments on bridges using resilient damage-resistant systems and accelerated construction techniques, Structural Engineering International, 30(2), 224-231.

NACE. 2007. Corrosion control of submerged areas of permanently installed steel offshore structures associated with petroleum production (SP0176-2007-SG), National Association of Corrosion Engineers, Houston, TX.

Nossoni, G. 2015. Modeling the corrosion rate of steel reinforcement in FRP-wrapped concrete, Journal of Composites for Construction, 20(3), 04015068.

Podrouzek, J. and Teply, B. 2008. Modelling of chloride transport in concrete by cellular automata, Engineering Mechanics, 15(3), 213-222.

Poulsen, E. and Mejlbro, L. 2006. Diffusion of chloride in concrete: theory and application. Taylor and Francis, New York, NY.

Purnell, P. 2007. Degradation of fibre-reinforced cement composites, Durability of Concrete and Cement Composites, Elsevier, 316-363.

Ramirez, J.L. 1996. Ten concrete column repair methods, Construction and Building Materials, 10(3), 1996.

Roy, S.K., Chye, L.K., and Northwood, D.O. 1993. Chloride ingress in concrete as measured by field exposure tests in the atmospheric, tidal and submerged zones of a tropical marine environment, Cement and Concrete Research, 23(6), 1289-1306.

Shi, Y., Chen, X., Li, J., Li, X., and Peng, Z. 2019. Micro–macro properties of plastic concrete anti-seepage wall materials mixed with low-liquid limit clay, Advances in Mechanical Engineering, 11(5), 1-9.

Stanish, K.D., Hoonton, R.D., and Thomas, M.D.A. 1997. Testing the chloride penetration resistance of concrete: a literature review, Report No. DTFH61-97-R-00022, Federal Highway Administration, Washington, D.C.

Song, H.W., Chang, H.L., and Ann, K.Y. 2008. Factors influencing chloride transport in concrete structures exposed to marine environments, Cement and Concrete Composites, 30(2): 113-121.

Suh, K., Mullins, G., Sen, R., and Winters, D. 2007. Effectiveness of fiber-reinforced polymer in reducing corrosion in marine environment, ACI Structural Journal, 104 (1), 76-83.

Titi, A, and Biondini, F. 2016. On the accuracy of diffusion models for life-cycle assessment of concrete structures, Structure and Infrastructure Engineering, 12(9), 1202-1215.

Thoft-Christensen, P., Jensen, F.M., Middleton, C.R., and Blackmore, A. 1996. Assessment of the reliability of concrete slab bridges, 7th IFIP WG 7.5 Working Conference, Boulder, CO, 1-8.

Val, D.M. and Melchers, R.E. 1997. Reliability of deteriorating RC slab bridges, Journal of Structural Engineering, 123(12), 1638-1644.

Vecchio, F.J., and Collins, M.P. 1986. Modified compression-field theory for reinforced concrete elements subjected to shear, Journal of the American Concrete Institute, 83(2), 219-231.

Vidal, T., Castel, A., and François, R., 2004. Analyzing crack width to predict corrosion in reinforced concrete, Cement and Concrete Research, 34(1), 165-174.

Wang, Y., Gong, F., Zhang, D., and Ueda, T. 2016. Estimation of ice content in mortar based on electrical measurements under freeze-thaw cycle, Journal of Advanced Concrete Technology, 14, 35-46.

Wang, Y., An, M., Yu, Z., Han, B., and Ji, W. 2018. Experimental and cellular-automata-based analysis of chloride ion diffusion in reactive powder concrete subjected to freeze-thaw cycling, Construction and Building Materials, 172, 760-769.

Wolfram, S. 1984. Cellular automata as models of complexity, Nature, 311(5985), 419-424.

Wolnik, B. and Baets, B.D. 2020. Ternary reversible number-conserving cellular automata are trivial, Information Sciences, 513, 180-189.

Wu, L., Wang, Y., Wang, Y., Ju, X., and Li, Q. 2020. Modelling of two-dimensional chloride diffusion concentrations considering the heterogeneity of concrete materials, Construction and Building Materials, 243, 118213.

Yin, G., and Pan., L. 2020. The effect of shape on chloride penetration of circular reinforcement concrete columns and its durability design, Applied Sciences 10(2): 459.

Yoon, S., Wang, K., Weiss, W.J., and Shah, S.P. 2000. Interaction between loading, corrosion, and serviceability of reinforced concrete, ACI Materials Journal, 97(6), 637-644.

Zhang, Q. and Alam, M.S. 2020. State-of-the-art review of seismic-resistant precast bridge columns, Journal of Bridge Engineering, 25(10), 03120001.

Zhang, Y., Zhang, M., and Ye, G. 2018. Influence of moisture condition on chloride diffusion in partially saturated ordinary Portland cement mortar, Materials and Structures, 51:36

Table II.1. Details of concrete mixture

Component	Compressive strength (MPa)			
	30	35	40	45
wc	0.54	0.47	0.42	0.37
Water (kg/m³)	193	193	193	193
Cement (kg/m³)	358	406	455	524
Coarse aggregate (kg/m³)	1,144	1,144	1,144	1,144
Fine aggregate (kg/m³)	679	639	597	539

wc = water-to-cement ratio

Table II.2. Modeling parameters

Concrete strength, f'_c (MPa)	Construction method	Service environments	Concrete cover, c (mm)	Diffusion coefficient, $D(0)$ ($\times 10^{-12}\mathrm{m}^2/\mathrm{s}$)	Age parameter, η	Surface chloride, C_0 (% wt. of cement)	Corrosion initiation year, t_i (years)
30	CIP	Atmospheric	125	4.29	0.19	1.33	54.1
		Splash	125	6.43	0.019	$1.65t^{0.484}$	8.9
		Submerged	125	10.72	0.114	3.31	9.6
	ABC	Atmospheric	125	1.00	0.19	1.33	232.8
		Splash	125	2.30	0.019	$1.65t^{0.484}$	25.8
		Submerged	125	3.97	0.114	3.31	25.9
35	CIP	Atmospheric	100	3.15	0.295	1.17	55.6
		Splash	100	4.72	0.03	$1.37t^{0.484}$	8.8
		Submerged	100	7.87	0.177	2.93	9.1
	ABC	Atmospheric	100	0.73	0.295	1.17	238.9
		Splash	100	1.69	0.03	$1.37t^{0.484}$	25.5
		Submerged	100	2.91	0.177	2.93	24.5
40	CIP	Atmospheric	100	2.41	0.37	1.05	85.7
		Splash	100	3.62	0.037	$1.17t^{0.484}$	11.9
		Submerged	100	6.03	0.222	2.63	12.8
	ABC	Atmospheric	100	0.56	0.37	1.05	368.4
		Splash	100	1.29	0.037	$1.17t^{0.484}$	34.3
		Submerged	100	2.23	0.222	2.63	34.7
45	CIP	Atmospheric	85	1.75	0.445	0.92	108.3
		Splash	85	2.63	0.045	$0.97t^{0.484}$	12.7
		Submerged	85	4.38	0.267	2.29	14.2
	ABC	Atmospheric	85	0.41	0.445	0.92	465.7
		Splash	85	0.94	0.045	$0.97t^{0.484}$	36.7
		Submerged	85	1.62	0.267	2.29	38.3

CIP = cast-in-place; ABC = accelerated bridge construction

Table II.3. Properties used for model validation

Reference	Surface chloride	Diffusion coefficient (m^2/s)
Cao et al.[35]	0.5% wt. of concrete	3.22×10^{-12}
Titi and Biondini[36]	3% wt. of concrete	1×10^{-11}
Wang et al.[37]	$1.95\times(t/360)^{1.28715}$ mg/g*	$2.588\times(360/t)^{-0.9574}\times10^{-13}$
Yin and Pan[38]	2% wt. of binder	$1.38\times(28/t)^{-0.53}\times10^{-13}$

*: mass of chloride ions per mass of cementitious binder

t = time in days

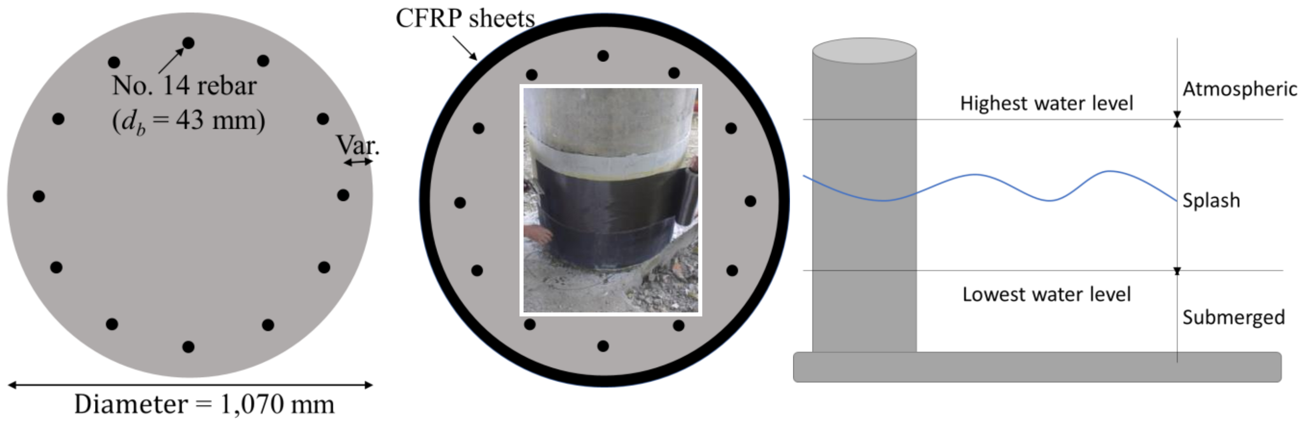

(a) (b)

Fig. II.1. Benchmark column: (a) dimension and strengthening scheme (picture (Cuzzilla et al. 2011) used with permission, American Concrete Institute); (b) service environments

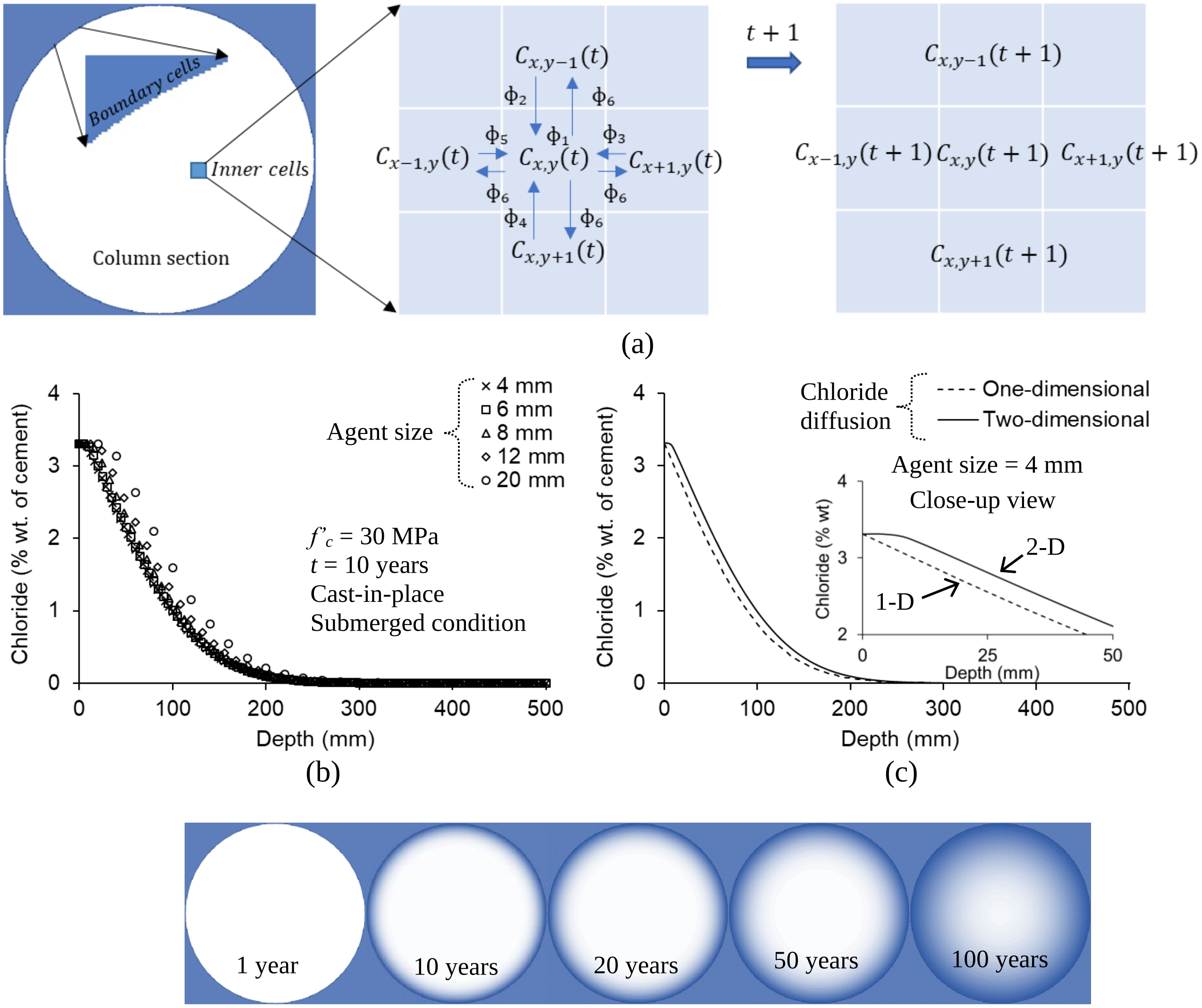

(a)

(b)

(c)

(d)

Fig. II.2. Two-dimensional cellular automata for benchmark column: (a) configuration of von Neumann's square lattice; (b) sensitivity analysis; (c) proposed versus conventional approaches; (d) simulated chloride migration in cast-in-place column with concrete strength = 30 MPa under submerged condition

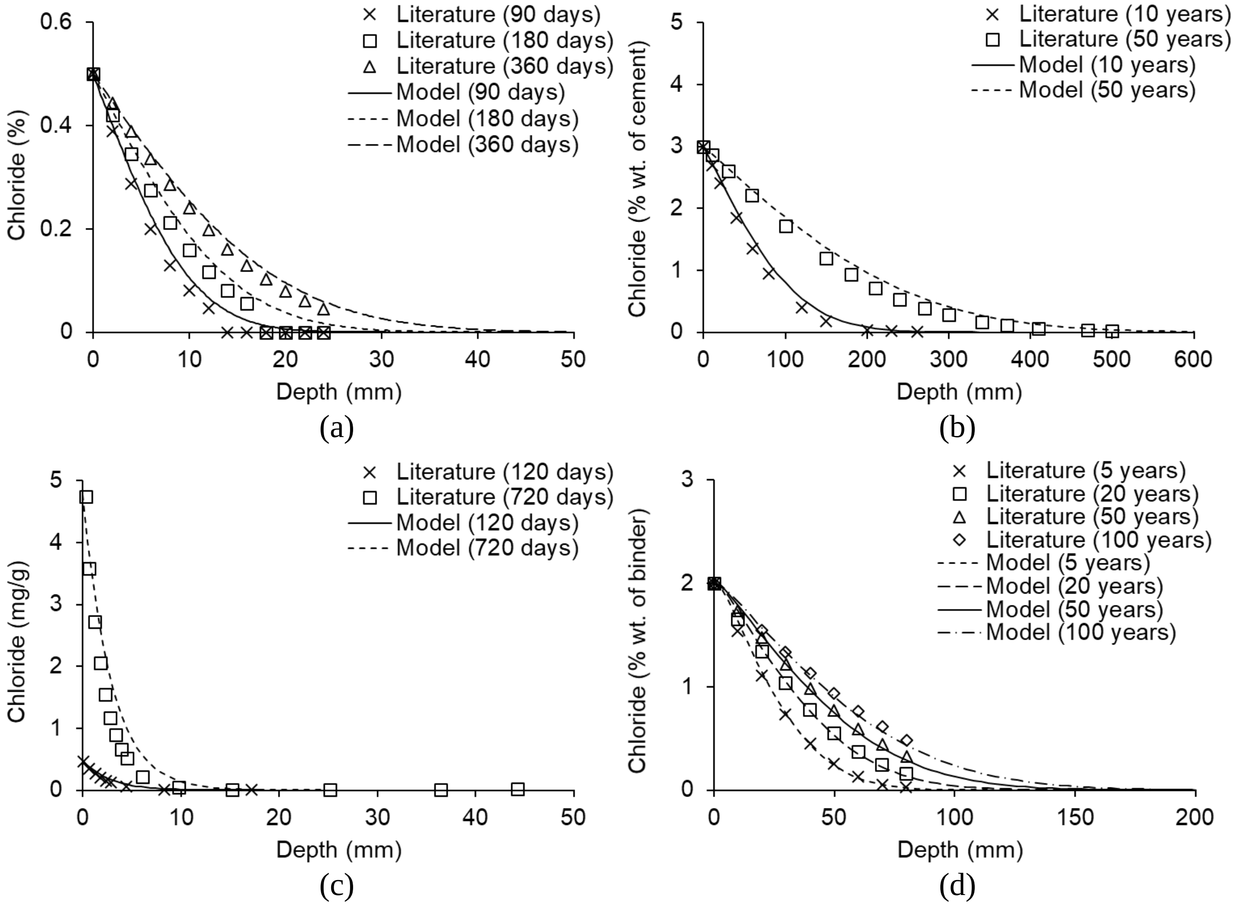

(a) (b)

(c) (d)

Fig. II.3. Validation of modeling approach: (a) Cao et al. (2012); Titi and Biondini (2016); (c) Wang et al. (2018); (d) Yin and Pan (2020)

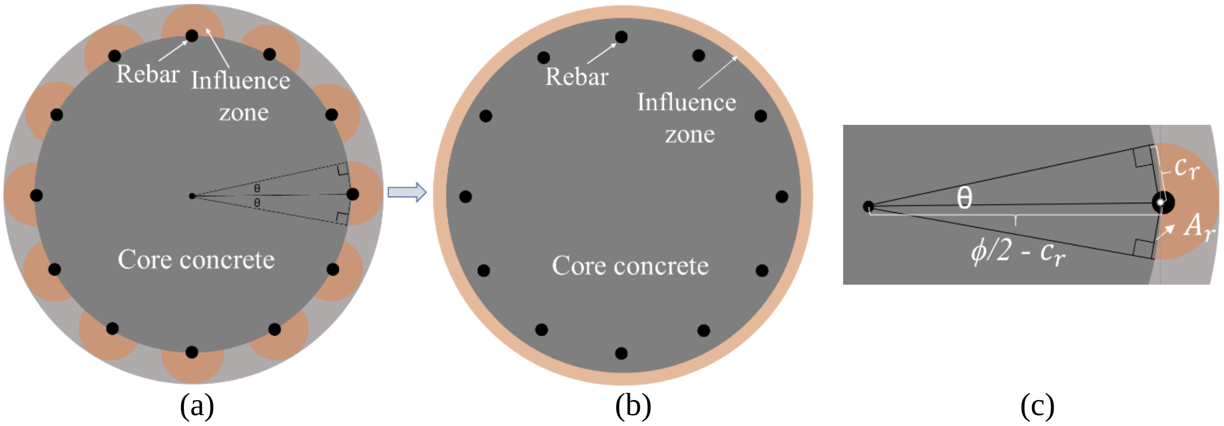

Fig. II.4. Cover-strength reduction: (a) spalling and cracking zones; (b) equivalent area; (c) geometric details

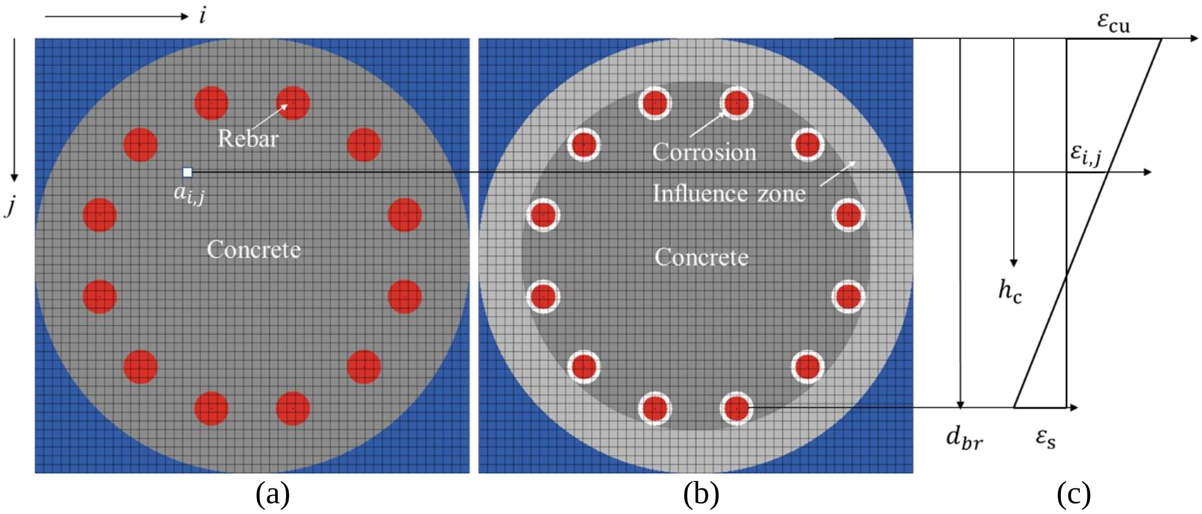

Fig. II.5. Sectional model: (a) intact column; (b) corrosion-damaged column; (c) strain profile

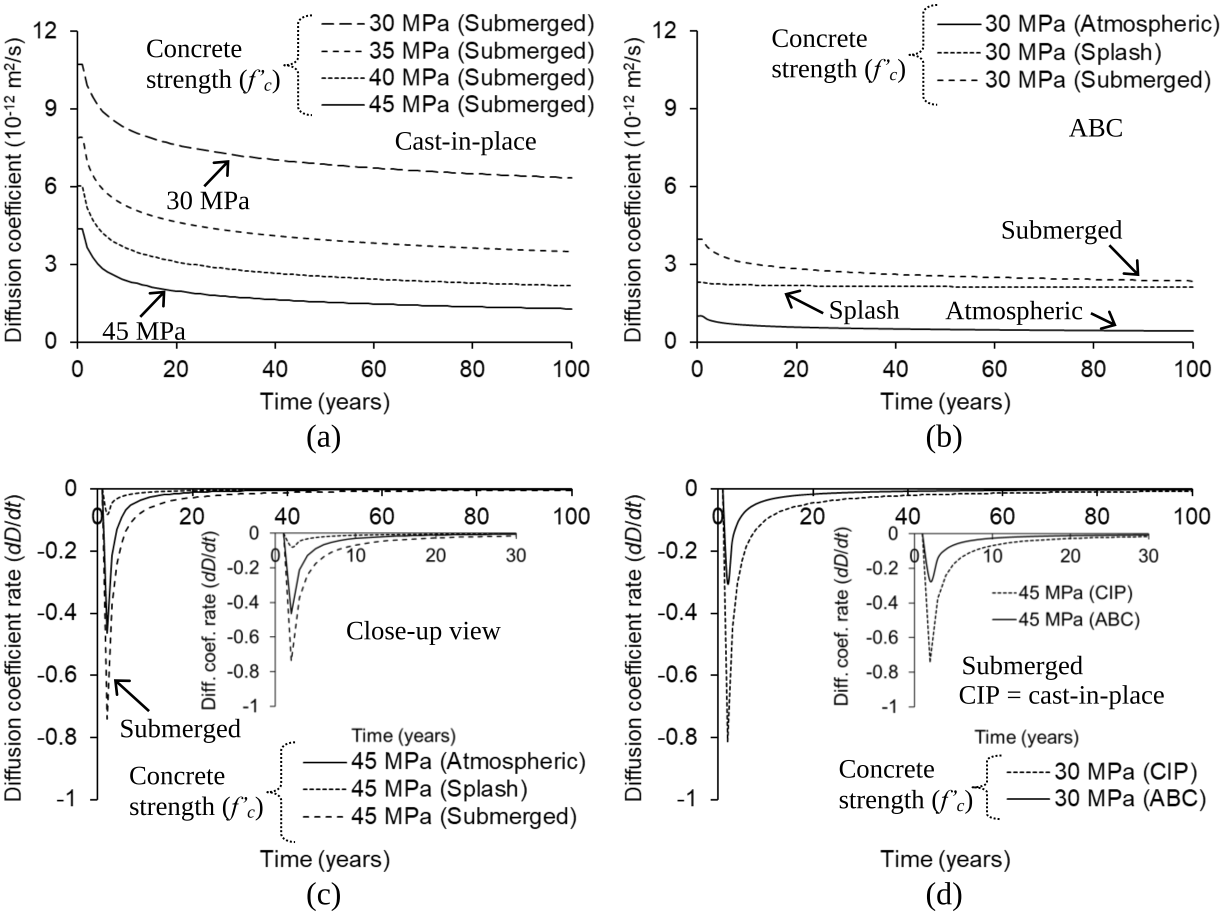

Fig. II.6. Diffusion coefficient: (a) cast-in-place column with concrete strength; (b) ABC column with service environment; (c) rate in cast-in-place column with service environment; (d) comparison of rates between cast-in-place and ABC columns under submerged condition

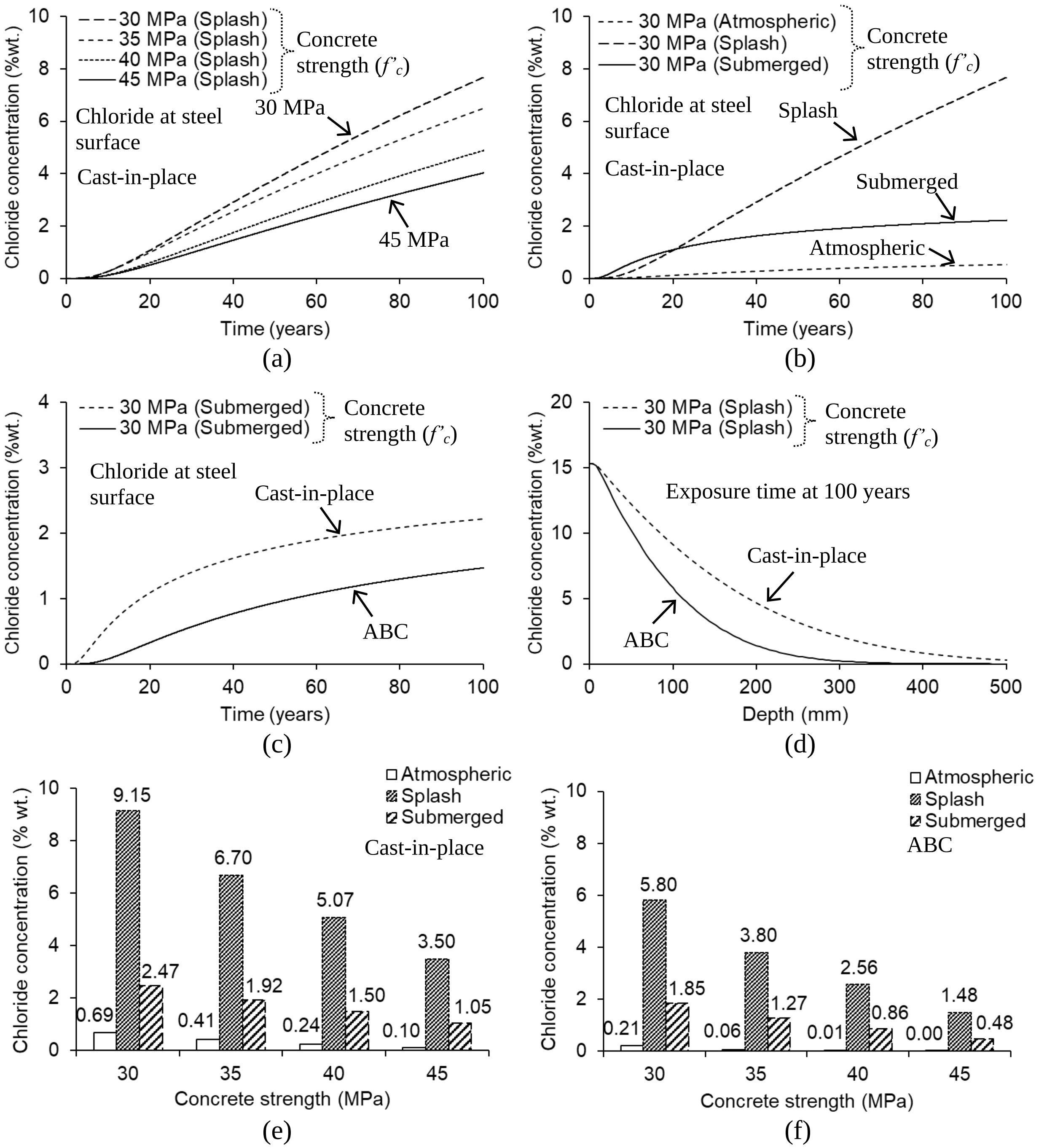

Fig. II.7. Chloride concentration: (a) cast-in-place column with concrete strength; (b) cast-in-place column under variable environments; (c) cast-in-place vs. ABC columns with time; (d) cast-in-place vs. ABC columns across concrete; (e) cast-in-place column at 100 mm from surface; (f) ABC column at 100 mm from surface

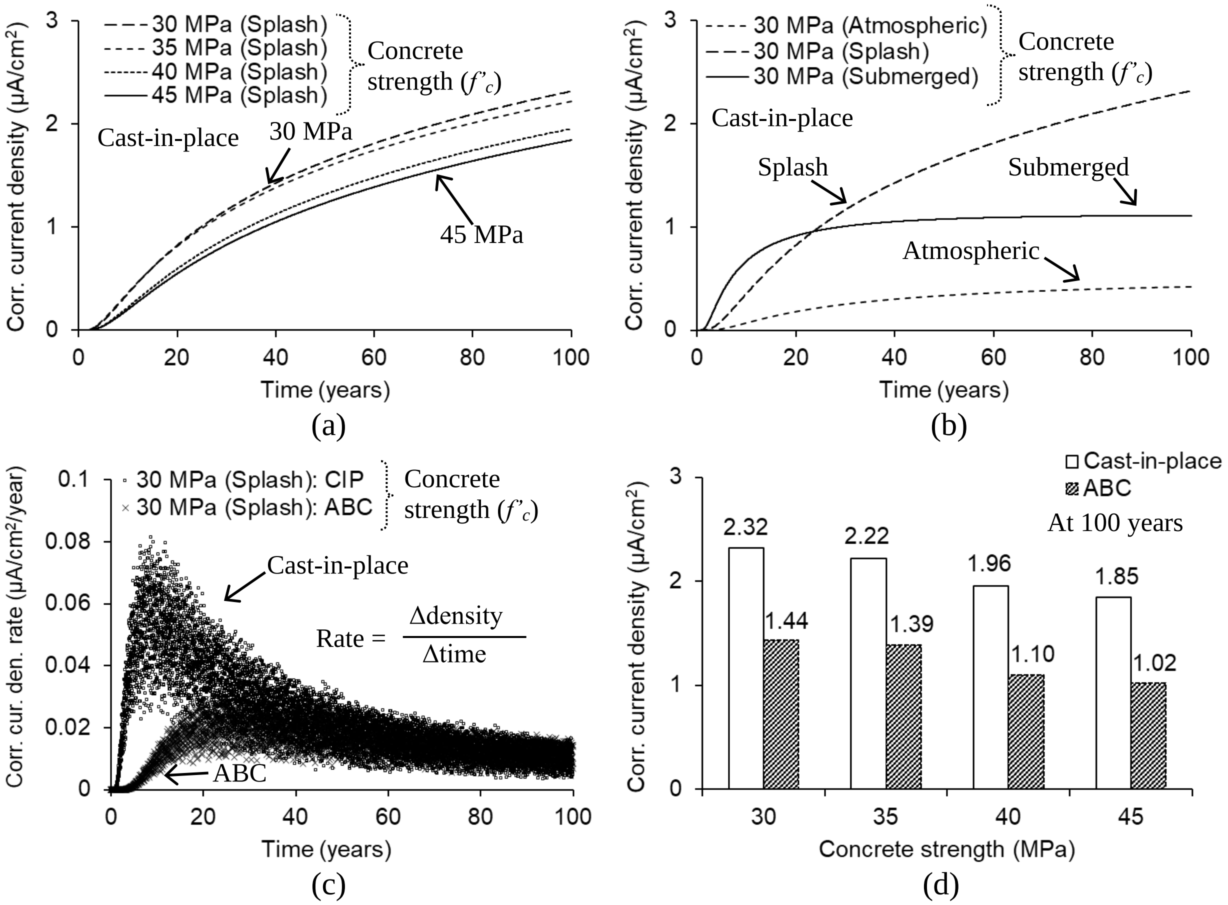

Fig. II.8. Corrosion current density at surface level of reinforcement: (a) cast-in-place column with concrete strength; (b) cast-in-place column under variable environments; (c) cast-in-place vs. ABC columns with time; (d) comparison at 100 years

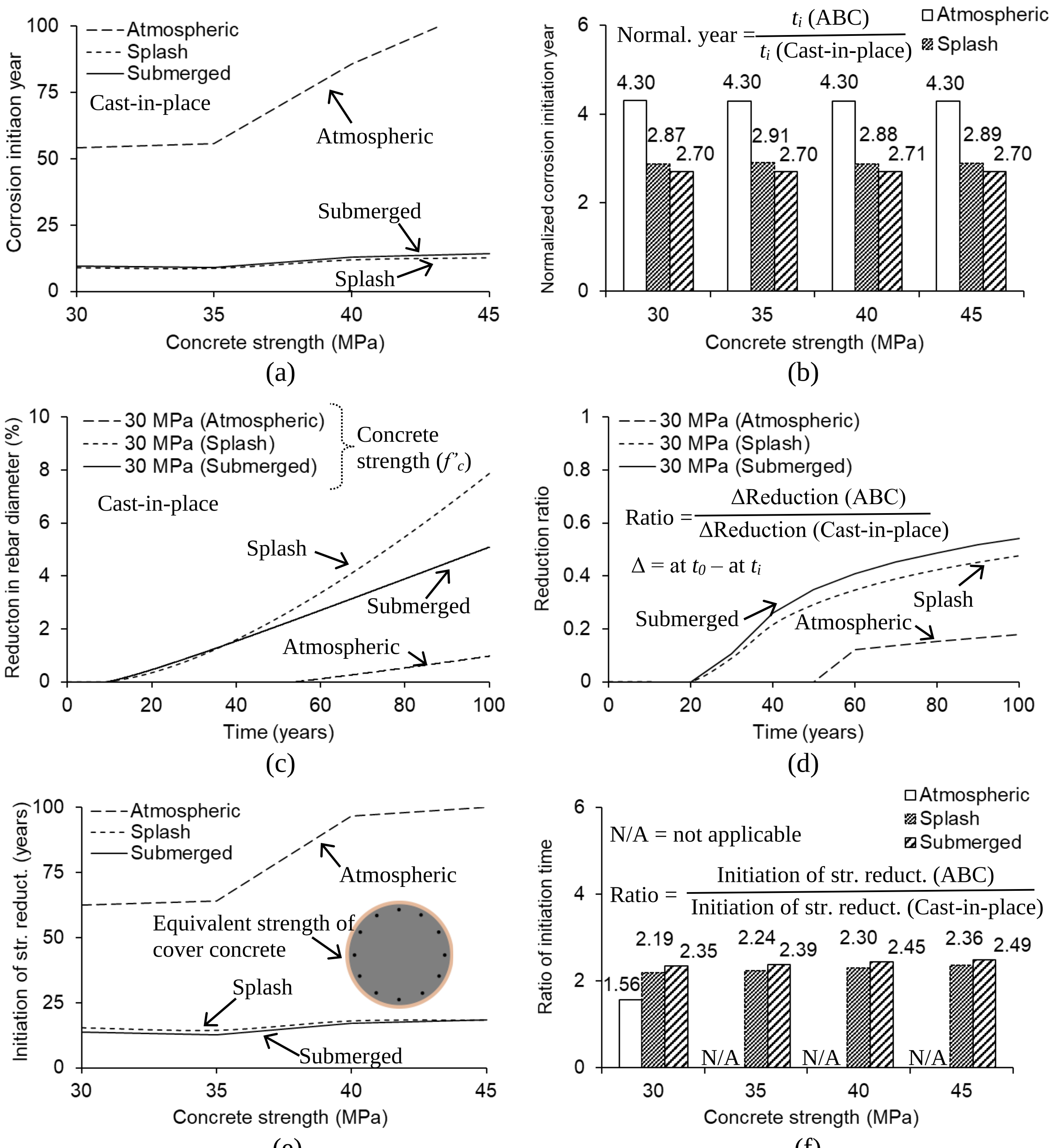

(a)

(b)

(c)

(d)

(e)

(f)

Fig. II.9. Consequences of corrosion: (a) corrosion initiation year for cast-in-place column; (b) normalized corrosion initiation year; (c) reduced rebar diameter in cast-in-place column; (d) ratio of reduced rebar diameter between ABC and cast-in-place columns; (e) initiation of strength reduction in cover concrete of cast-in-place column; (f) ratio of initiation time for strength reduction between ABC and cast-in-place columns

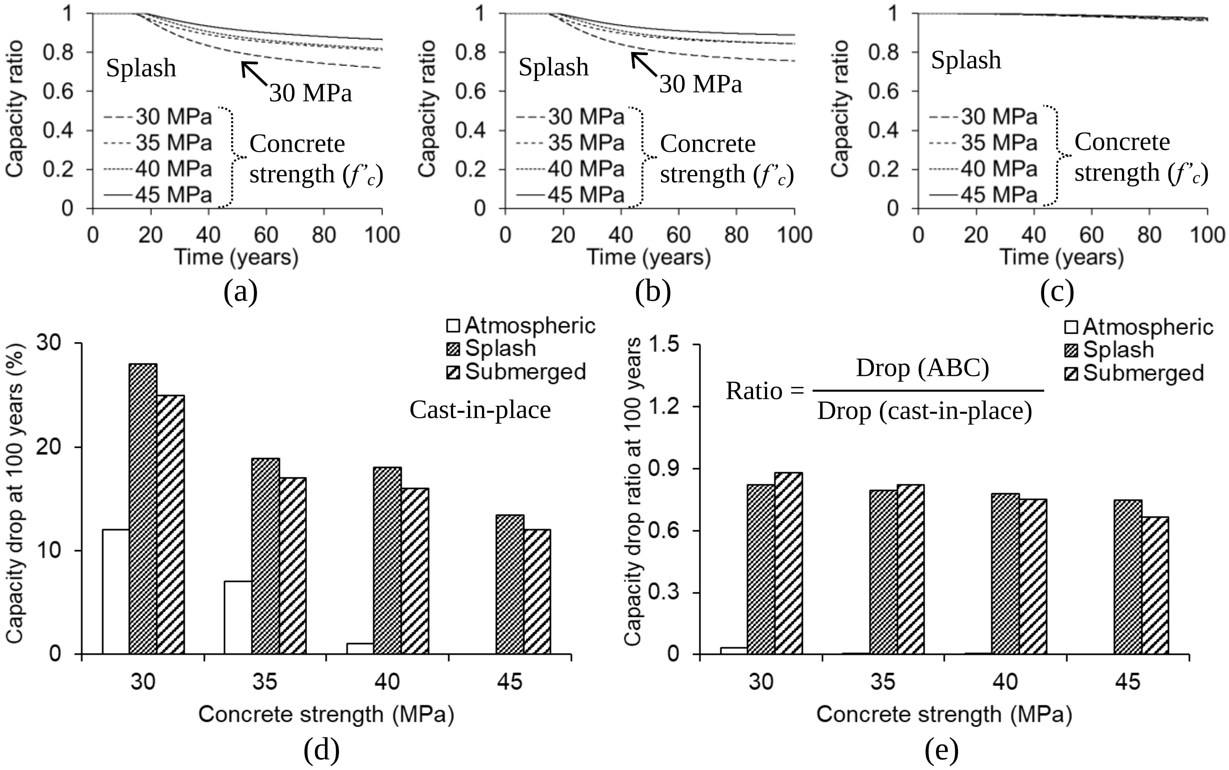

Fig. II.10. Reduction in axial capacity of column: (a) normalized capacity of cast-in-place column; (b) concrete portion of normalized capacity; (c) rebar portion of normalized capacity; (d) capacity drop of cast-in-place column at 100 years; (e) ratio of capacity drop between ABC and cast-in-place columns at 100 tears

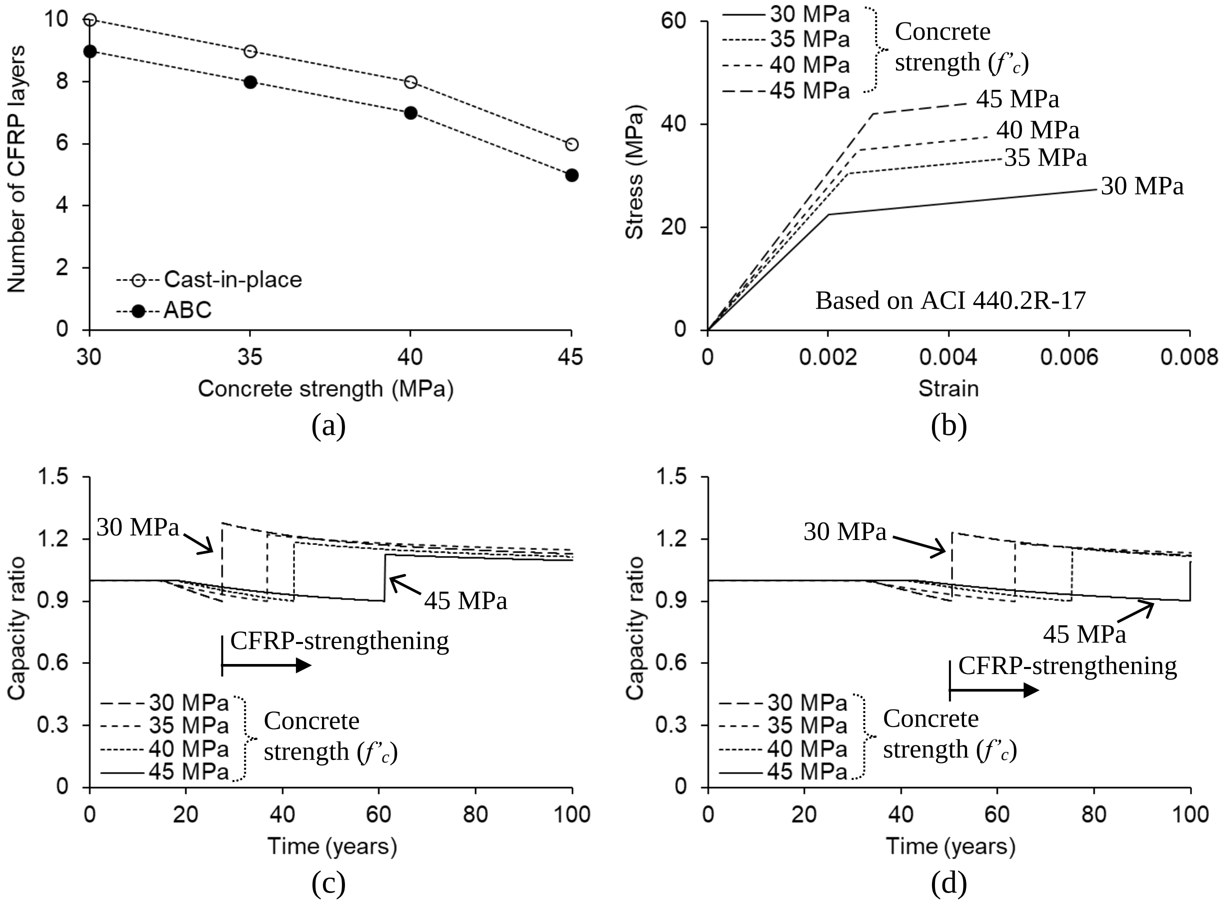

Fig. II.11. Strength recovery with CFRP-confinement: (a); CFRP layers (b) stress-strain relationship of cast-in-place concrete (f'_{cc}); (c) cast-in-place column; (d) ABC column

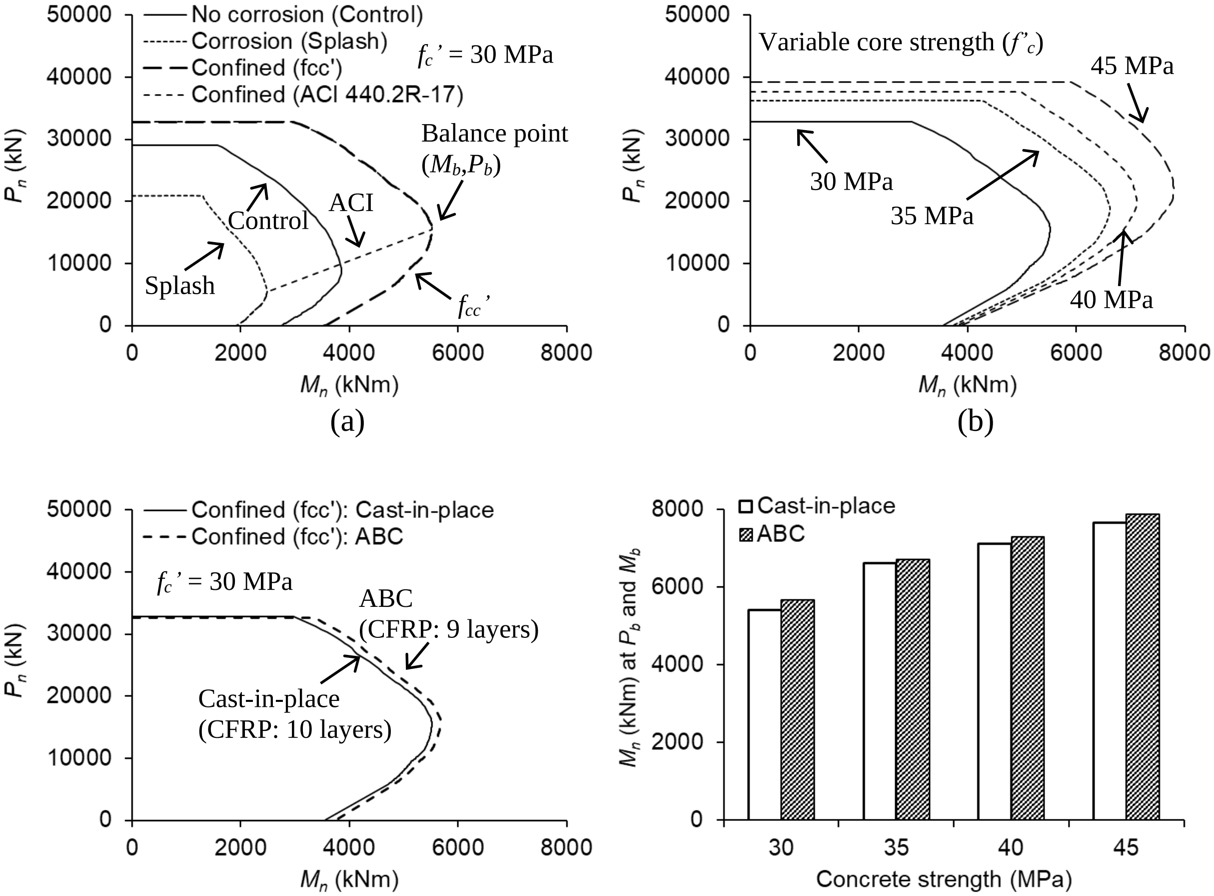

(a)

(b)

(c)

(d)

Fig. II.12. Load-moment interaction at 100 years: (a) cast-in-place column; (b) cast-in-place column confined with f'_{cc}; (c) cast-in-place vs. ABC columns; (d) comparison at balance load (P_b) and moment (M_b)

Part III: Simulated Chloride Penetration into a Solid Slab Bridge Overlayed with Ordinary Concrete and UHPC

III.1. Introduction

Corrosion poses a significant challenge for civil infrastructure, as it can degrade the structural integrity and durability of bridges over time. Additionally, bridge corrosion can incur significant costs for inspections, maintenance, repair, and potential structural rehabilitation. An annual expenditure exceeding $5 billion is allocated toward the maintenance and repair of constructed bridges (Sritharan et al. 2018). In order to mitigate corrosion, various preventive methods and maintenance strategies are implemented. One of the promising approaches for upgrading the performance of bridge structures is the use of sustainable overlays that can minimize the ingress of chlorides. Traditional overlays demand substantial thickness (Krauss et al. 2009), resulting in an increase in dead load (Wibowo and Sritharan 2018). To address such a challenge, ultra high-performance concrete (UHPC) overlays may be placed. These overlays offer reduced thickness requirements while maintaining appropriate chloride resistance. Furthermore, UHPC exhibits exceptional resistance to freeze-thaw and abrasion (Graybeal et al. 2018), making it a preferred choice for the overlays of numerous bridge structures (Bruhwiler and Denarie 2013). Consequently, comprehensive investigations are necessary to examine the effectiveness of UHPC overlays for the longevity of highway bridges.

Random walk modeling offers a valuable opportunity for the prediction of chloride diffusivity in concrete structures by simulating the movement of chloride ions within the microstructure of concrete (Wang and Kim 2023). To simulate the response of the microstructure, a user-friendly computer modelling tool like the Virtual Cement and Concrete Testing Laboratory (VCCTL) may be utilized (Bullard 2014). Unlike traditional laboratory tests that rely on physical equipment and samples, the VCCTL program enables efficient and cost-effective outcomes when studying various microstructural aspects. Additionally, agent-based modelling (Wilensky 1999) can be employed to simulate problems concerning the diffusion of chlorides through overlayed bridges in conjunction with the findings from the VCCTL method.

This study aims to assess the efficacy of ordinary concrete and UHPC overlays as a repair technique for a solid slab bridge in a corrosive environment. To achieve this, computational models are proposed to represent the microstructure of the concrete mixtures and simulate the random process of chloride migration in the overlays.

III.2. Research Significance

The significance of this study stems from the pervasive issue of chloride-related problems in highway bridges. It is imperative to address these challenges with effective methods, especially for bridge decks and superstructures. The study examines the durability of a solid slab bridge overlayed with ordinary concrete and UHPC. The significance of the study is that the efficacy of these overlay materials is elucidated from micro- to macro-level standpoints.

III.3. Benchmark Bridge

This section provides information on the design of a benchmark solid slab bridge and damage scenarios.

III.3.1. Design

In compliance with the American Association of State Highway and Transportation Officials (AASHTO) Load and Resistance Factor Design (LRFD) Bridge Design Specifications (BDS)

(AASHTO 2020), a benchmark bridge was designed with the following:

- Concrete mix design: The concrete used for the slab bridge had a water-to-binder ratio of w/b = 0.5 and a specified compressive strength of f'_c = 45 MPa (Lantsoght et al. 2013). The details of the mix design are shown in Table 1 (Tayeh et al. 2012).
- Bridge type: The benchmark bridge is a three-span solid slab bridge with a length of 32.1 m, as depicted in Fig. 1(a).
- Slab thickness and reinforcement: The slab had a thickness of 457 mm and was reinforced with No. 8 bars (diameter = 25.4 mm) placed at spacings of 150 mm. The reinforcement was designed to resist both positive and negative bending moments.
- Overlay: To protect the slab, an overlay was cast. Two types of overlay materials were used: ordinary concrete and UHPC (Table III.1). As illustrated in Fig. III.1(a), both overlays had a nominal thickness of 38 mm (Haber et al. 2018).

III.3.2. Overlay Repair

It was hypothesized that the initial overlay was damaged after 10 years of service (Fig. III.1(b)). This study considered two categories for repair. The first category (Category A) involved a scenario that replaced the damaged overlay using ordinary concrete and UHPC (Fig. III.1(c)). In the second category (Category B), the damaged overlay and the upper part of the slab were repaired at variable depths of ordinary concrete and UHPC: the repair depths included 38 mm, 51 mm, and 64 mm, as illustrated in Figs. III.1(d) and (e).

III.4. Simulation

In this section, equation-based and agent-based modeling methodologies are integrated to simulate the ramifications of bridge deterioration caused by overlay damage and reinforcement corrosion. Random walk theory is adopted to determine chloride diffusion coefficients in ordinary concrete and UHPC components.

III.4.1. Flexural Capacity Reduction

Chloride diffusion coefficient—To determine chloride diffusion coefficients using random walk, the following steps were applied:

1. The geometric and other properties of ordinary concrete and UHPC pastes were defined in the VCCTL program. The dimensions of simulated three-dimensional (3D) paste mixtures were 100×100×100 μm^3, and two-dimensional (2D) images of 100×100 μm^2 were collected from the 3D image (Fig. III.2): each of the 1×1 μm^2 cells was assigned to be one color, representing one specific constituent in the paste. For instance, paste pores were represented by black cells (Fig. III.2(c)).
2. A random walk model was developed, as shown in Fig. III.3
    2.1. A virtual environment was created, where chloride ions move randomly by extracting the paste pores from the above-discussed 2D images, and the images were imported to an agent-based model, called NetLogo (Wilensky 1999), to establish a grid pore structure within which chloride ions migrated.
    2.2. A total of 1,000 chloride ions were placed in the created virtual environment and another 1,000 chloride ions were added to a virtual environment representing water (Wang and Kim 2023).

2.3. Each chloride ion underwent 300,000 random movements (Wang and Kim 2023). The ions placed in the water freely moved; however, those located in the paste moved one step at a time, or 1 μm, when the cell in front of it was a pore.

2.4. The positions of the chloride ions were monitored and recorded at every step.

2.5. Mean square displacements were calculated to estimate chloride diffusion coefficients for the paste of the concrete (Wang and Kim 2023).

To compute the chloride diffusion coefficients for ordinary concrete and UHPC, the equations enumerated in Table III.2 were employed. Specifically, Eq. III.I (Care 2002; Li et al. 2012) and Eq. III.II (Bamforth et al. 1997) in Table III.2 were utilized to determine the chloride diffusion coefficients of the concrete mixtures at 1 and *t* years, respectively.

Chloride-induced corrosion model—Fick's second law (Eq. III.III in Table III.3) is a valuable approach to predict the penetration of chloride ions in concrete (Crank 1975). Table III.3 demonstrates equations to predict the flexural capacity of the overlayed slabs. According to the Crank-Nicholson method (Ugural and Fenster 1995), the differential equation format of Eq. III.III was converted to a discrete form in Eq. III.IV. Equation III.V in Table III.3 determines the year of corrosion initiation (Thoft-Christensen et al. 1996). Additionally, in accordance with the study conducted by Liu and Weyers (1998), chloride contents were converted to corrosion current density (i_{corr} in μA/cm^2) using Eq. III.VI in Table III.3. To replicate corrosion in a natural environment, a pitting pattern was adopted (Cao and Cheung 2014). The estimated pitting depth at a given time *t* ($P(t)$ in mm) was obtained using Eq. III.VII in Table III.3 (Val and Melchers 1997). The cross-sectional area of the rebar ($A(t)$) was then approximated using Eq. III.VIII in Table III.3.

Using the predicted reinforcement area from the above-developed models, the negative moment capacity of the solid slab was calculated by

$$M_n = A(t)\, f_y \left(d - \frac{a}{2} \right) \tag{III.1}$$

where f_y is the yield strength of the steel (f_y = 414 MPa); d is the effective depth of the solid slab (d = 393 mm); and a is the equivalent stress block factor computed by

$$a = \frac{A(t)\, f_y}{0.85 f_c^{'} b} \tag{III.2}$$

where b is the unit width of the slab (b = 300 mm).

III.5. Results

Described below are simulation results from the chloride diffusion coefficient model and the chloride-induced corrosion model. Also, the capacity loss of damaged bridge members and repaired ones are presented.

III.5.1. Chloride Diffusion Coefficients

As shown in Table III.4, the simulated chloride diffusion coefficient of UHPC (D_{ce} = 0.69 × 10^{-12} m^2/s) was significantly lower than the coefficient of ordinary concrete (D_{ce} = 6.05 × 10^{-12}). In fact, the diffusion coefficient of ordinary concrete was nine times higher than that of UHPC, primarily due to the presence of large micropores (Wang and Kim 2020).

III.5.2. Influence of Repair Material in Category A

Figures III.4(a), (b), and (c) depict chloride distributions across the concrete slab of the damaged bridge after 50 years of service, the bridge repaired with ordinary concrete, and the bridge repaired with UHPC, respectively. When the overlay repair was performed using ordinary concrete, a decrease in the chloride content was observed along the slab depth. When UHPC was utilized, the reduced chloride content was even more pronounced. Specifically, the chloride content at the surface of the rebar decreased by up to 40% and 68% when ordinary concrete and UHPC were used for the repair, respectively. Figures III.5(a), (b), and (c) illustrate chloride concentrations at the rebar surface for the damaged bridge, the bridge repaired with ordinary concrete, and the bridge repaired with UHPC, respectively. Prior to damage, the development of chloride contents over a period of 10 years was consistent across all scenarios. However, after 10 years, the damaged bridge exhibited significantly higher chloride contents relative to the bridge repaired with ordinary concrete. The use of UHPC for the bridge repair caused a slight reduction in the chloride content immediately after 10 years, owing to chloride redistributions (Song et al. 2009). Similarly, the corrosion current density depicted in Fig. III.6(a) was higher for the damaged case, while the repaired case using ordinary concrete (Fig. III.6(b)) showed a lower value. The lowest corrosion current density was observed in the repaired case with UHPC (Fig. III.6(c)). It is noteworthy that the UHPC-repaired case demonstrated a significant variation in the corrosion current density at the 10-year mark compared with chloride concentrations. This observation is attributed to the intricate relationship between the chloride concentrations and current density. Specifically, a slight change in chloride concentrations led to a pronounced change in the corrosion current density as per Equation III.VI in Table III.3. Corrosion initiation at 23 years resulted in a decrease in the steel area. When the service time of the bridge reached 50 years, the normalized cross-sectional area of the steel reinforcement was predicted to be 0.86 for the damaged bridge (Fig. 7(a)), 0.91 for the bridge repaired with ordinary concrete (Fig. III.7(b)), and 0.95 for the bridge repaired with UHPC (Fig. III.7(c)). Consequently, the flexural capacity of these cases was reduced by 14% (Fig. III.8(a)), 9% (Fig. III.8(b)), and 5% (Fig. III.8(c)) at 50 years for the three respective cases mentioned above.

III.5.3. Influence of Repair Depth in Category B

Figures III.9(a) and (b) illustrate chloride distributions at 50 years for different repair depths when ordinary concrete and UHPC were utilized, respectively. It is worth noting that repairing with ordinary concrete led to a significant reduction in the chloride content compared with the damaged case. Nonetheless, the increased repair depth did not remarkably alter the chloride content (Fig. III.9(a)). Conversely, when UHPC was employed, increasing the repair depth caused a reduction in the chloride content. Figures III.10(a) and (b) display the normalized flexural capacity of the slabs with ordinary concrete and UHPC, respectively. Similar to the chloride content, the increased repair depth did not influence the flexural capacity (Fig. III.10(a)). However, when UHPC was cast, the loss of the capacity was 5%, 4%, and 3% for the repair depths of 38 mm, 51 mm, and 64 mm, respectively, as shown in Fig. III.10(b).

III.6. Summary and Conclusions

This report has investigated the durability of a solid slab bridge through simulation techniques to understand the performance of ordinary concrete and UHPC overlays with varying repair depths. The

Virtual Cement and Concrete Testing Laboratory (VCCTL) program was utilized to model the three-dimensional microstructure of the concrete mixtures. Furthermore, agent-based models were employed to simulate the random walk of chloride ions within the microstructure of the overlays, and the chloride diffusion coefficients of ordinary concrete and UHPC were computed. With these coefficients, the process of chloride diffusion was modeled, enabling the evaluation of the structural behavior of the damaged and repaired slabs. The following conclusions can be drawn:

- The UHPC mixture had a significantly lower chloride diffusion coefficient compared with the ordinary concrete mixture possessing large micropores.
- Repairing with UHPC resulted in a more pronounced reduction in the chloride content compared with ordinary concrete.
- The corrosion current density of the slabs was highest in the damaged case, midway in the ordinary concrete repair case, and lowest in the UHPC repair case. The capacity reduction of the slabs was 14% for the damaged bridge, 9% for the bridge repaired with ordinary concrete, and 5% for the bridge repaired with UHPC at 50 years.
- Repairing with ordinary concrete led to significantly lower chloride contents compared with the damaged case; however, the increased repair depth had a limited impact on the chloride content.
- When UHPC was used for repair, increasing the repair depth reduced chloride contents. The flexural capacity of the slabs showed a minimal variation with increasing the repair depth for the ordinary concrete repair, while the UHPC repair exhibited a slight reduction in the flexural capacity with deeper repair depths.

REFERENCES

AASHTO. 2020. AASHTO LRFD bridge design specifications, American Association of State Highway and Transportation Officials, Washington, D.C.

Bamforth, P.B., Price, W.F., and Emerson, M. 1997. An international review of chloride ingress into structural concrete, Contractor Report 359, Thomas Telford, Edinburgh, UK.

Bullard, J.W. 2014. Virtual cement and concrete testing laboratory: version 9.5 user guide, National Institute of Standards and Technology, Gaithersburg, MD.

Cao, C. and Cheung, M.M.S. 2014. Non-uniform rust expansion for chloride-induced pitting corrosion in RC structures, Construction and Building Materials, 51, 75-81.

Care, S. 2002. Influence of aggregates on chloride diffusion coefficient into mortar, Cement and Concrete Research, 33, 1021-1028.

Crank, J. 1975. The mathematics of diffusion, Clarendon Press, Oxford, UK.

Graybeal, B. and Haber. Z. 2018. Ultra-high performance concrete for bridge deck overlays, No. FHWA-HRT-17-097, Federal Highway Administration, Washington, D.C.

Haber, Z.B., Munoz, J.F., De la Varga, I., and Graybeal, B.A. 2018. Bond characterization of UHPC overlays for concrete bridge decks: laboratory and field testing, Construction and Building Materials, 190, 1056-1068.

Hooton, R.D., Geiker, M.R., and Bentz, E.C. 2002. Effects of curing on chloride ingress and implications on service life, ACI Materials Journal, 99, 201-206.

Krauss, P.D., Lawler, J.S., and Steiner, K.A. 2009. Guidelines for selection of bridge deck overlays, sealers and treatments, NCHRP Project 20-07, Transportation Research Board, Washington, D.C.

Lantsoght, E.O.L., van der Veen, C., Walraven, J., and de Boer, A. 2013. Recommendations for the shear assessment of reinforced concrete slab bridges from experiments, Structural Engineering International, 23(4), 418-426.

Li, L., Xia, J., and Lin, S. 2012. A multi-phase model for predicting the effective diffusion coefficient of chlorides in concrete, Construction and Building Materials, 26, 295-301.

Liu, T. and Weyers, R.W. 1998. Modeling the dynamic corrosion process in chloride contaminated concrete structures, Cement and Concrete Research, 28(3), 365-379.

Park, K.J., Ardito, T.H., Ito, A.P., Park, K.J.B., de Oliveira, R.A., and Chiorato, M. 2007. Effective diffusivity determination considering shrinkage by means of explicit finite difference method, Drying Technology, 25, 1313-1319.

Song, H.W., Shim, H.B., Petcherdchoo, A., and Park, S.K. 2009. Service life prediction of repaired concrete structures under chloride environment using finite difference method, Cement and Concrete Composites, 31(2), 120-127.

Sritharan, S., Doiron, G., Bierwagen, D., Keierleber, B., and Abu-Hawash, A. 2018. First application of UHPC bridge deck overlay in North America, Transportation Research Record, 2672(26), 40-47.

Tayeh, B.A., Bakar, B.A., Johari, M.M., and Voo, Y.L. 2012. Mechanical and permeability properties of the interface between normal concrete substrate and ultra high performance fiber concrete overlay, Construction and Building Materials, 36, 538-548.

Thoft-Christensen, P., Jensen, F.M., Middleton, C.R., and Blackmore, A. 1996. Assessment of the reliability of concrete slab bridges, 7th IFIP WG 7.5 Working Conference, Boulder, CO, 1-8.

Ugural, A.C. and Fenster, S.K. 1995. Advanced strength and applied elasticity, Prentice-Hall, Upper Saddle River, NJ.

Val, D.M. and Melchers, R.E. 1997. Reliability of deteriorating RC slab bridges, Journal of Structural Engineering, 123(12), 1638-1644.

Wang, J. and Kim, Y.J., 2020. Functional characteristics of ultra-high performance concrete comprising various fibers. ACI Materials Journal, 117(5), 179-191.

Wang, J. and Kim, Y.J., 2023. Evolutionary characteristics of microstructural hydration and chloride diffusion in UHPC, Materials & Design, *225*, 11528.

Wibowo, H. and Sritharan, S. 2018. Use of ultra-high-performance concrete for bridge deck overlays, Report No. IHRB Project TR-683, Institute for Transportation, Iowa State University, Ames, IA.

Wilensky, U. 1999. NetLogo, Center for connected learning and computer-based modeling, Northwestern University, Evanston, IL.

Table III.1. Concrete mixtures

Component	Proportion by mass	
	Ordinary concrete	UHPC
Compressive strength (MPa)	45	239
Water	0.5	0.18
Cement	1	1
Silica fume	0	0.25
water-to-binder ratio (w/b)	0.5	0.144
Glass powder	0	0.25
Fine aggregate	2.18	1.05
Coarse aggregate	2.33	0

Table III.2. Equations for chloride diffusion coefficient model

Equation number	Equation formula	Meaning
III.I(a) III.I(b)	$D_{ce} = D_p V_p T$ $T = \frac{2V_p}{3 - V_p}$	D_p = chloride diffusion coefficient of the cement paste V_p = volumetric fraction of the paste from the micromechanical model (Li et al. 2012) T = tortuosity factor (Care 2002)
III.II	$D_{ce}(t) = D_{ce}(0)t^{-0.3}$	$D_{ce}(0)$ = initial chloride diffusion coefficient of the concrete (Bamforth et al. 1997)

Table III.3. Equations for flexural capacity model

Equation number	Equation formula	Meaning
III.III	$\frac{\partial C}{\partial t} = D_{ce}\left(t\right)\frac{\partial^2 C}{\partial^2 x^2}$	C = chloride concentration at time t and position x
III.IV	$C_{i,j+1} - C_{i,j} = k\left(C_{i+1,j} - C_{i-1,j} - 2C_{i,j}\right)$	$C_{i,j}$ = chloride concentration (percent weight (% wt.) of the cement) at position x and time t; $k = D_{ce}(t)\Delta t/\Delta x^2$ ($k < 0.5$ for the purpose of stability (Park et al. 2007))
III.V	$t_i = \frac{C_d^2}{4D_{ce}}\left(erf^{-1}\left(\frac{C_{cr} - C_0}{C_i - C_0}\right)\right)^{-2}$	C_d = cover depth in cm; erf = Gauss error function; C_{cr}= critical chloride contents (C_{cr} = 0.4%. wt cement (Hoonton et al. 2002); C_0 = surface chloride contents (C_0 = 4.7 kg/m^3 (0.29 lb/ft^3); C_i = initial chloride contents (C_i = 0%. wt cement)
III.VI	$i_{corr} = 0.92e^{\left(7.89+0.777\ln\left(1.69C_b\right)-3006/T-0.000166R_c+2.24t_c^{-0.215}\right)}$	C_b = chloride content at the steel surface in kg/m^3; T = temperature at the steel surface in Kelvin (T = 293.15 K (68°F)); R_c = resistance of the concrete cover (R_c = 1,500 ohms); t_c = year after the corrosion initiation [19]
III.VII	$p\left(t\right) = 0.0116\alpha\left(t - t_i\right)i_{corr}$	α = pitting factor (α = 10).
III.VIII	$A\left(t\right) = \begin{cases} \frac{\pi D_b^2}{4} & t < t_i \\ \frac{\pi\left(D_b - p\left(t\right)\right)^2}{4} & t_i < t < t_i + D_b/\left(0.0116 i_{corr}\right) \\ 0 & t_i + D_b/\left(0.0116 i_{corr}\right) < t \end{cases}$	D_b = initial diameter of the steel rebar

Table III.4. Diffusion coefficients of concrete

Mixture	Diffusion coefficient (D_{ce}, $\times 10^{-12}$ m^2/s)
Ordinary concrete	6.05
UHPC	0.69

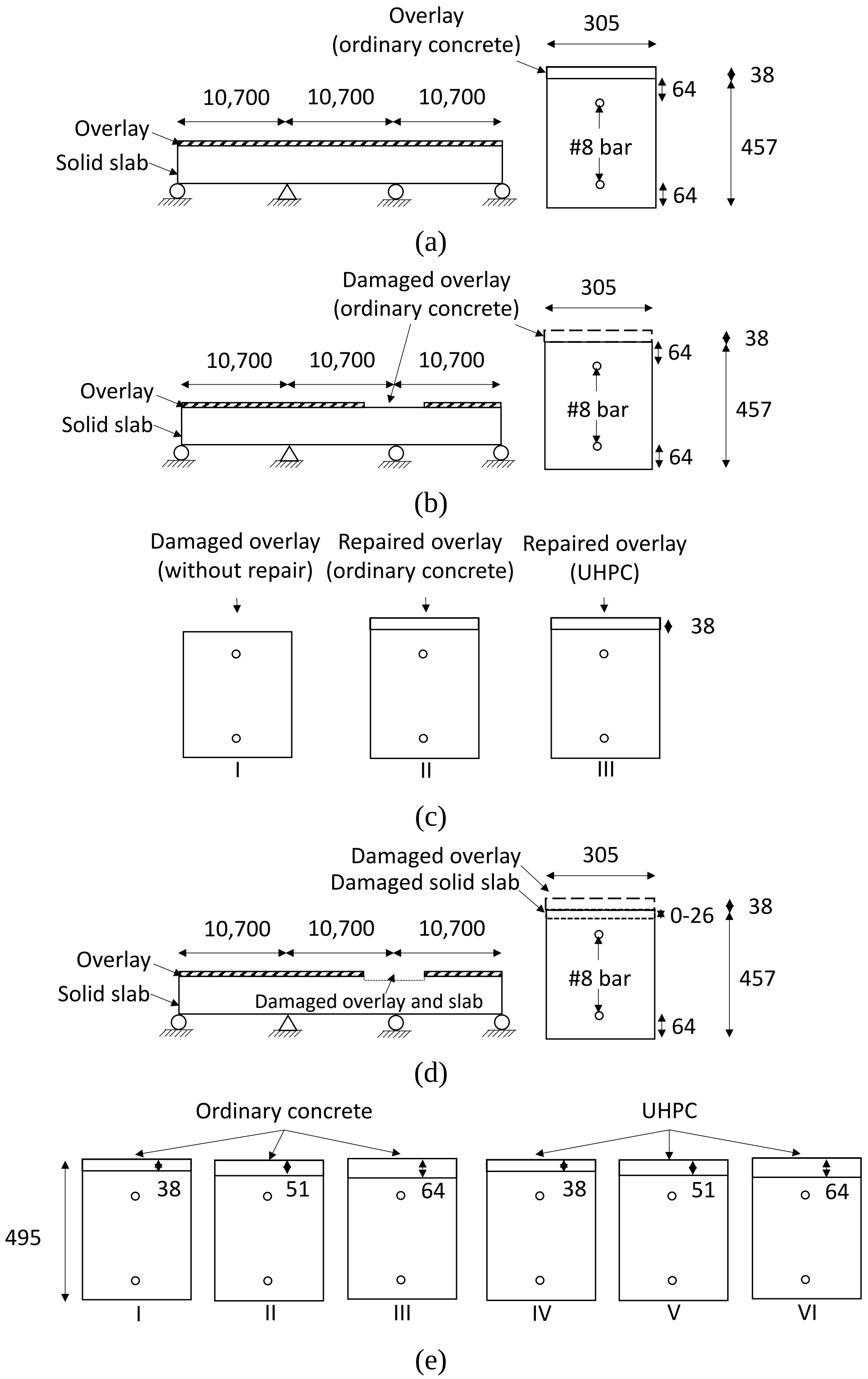

Fig. III.1. Solid slab bridge (units in mm): (a) description; (b) damaged overlay; (c) damaged and repaired overlays (Category A); (d) damaged overlay and slab; (e) damaged and repaired overlay and slabs (Category B)

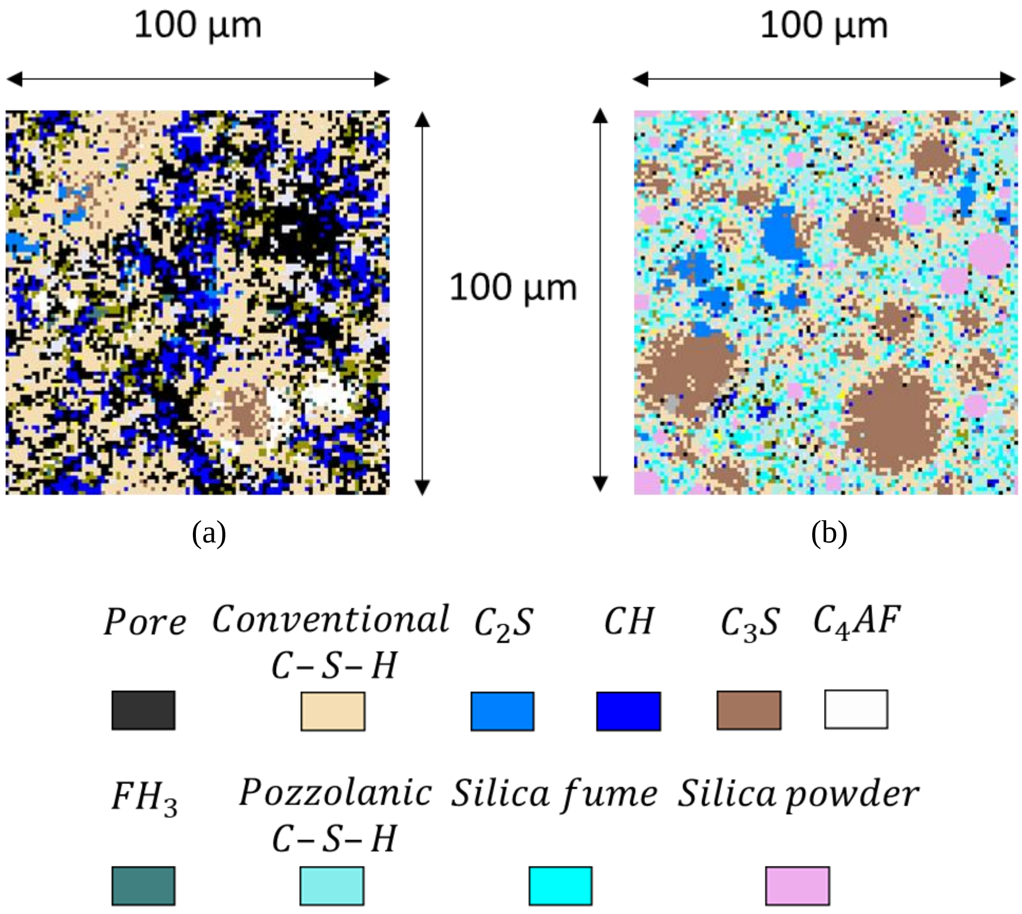

(a) (b)

(c)

Fig. III.2. Microstructure of concrete: (a) ordinary concrete; (b) UHPC; (c) color code

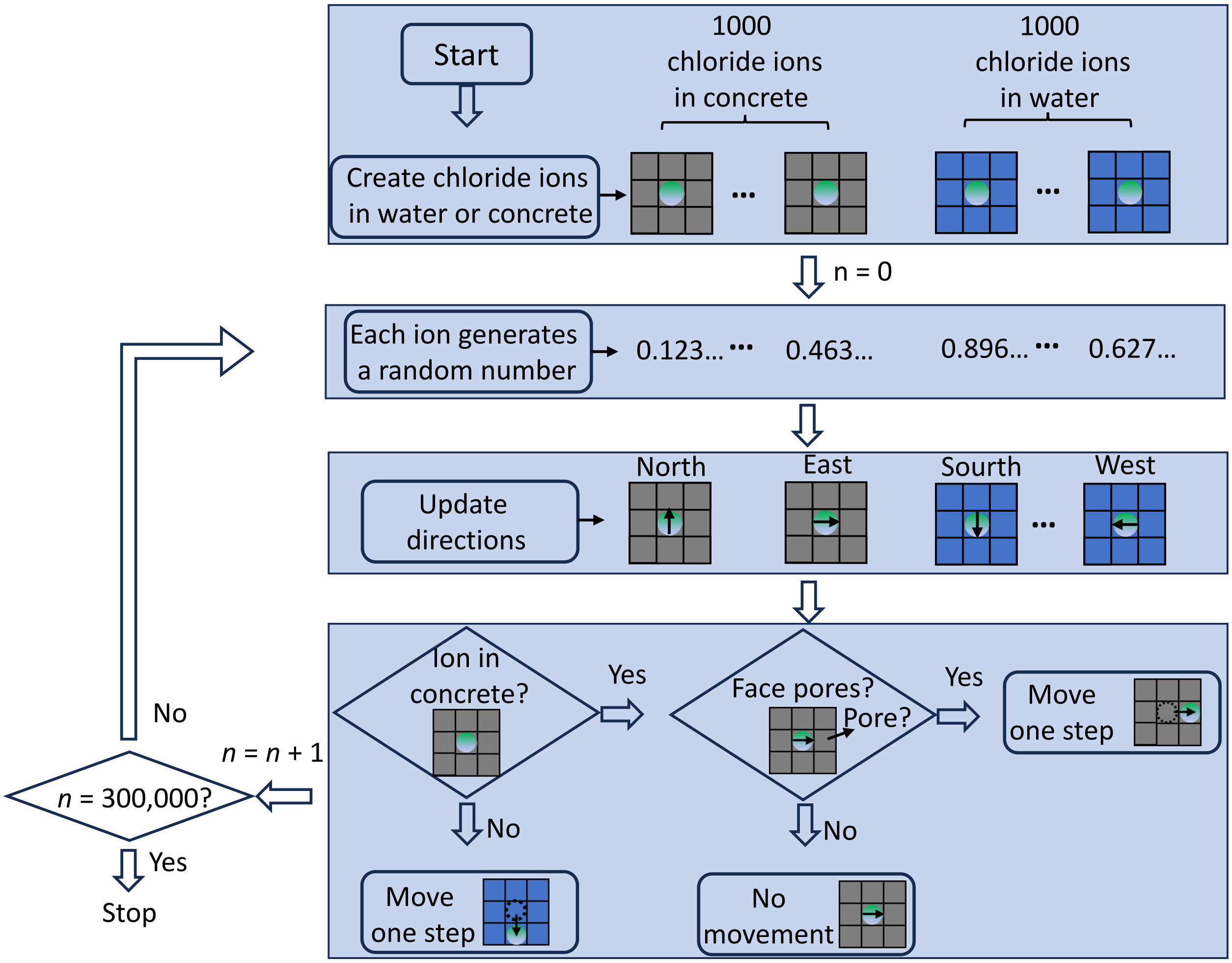

Fig. III.3. Flowchart of random walk model

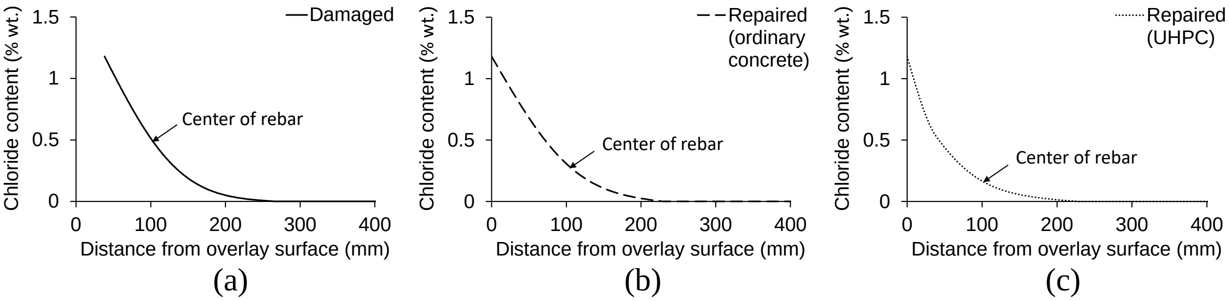

(a) (b) (c)

Fig. III.4. Chloride distribution at 50 years (Category A): (a) damaged: (b) repaired with ordinary concrete; (c) repaired with UHPC

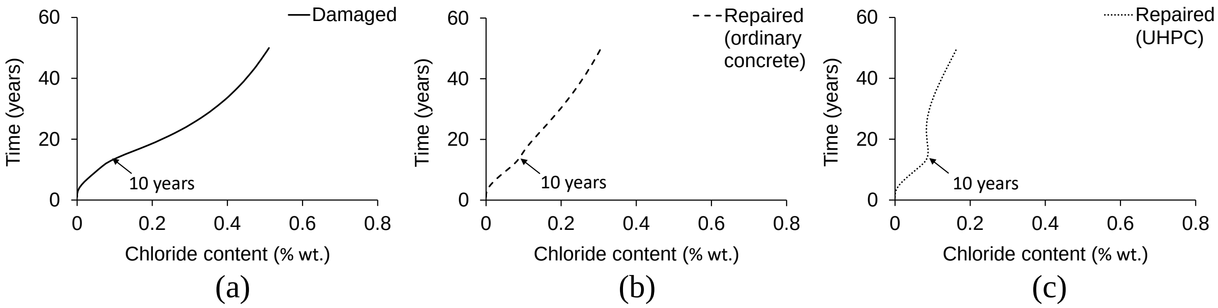

Fig. III.5. Chloride concentration at rebar surface (Category A): (a) damaged: (b) repaired with ordinary concrete; (c) repaired with UHPC

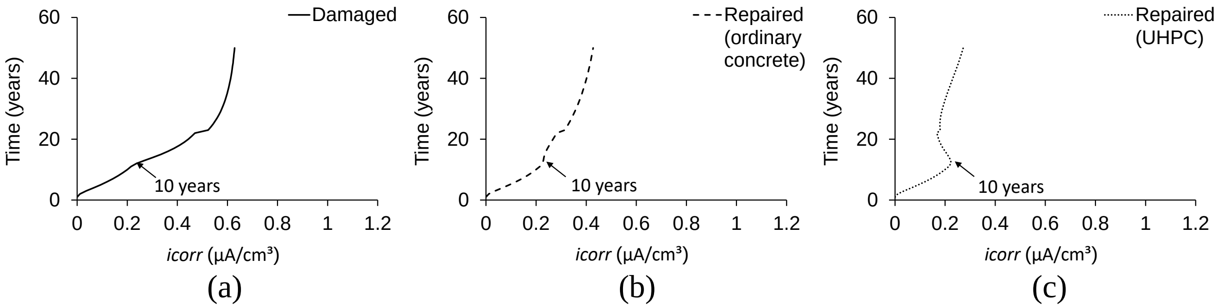

Fig. III.6. Corrosion current density at rebar surface (Category A): (a) damaged: (b) repaired with ordinary concrete; (c) repaired with UHPC

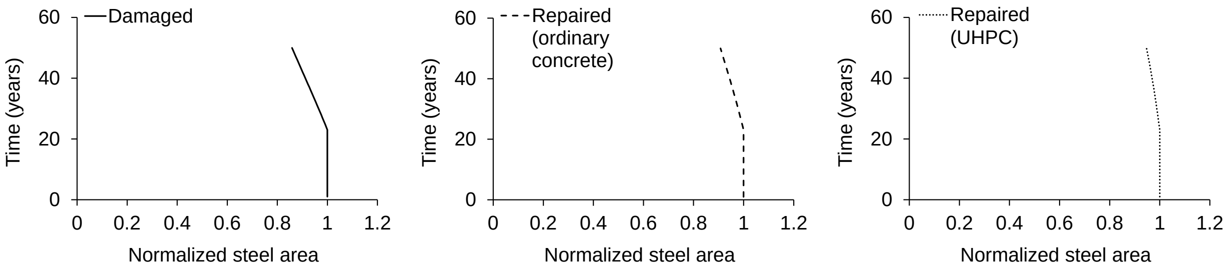

(a) (b) (c)

Fig. III.7. Normalized cross-sectional area of steel (Category A): (a) damaged: (b) repaired with ordinary concrete; (c) repaired with UHPC

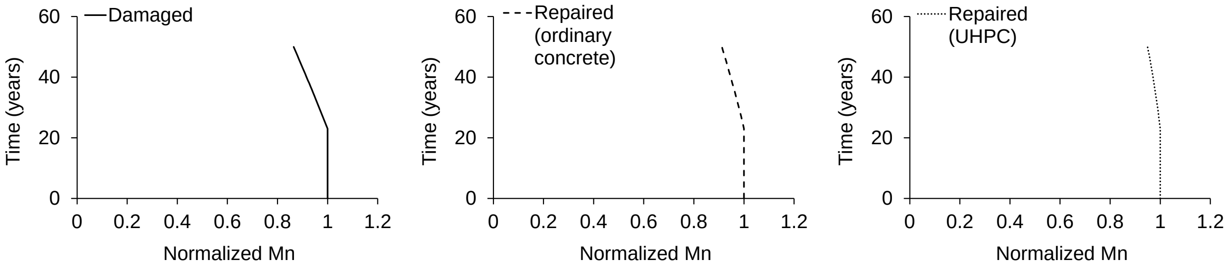

(a) (b) (c)

Fig. III.8. Normalized flexural capacity of solid slab (Category A): (a) damaged: (b) repaired with ordinary concrete; (c) repaired with UHPC

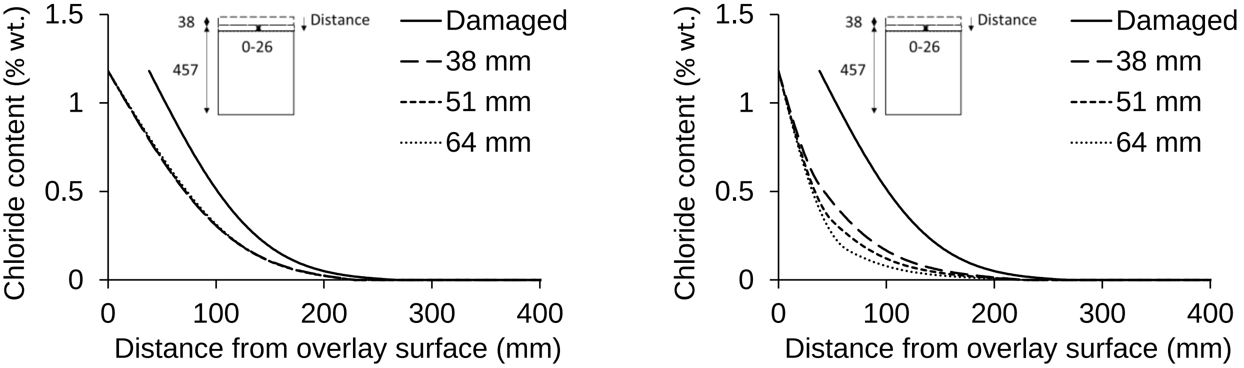

(a) (b)

Fig. III.9. Chloride distribution at 50 years (Category B): (a) repaired with ordinary concrete; (b) repaired with UHPC

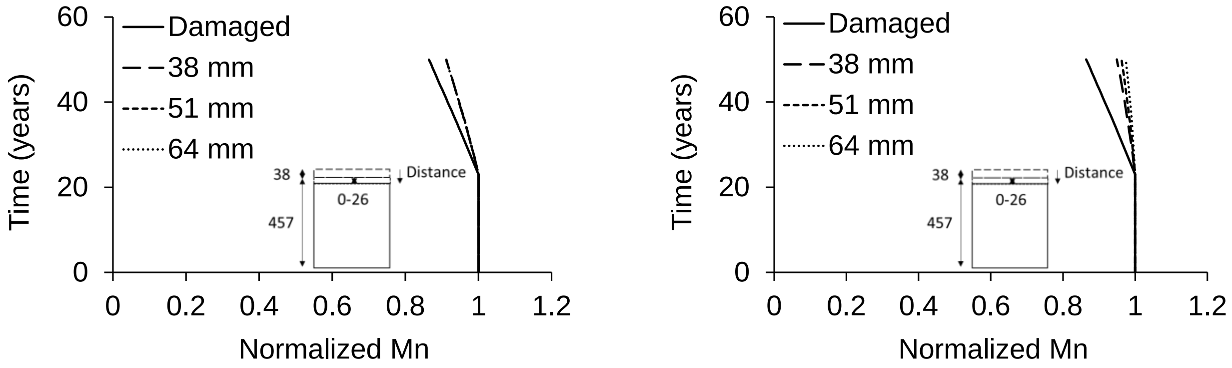

(a) (b)

Fig. III.10. Normalized flexural capacity of solid slab (Category B): (a) repaired with ordinary concrete; (b) repaired with UHPC